

The Pennsylvania State University

The J. Jeffrey and Ann Marie Fox Graduate School

**SYSTEM DESIGN OPTIMIZATION AND TECHNOECONOMIC ANALYSIS OF GREEN
HYDROGEN PRODUCTION VIA PEM ELECTROLYSIS**

A Thesis in

Chemical Engineering

by

Ernest Boakye Danquah

© 2025

Submitted in Partial Fulfillment
of the Requirements
for the Degree of

Master of Science

August 2025

The thesis of Mr. Ernest Boakye Danquah was reviewed and approved by the following:

Dr. Rui Shi
Assistant Professor of Chemical Engineering
Thesis Advisor

Dr. Phillip Savage
Walter L. Robb Family Chair, Professor of Chemical Engineering.

Dr. Andrew Zydney
Bayard D. Kunkle Chair, Professor of Chemical Engineering

Dr. Esther Gomez
Waltemeyer Mid-Career Biotechnology Professor

ABSTRACT

The global transition to a low-carbon economy hinges on making green hydrogen cost-competitive with fossil fuel-derived alternatives. Proton Exchange Membrane (PEM) electrolysis has evolved as an optimistic solution; however, its adoption is hindered by the high cost of production. While various government incentives can help bridge this gap, long-term viability requires fundamental cost optimization in production technology. This study addresses the critical need for a systematic framework that connects advances in PEM electrolyzer design and electricity source configuration to estimate the levelized cost of hydrogen (LCOH) and net present value (NPV). The electrochemical module determines the Specific Energy Consumption from the activation, ohmic, and concentration overpotentials based on the PEM design. The Techno-Economic Analysis (TEA) model applies capital-cost scaling with a 20-year discounted cash flow. An hourly resolved energy sub-model simulates photovoltaic, wind, hybrid, and grid-interactive configurations at representative inland locations in the U.S. Great Plains. The electrochemical model achieved an RMSE of 32 mV for an LCOH of \$7.05/kg, a 32 % IRR and an \$77 M NPV at the baseline plant capacity of 10,000 kg H₂/day at 333 K and 30 bar. Sensitivity analyses revealed that the electricity feedstock cost and equipment cost are the dominant cost drivers. Economies of scale show diminishing returns beyond the baseline capacity, as electricity costs start to dominate other cost factors. A capacity factor of 40-50% is found to be optimal for PEM-Renewable Energy (RE) integration. Variability in local RE potential can change the LCOH by 20–30%. This framework recommends that achieving sub-\$5/kg of H₂ requires specific energy consumption of ≤ 45 kWh/kg, an installed cost of \leq \$500/kW, and electricity tariffs of \leq \$0.05/kWh, thus guiding R&D and investment toward DOE's \$1–2/kg goals. Its modular design allows future expansion, such as material substitution sensitivity, surrogate-accelerated optimization, and geospatial LCOH mapping to support policy and commercial deployment strategies.

TABLE OF CONTENTS

ABSTRACT.....	iii
TABLE OF CONTENTS.....	iv
LIST OF FIGURES	vi
LIST OF TABLES	viii
NOMENCLATURE.....	ix
ACKNOWLEDGEMENT	xiii
Chapter 1 . Introduction	1
1.1 Problem Statement.....	1
1.2 Goals and Objectives.....	3
1.2.1 Research Questions	3
1.2.2 Aims and Objectives.....	3
Chapter 2: Literature Review.....	5
2.1 Hydrogen Economy and Global Policies.....	5
2.1.1 Sources of Hydrogen	6
2.2 PEM Electrolyzer Design Background.....	8
2.2.1 Membrane Electrode Assembly and PEM Cell Structure	9
2.2.2 Proton Exchange Membrane	11
2.2.3 Electrocatalysts Design	12
2.2.4 Bipolar Plates and Flow Field Design.....	13
2.3 Techno-economic and Renewable Energy Background	15
2.3.1 Frameworks for Technoeconomic Analysis	15
2.3.2 Cost Drivers for PEM hydrogen production.	17
2.3.3 Renewable Energy configuration	19
Chapter 3: Materials and Methods.....	21
3.0 Description of Framework.....	21
3.1 Mathematical Modelling	23
3.1.1 Electrolyzer Model Design.....	23
3.1.2 Energy System Design	32
3.2 Technoeconomic Analysis and Framework	37
3.2.1 Design Basis.....	37
3.2.2 Process Description	41
3.3 Scope and Indicators.....	42
3.3.1 System Boundary	42
3.3.2 Metrics.....	44
3.3.2.2 System-level Economic Metrics.....	45
3.4 Cost Modeling	47
3.4.1 PEM Capital Cost Sub-model	47

3.4.2 Operational Expenditure.....	49
3.5 Parametric Sensitivity and Uncertainty Analysis	50
3.5.1 Univariate Sensitivity on key Input Parameters	50
3.5.2 Multivariate and Montecarlo Simulations.....	51
Chapter 4: Results and Discussion.....	52
4.1 PEM Design Validation and Parameter Sensitivity	52
4.2. Univariate Sensitivity and Scenario analysis.....	56
4.2.1 Centralized , Baseline, and Distributed Scenario Analysis	56
4.2.2 Multi-Scenario Analysis and Sensitivity to LCOH	58
4.3 Multivariate sensitivity analysis	63
4.4 Impact of Renewable Energy configuration on LCOH	66
Chapter 5: Conclusion.....	69
5.1 Summary of Key Findings.....	69
5.2 Intellectual Merit	70
5.3 Broader Impact	70
5.4 Limitations of the Study	71
5.5 Future Research Directions	72
5.5.1 Multi-Objective Optimization of PEM Electrolyzer Design.....	72
5.5.2 Evaluation of Cost-Reduction Levers	74
5.5.3 Dynamic Optimization of Renewable-Electrolyzer Configurations	74
5.5.4 Geospatial, Hourly-Resolved LCOH Mapping with Policy and Emissions Layers.....	75
Appendix A. PEM Electrolyzer and Energy Design Parameters	77
A.1 PEM Electrolyzer Cell Design Parameters and Assumptions	77
A.2 Renewable Energy Design Parameters.....	82
Appendix B: Economic and System Parameters.....	86
Appendix C: Sensitivity Analysis Parameters	89
References.....	90

LIST OF FIGURES

Figure 1. Colors of Hydrogen: Classification of Hydrogen Production Pathways	6
Figure 2: Schematic of a Proton Exchange Membrane (PEM) water electrolyzer cell and its core components[27]	8
Figure 3: Comparison of different Membrane Electrode Assembly (MEA) fabrication method; CCM (Catalyst Coated Membrane), PTE (Porous Transport Electrode), and the DMD (Direct Membrane Deposition)	10
Figure 4: A diagram showing the primary components and candidate materials for the anode, cathode, and polymer electrolyte membrane of a PEM water electrolyzer[33].....	11
Figure 5: Illustration of common flow field plate designs used in electrolyzers: a parallel flow field (a, d), a single-serpentine flow field (b, e), and a triple-serpentine flow field (c, f)[50].	14
Figure 6: Cost drivers in hydrogen production: Relationship of electrolyzer materials, performance, and economic parameters.....	17
Figure 7: Description of LCOH framework for hourly assessment of green hydrogen production	21
Figure 8: Cross-sectional diagram of a Proton Exchange Membrane (PEM) electrolyzer for internal resistance analysis[92]	27
Figure 9: A diagram illustrating the primary water transport mechanisms across the membrane in a PEM water electrolyzer.....	29
Figure 10: Block flow diagram for PEM electrolysis hydrogen production.....	41
Figure 11: Scope and boundary for TEA of PEM hydrogen production.....	43
Figure 12: Uninstalled capital cost curve for PEM electrolyzer[66].	48

Figure 13: Model validation and voltage loss analysis for a PEM electrolyzer. (a) The polarization curve generated by an electrochemical model (solid line) is compared with experimental data points. (b) A breakdown of the total cell voltage predicted by the model.....	52
Figure 14: Parametric study of a PEM electrolyzer on cell performance. (a) Temperature Sensitivity, (b) Membrane Thickness Sensitivity, (c) Anode Exchange current density Sensitivity, (d) Cathode Exchange current density Sensitivity	53
Figure 15:a) Contour of LCOH to Temperature and current density, b) Contour of LCOH to Membrane thickness and current density.	55
Figure 16: a) LCOH at different plant capacities of 1500kg/day(distributed), 10,000kg/day and 50,000kg/day(centralized). B) The IRR and NPV for distributed and centralized systems	56
Figure 17: Tornado chart showing a univariate sensitivity of LCOH to key parameters.....	58
Figure 18: Tornado chart showing a univariate sensitivity of NPV to key parameters.....	61
Figure 19: A contour of the LCOH of hydrogen at different operating power and cost of electricity	66
Figure 20: LCOE and the corresponding LCOH impact for hydrogen production for different energy configurations.....	67
Figure 21: Contour of LCOH (\$/kg H ₂) versus design capacity (kg H ₂ /day) and electricity cost (\$/kWh). The white marker denotes the 10,000 kg/day baseline case at \$0.07 kWh	64
Figure 22: Contour of LCOH (\$/kg H ₂) versus specific energy consumption (kWh/kg H ₂) and electricity cost (\$/kWh).....	65
Figure 23 Schematic of the multi-objective optimization workflow, highlighting decision variables, constraints	73

LIST OF TABLES

Table 1: Parameters for distributed, baseline and centralized hydrogen production systems	37
Table 2: Process design basis	38
Table 3: Economic parameters and basis for discounted-cash-flow analysis	39
Appendix A. 1 PEM Electrolyzer Cell Design Parameters and Assumptions	77
Appendix A. 2: Reference exchange currents and activation energies for OER and HER [86]	79
Appendix A. 3: Polarization Curve Validation data from Debe et al. 2012[106]	79
Appendix A. 4: System Energy Balance Parameters based on H2A Case study	80
Appendix A. 5: Photovoltaic (PV) System Model Parameters	82
Appendix A. 6: Wind Turbine Parameters	83
Appendix A. 7: Polynomial Power coefficient (cp) curves in wind turbines [117]	84
Appendix A. 8: Overall Plant Operating and Design Assumptions	84
Appendix B. 1: Baseline Design Parameters: Technical Operating Parameters and Specifications, and Financial Input Values.....	86
Appendix B. 2: Capital Costs and Assumptions	87
Appendix B. 3: Operating Costs and Assumptions.....	88
Appendix C. 1: Uncertainty and Sensitivity Parameters.....	89

NOMENCLATURE

- **AC:** Alternating Current
- **AEM:** Anion-Exchange Membrane
- **BDD:** Boron-doped diamond
- **BOP / BoP:** Balance of Plant
- **BPP:** Bipolar Plate
- **CAPEX / CapEx:** Capital Expenditure
- **CCM:** Catalyst-Coated Membrane
- **CCS:** Carbon Capture and Storage or Catalyst-Coated Substrate
- **COE:** Cost of Energy
- **CRF:** Capital Recovery Factor
- **DC:** Direct Current
- **DCFROR:** Discount-Cash-Flow Rate of Return
- **DFMA:** Design for Manufacturing and Assembly
- **DI:** Deionized
- **DMD:** Direct Membrane Deposition
- **DOE:** US Department of Energy
- **EACs:** Energy Attribute Certificates
- **ECSA:** Electrochemically Active Surface Area
- **ERCOT:** Electric Reliability Council of Texas
- **EU:** European Union
- **EW:** Equivalent Weight
- **FCI:** Fixed-Capital Investment
- **GDL:** Gas Diffusion Layer

- **GHI:** Global Horizontal Irradiance
- **GPP:** Grid Power Purchase
- **GTI:** Global Tilted Irradiance
- **H₂:** Hydrogen
- **H2A:** Hydrogen Analysis Production Model
- **HER:** Hydrogen Evolution Reaction
- **HHV:** Higher Heating Value
- **HT:** High Temperature
- **i:** current density
- **IEC:** International Electrotechnical Commission
- **IRA:** Inflation Reduction Act
- **IRR:** Internal Rate of Return
- **IRS:** Internal Revenue Service
- **ISO:** International Organization for Standardization
- **kWh:** Kilowatt Hours
- **LCA:** Life Cycle Assessment
- **LCOE:** Levelized Cost of Electricity
- **LCOH:** Levelized Cost of Hydrogen
- **LFL:** Lower Flammability Limit
- **LGDL:** Liquid-Gas Diffusion Layer
- **LHV:** Lower Heating Value
- **LT:** Low Temperature
- **MACRS:** Modified Accelerated Cost Recovery System
- **MAE:** Mean Absolute Error
- **MEA:** Membrane Electrode Assembly / Assemblies

- **MMO:** Mixed Metal Oxide
- **n_d :** Drag coefficient
- **NOCT:** Nominal Operating Cell Temperature
- **NPC:** Net Present Cost
- **NPV:** Net Present Value
- **NREL:** National Renewable Energy Laboratory
- **O&M:** Operations and Maintenance
- **OER:** Oxygen Evolution Reaction
- **OPEX:** Operating Expenditure
- **PEM:** Proton Exchange Membrane / Polymer Electrolyte Membrane
- **PEMWE:** Proton Exchange Membrane Water Electrolyser
- **PFSA:** Perfluorosulfonic Acid
- **PMS:** Power Management System
- **PPA:** Purchase Power Agreements
- **sPPS:** sulfonated poly(phenylene sulfone)
- **PSO:** Particle Swarm Optimization
- **PTC:** Production Tax Credit
- **PTE:** Porous Transport Electrode
- **PTL:** Porous Transport Layer
- **PV:** Photovoltaic
- **RE:** Renewable Energy
- **RES:** Renewable Energy Sources
- **RF:** Renewable Fraction
- **RHE:** Reversible Hydrogen Electrode
- **RMSE:** Root Mean Square Error

- **RO:** Reverse Osmosis
- **SA:** Sensitivity analysis
- **SEC:** Specific Energy Consumption
- **SF:** Safety Factors
- **SMR:** Steam Methane Reformer / Reforming
- **SOE:** Solid Oxide Electrolysis
- **SOEC:** Solid Oxide Electrolysis Cell
- **SOFC:** Solid Oxide Fuel Cell
- **SPT:** Sintered Porous Titanium
- **STC:** Standard Test Conditions
- **TEA:** Techno-Economic Analysis
- **t_{mem} :** Membrane thickness
- **TRL:** Technology Readiness Level
- **v_{cell} :** cell voltage
- **WACC:** Weighted Average Cost of Capital
- **ΔG :** Reaction enthalpy, Gibbs energy
- **σ_{mem} :** Membrane conductivity

ACKNOWLEDGEMENT

I would like to express my sincere gratitude to my research advisor, Dr. Shi, for his unwavering support, insightful guidance, and encouragement throughout my research. Her vast knowledge, sharp insights and feedback have been valuable in shaping the depth and course of this research. I would like to appreciate the support of other research group members, Farhad Zaker, Hafi Wadgama, Kay Glass, Elizabeth Aigaje and Sakib Nuro.

My thanks also go to the U.S. Department of Energy's H2A team for developing and maintaining the foundational techno-economic analysis model that underpins this study. Their open-access framework provided a robust starting point for my integrated modeling efforts.

I am grateful to the NSF I-Corps facilitators, Olga E. Petrova and Erienne Olesh, whose mentorship and I-Corps program helped me engage with industry experts and refine the practical relevance of my research.

Special appreciation is due to Dr. Jae Lee of the Toyota Research Institute of America for contributing insights from the hydrogen economy and cost-driver survey, which set the trajectory for my analysis.

Finally, I would like to thank Dr. Philip Savage, Dr. Andrew Zydney, and Dr. Esther Gomez for agreeing to serve on my thesis committee.

Chapter 1

Introduction

1.1 Problem Statement

The transition to a low-carbon energy economy has placed green hydrogen at the forefront of global decarbonization strategies. A hydrogen production system, when powered by renewable electricity, yields minimal lifecycle greenhouse gas emissions, unlike hydrogen produced from natural gas or coal. Yet, despite its environmental promise, green hydrogen remains significantly more expensive than fossil-derived alternatives, with levelized costs frequently exceeding \$6/kg, compared to \$1–2/kg for grey hydrogen produced from natural gas [1], [2].

Governments and industry leaders have responded with a variety of policies and incentives. The EU and its member states, through the REPowerEU plan and the Clean Industrial Deal, aim for 40 GW of electrolyser capacity by 2030. Section 45v of the Inflation Reduction Act (IRA) introduced a production tax credit (PTC) of up to \$3 per kilogram to narrow this cost gap[3], [4]. Yet in practice, these incentives alone do not guarantee long-term competitiveness. Political shifts, changes in subsidy schemes, and volatility in renewable electricity markets can render incentive-driven projects economically vulnerable. In this context, a more enduring solution lies in driving down the intrinsic production costs of proton-exchange-membrane (PEM) electrolyzers through advances in electrolyzer design, scale economies, and system-level optimization.

Current projections indicate that demand for green hydrogen in the US could rise from less than 11.16 million metric tons in 2021 to over 27 million tons by 2040 driven by heavy industries, long-haul transportation, and steel making [5]. Among the various electrolysis technologies, PEM electrolyzers stand out for their high efficiency and compact footprint. Their operational flexibility makes them particularly

well-suited to dynamic renewable power inputs. Nevertheless, the capital cost of PEM stacks, their balance-of-plant (BoP) requirements, and the high price of electricity feedstock continue to dominate the levelized cost of hydrogen (LCOH). At the same time, these cost drivers are tightly interwoven with design choices such as current density, membrane thickness, catalyst loading, and operating temperature and with the temporal variability of upstream renewable generation. As a result, optimizing PEM hydrogen production requires a comprehensive analysis that spans electrochemical physics, economics, and energy systems modeling. Although individual studies have looked at alternatives to membranes or substitutions for catalysts, very few have systematically connected changes in material properties to their economic and technical outcomes. This gap makes it harder to pinpoint which material investments actually lead to cost-effective performance improvements when scaled up to commercial module sizes.

This report addresses this challenge by presenting an integrated framework that unites three previously siloed domains. First, we develop a detailed, physics-based model of a PEM electrolyzer stack, capturing activation, ohmic and concentration overpotentials, Faradaic efficiency, and gas crossover effects. Next, we couple these cell-level performance metrics with a modular techno-economic assessment (TEA) to quantify how material choices, operating conditions, and scale-dependent capital costs drive LCOH and net present value (NPV). Finally, we embed an hourly-resolved energy-supply layer to simulate photovoltaic, wind, hybrid, and grid-interactive configurations. We examine how renewable intermittency and geographic resource variability affect production economics and carbon intensity. By merging these three components, thus, electrochemical, economic, and energy system models, into a single cohesive framework, our research uncovers interactions and trade-offs that remain opaque under conventional, one-dimensional analyses.

1.2 Goals and Objectives

The goal of this research is to develop and validate an integrated modeling framework that couples detailed, physics-based PEM electrolyzer design with system-level techno-economic analysis and dynamic renewable energy system modeling, in order to identify key cost drivers and optimize green hydrogen production. By unifying electrochemical, economic, and energy-resource perspectives, the framework will enable data-driven decision-making for next-generation PEM electrolyzers and their deployment under diverse operating conditions.

1.2.1 Research Questions

To achieve this goal, we will address the following research questions:

1. What are the principal techno-economic cost drivers in PEM electrolyzer hydrogen production, and how do these drivers vary with plant scale, material type, and operating conditions?
2. In what ways do electrolyzer design variables such as membrane thickness, catalyst layer loading, and cell operating temperature affect energy efficiency, Faradaic performance, and stack durability, and how do these trade-offs translate into changes in levelized cost of hydrogen (LCOH) and net present value (NPV)?
3. What is the impact of different renewable energy supply configurations (photovoltaic, wind, hybrid, or grid-interactive) on hydrogen production cost and capacity factor, when modeled at an hourly resolution for location-specific scenarios?

1.2.2 Aims and Objectives

To answer these questions, this study is organized around three specific aims and tasks:

Aim 1: To develop a Physics-Based Electrochemical Model and Multi-Objective Design Optimization.

The first task is to review and design a standard PEM electrolyzer model, with a lumped-parameter electrochemical model by incorporating activation, ohmic, and concentration overpotentials. The model should account for membrane hydration, Faradaic efficiency, and gas crossover effects.

Aim 2: To construct a Modular Techno-Economic Assessment (TEA) Integrating Electrolyzer Performance.

Building on the cell-level outputs from Aim 1, Aim 2 will define a comprehensive system boundary around the electrolyzer stack and balance-of-plant components. The task is to develop a modular TEA that calculates LCOH and NPV over a 20-year period by integrating a dynamic Specific Energy Requirement, Uninstall Cost, and Operating Cost factors. A parametric study will be conducted to assess the impacts of economies of scale, as well as uncertainties in uninstalled CAPEX, electricity prices, efficiency, and fixed O&M costs on hydrogen production economics.

Aim 3: Integrate Dynamic, Hourly-Resolved Renewable Energy Modeling and Location-Specific Optimization.

Aim 3 will combine the outputs from Aim 1 and Aim 2 with an energy supply layer that simulates hourly production from photovoltaic, wind, hybrid, and grid-interactive systems in a typical U.S. region. By analyzing time-series data on renewable energy capacity factors and LCOE, we will create an hourly-resolved green hydrogen production cost profile.

Together, these Aims will fulfill our objectives of identifying cost drivers, optimizing electrolyzer design parameters, and energy-system configuration for scalable, cost-effective green hydrogen production.

Chapter 2: Literature Review

2.1 Hydrogen Economy and Global Policies

Hydrogen has become a crucial energy carrier in global decarbonization efforts. Before the end of 2019, only five countries had issued national hydrogen strategies, but by 2020, nearly 20 had released plans, with at least 10 more countries working on adding about 25 GW of electrolyzer capacity for green hydrogen by 2026[6]. The International Energy Agency's Hydrogen Projects Database documented 1,219 hydrogen projects worldwide scheduled for commissioning between 2020 and 2030[5]. Initiatives such as the “fit for 55” and REPowerEU by the European Union are targeting tens of gigawatts of electrolyser production in Europe by 2030[7], [8], [9]. Meanwhile, the United States, through the Department of Energy's "Hydrogen Shot," aims to achieve “Agenda 1 1 1” meaning \$1 per kilogram of H₂ in one (1) decade (2031)[10][11]. The 2022 Inflation Reduction Act established a new Section 45V clean hydrogen production tax credit of up to \$3 per kg for hydrogen produced with a life-cycle carbon intensity below 0.45 kg CO₂e per kg H₂[5]. The act offers a 30% investment tax credit alongside the production credit for projects beginning by 2033[5]. These incentives demonstrate strong federal support in the U.S. to foster a low-cost, clean hydrogen economy.

Beyond the incentives, effective regulation is also needed. A key regulatory development for green hydrogen is establishing criteria for incrementality, deliverability, and temporal matching of renewable energy[4]. Incrementality implies the renewable source must be new or incremental, typically in operation for no more than 36 months. Temporal matching suggests hydrogen production must align with renewable generation in real-time, with hourly matching required by 2030. Geographical deliverability specifies that the renewable source must be in the same region or deliverable to the electrolyzer[12][13]. These principles ensure electrolytic hydrogen credited as "clean" is truly powered by new, clean energy sources rather than diverted existing generation[4], [14][13][12].

Over 95% of global hydrogen, roughly 70–90 million tonnes annually, is produced through steam methane reforming of natural gas or coal gasification[15][6]. This process yields inexpensive hydrogen (\$1–2/kg) but emits large amounts of CO₂, which conflicts with climate goals[6]. Fossil-based H₂ costs around \$1–3 per kg, while electrolytic hydrogen with low-carbon electricity ranges from approximately \$3.5–11 per kg, given current prices[5]. The main reason for this price gap is capital and electricity costs, which make up about 50–60% of the levelized cost of hydrogen (LCOH)[6]. The insecurity of the hydrogen economy stems from the fact that, without substantial cost reductions, clean hydrogen cannot easily compete with grey hydrogen[5]. PEM electrolyzers depend on some of the rarest minerals on earth, such as iridium as catalysts and gallium/platinum-coated components. A rapid expansion of PEM deployment could strain the supply and increase the prices of these critical materials[15]. This supply risk highlights the need for R&D to find substitutes for noble metals in electrolyzers. . Despite these challenges, projections for a green hydrogen economy remain optimistic[5].

2.1.1 Sources of Hydrogen

Hydrogen can be classified with a color taxonomy to indicate its production method and carbon footprint.

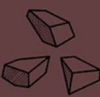





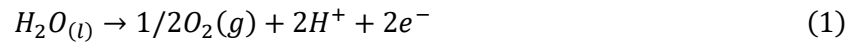
Color	Brown Hydrogen	Grey Hydrogen	Blue Hydrogen	Turquoise Hydrogen	Green Hydrogen	Pink Hydrogen
Process	Gasification	SMR*	SMR or Gasification with carbon capture	Pyrolysis	Electrolysis	Electrolysis
Source	Coal 	Natural Gas 	Natural Gas 	Natural Gas 	Renewable electricity 	Nuclear electricity 

Figure 1. Colors of Hydrogen: Classification of Hydrogen Production Pathways

The production methods and sources also inform the cost of the product. Green hydrogen is produced from water electrolysis powered by solar, wind, or hydro. It yields zero direct CO₂ emissions with a production cost that ranges from \$2.50 to \$11 per kilogram of hydrogen[6][16][17][18]. Grey hydrogen is made by reforming natural gas or gasifying coal without capturing CO₂. The typical price falls between \$1.5 and \$2.5/kg in major markets[18][19][20]. Blue hydrogen uses the same fossil feedstocks but adds carbon capture and storage. It is considered a lower-carbon interim solution as its life-cycle emissions depend on capture efficiency and methane leakage. The reported cost of blue hydrogen ranges from \$2.00 to \$7.00/kg[18]. Brown and black hydrogen describe hydrogen produced from lignite and bituminous coal, respectively, without CCS at a cost of about \$1.20 to \$2.20/kg[21]. A review of the cost of nuclear hydrogen energy-powered electrolysis) reveals a production cost between \$1.1 and \$6.76/kg as influenced by the reactor type and scale of production[22]. Other types, such as "turquoise" hydrogen, are sourced from methane pyrolysis, while "white" hydrogen describes the rare case of naturally occurring geologic hydrogen[23][24][21]. While these colorful labels help facilitate discussion, in practice, hydrogen is also evaluated based on purity and usage standards. The ISO 14687 standard specifies two grades of hydrogen fuel for PEM fuel cell road vehicles: Type I Grade D (gaseous) and Type II Grade D (liquid) hydrogen[25]. Type I Grade D gaseous hydrogen, used in compressed H₂ tanks for cars and buses, must contain at least 99.97% hydrogen (fuel index) with total non-H₂ impurities of ≤ 300 $\mu\text{mol/mol}$. This aligns with SAE J2719 and ISO requirements that limit key contaminants such as H₂O, O₂, N₂, CO, CO₂, CH₄, and sulfur compounds to parts-per-million or lower levels to prevent fuel cell poisoning[26]. Type II Grade D liquid hydrogen must meet similar purity standards for cryogenic liquid fuel systems[27]. Notably, such high purities are most easily achieved through electrolytic hydrogen, which is produced at high purity by design.

2.2 PEM Electrolyzer Design Background

Hydrogen production in a PEM electrolyzer is an electrochemical process that breaks down water with electricity. Deionized water is supplied to the anode side of the cell. The water is oxidized into oxygen gas (O_2), protons (H^+), and electrons (e^-) via an Oxygen Evolution Reaction.



The protons (H^+) produced are conducted through the solid polymer membrane to the cathode side. The membrane is designed to be selective to protons over oxygen gas. At the cathode, a platinum on carbon, Pt/C, facilitates the reduction of protons into hydrogen.



The net result across the cell is the product of hydrogen and oxygen gases

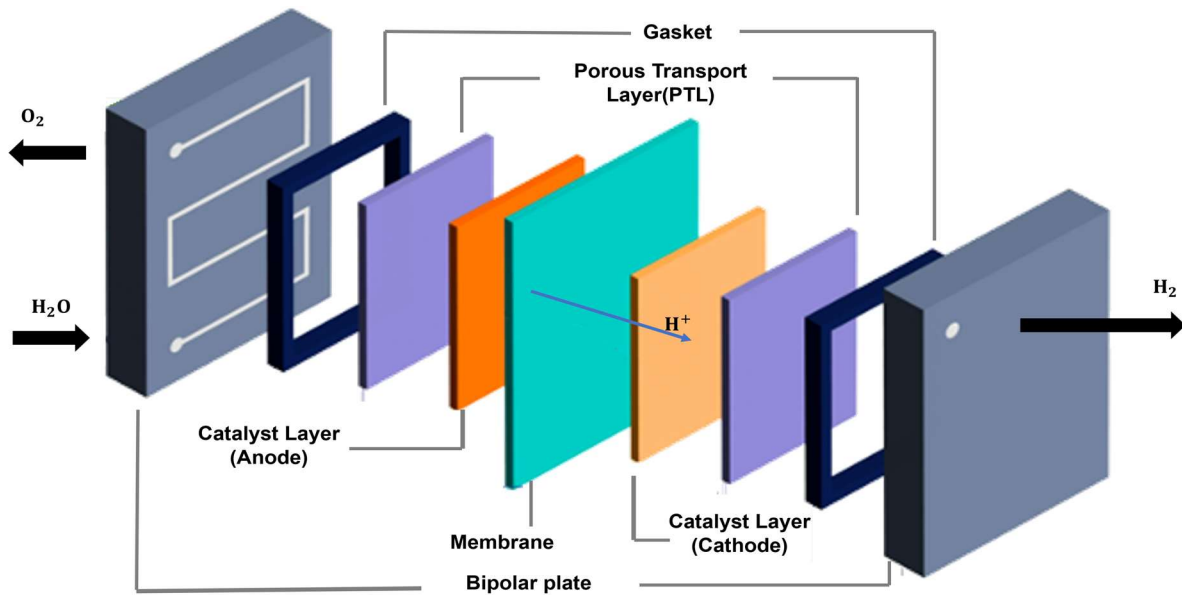


Figure 2: Schematic of a Proton Exchange Membrane (PEM) water electrolyzer cell and its core components[28]

2.2.1 Membrane Electrode Assembly and PEM Cell Structure

The fundamental unit of a PEM electrolyzer is a single electrolysis cell composed of a membrane-electrode assembly (MEA) pressed between two flow-field plates (bipolar plates). The MEA consists of a thin proton-conducting polymer membrane ($\approx 50\text{--}200\text{ }\mu\text{m}$ thick) coated on each side with porous catalyst layers (anode and cathode)[29]. In a state-of-the-art design, these catalyst layers are applied directly onto the membrane in a configuration called catalyst-coated membrane (CCM). Alternatively, the catalyst can be applied onto a porous substrate (such as the gas diffusion layer) and then assembled against the membrane; this is known as a catalyst-coated substrate (CCS), decal transfer method or PTE (Porous Transport Electrode)[30][31]. Experiments have shown that CCM-based MEAs slightly outperform those with catalysts on the substrate due to better interface conductivity and utilization of the catalyst[15]. They experience less mechanical deformation or decoupling from electrodes during hydration and dehydration cycles. CCM MEAs can be readily removed and replaced in stack maintenance[15]. A study demonstrated continuous operation over 20,000 hours with a CCM-based PEM electrolyzer cell, highlighting the robustness of the bonded interface[32][15][33]. Figure 3 compares different Membrane Electrode Assembly (MEA) fabrication methods. The configurations include CCM (Catalyst Coated Membrane), where the catalyst layers are deposited directly onto the proton exchange membrane (PEM), and PTE (Porous Transport Electrode), where the catalyst is coated onto the gas diffusion layers (Ti-GDL and C-GDL), along with the DMD (Direct Membrane Deposition) method[31].

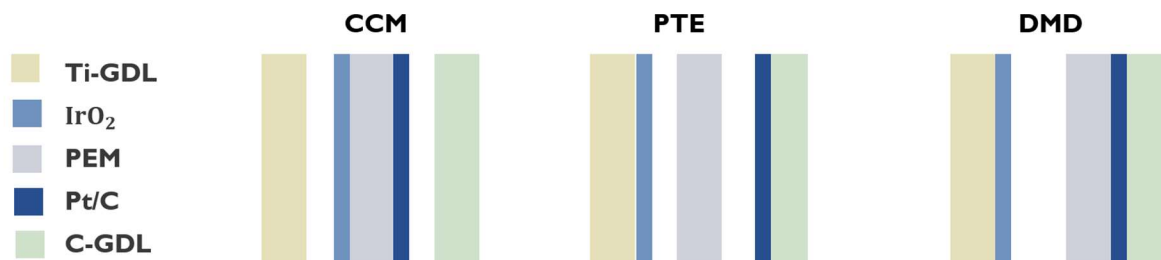


Figure 3: Comparison of different Membrane Electrode Assembly (MEA) fabrication method; CCM (Catalyst Coated Membrane), PTE (Porous Transport Electrode), and the DMD (Direct Membrane Deposition)

The catalyst-coated membrane is sandwiched between two porous transport layers (PTL) (Gas Diffusion Layer (GDL)), to facilitate reactant flow, remove products, and conduct electrons. In PEM fuel cells, the GDL typically consists of carbon fiber paper or cloth. However, in PEM electrolyzers, the highly oxidizing environment at the anode requires corrosion-resistant materials such as titanium felts or sintered porous Ti for the PTL on the oxygen side[15]. The cathode PTL may be carbon-based if maintained at low potential, but titanium is often used to enhance durability, especially since oxygen crossover can create a local fuel cell reverse potential on the carbon cathode[33]. The PTL distributes liquid water from the flow field channels to the anode catalyst and allows oxygen bubbles to escape back into the channels. At the cathode, the PTL/GDL provides pathways for hydrogen gas to exit and for any excess water to be removed. It also conducts electrons from the cathode catalyst layer to the bipolar plate. Since the anode PTL is often made of titanium to resist corrosion, its surface may develop a thin oxide layer that increases contact resistance over time. To prevent this, manufacturers often coat the Ti PTL or bipolar plate with noble metals, such as a thin layer of gold or platinum, to maintain low interfacial resistance[31]. The design of the PTL (whether felt, sintered powder, or mesh) and its thickness significantly impact performance. Thinner PTLs reduce ohmic drop and improve mass transport, but if too thin, they might have uneven contact with the catalyst layer[30].

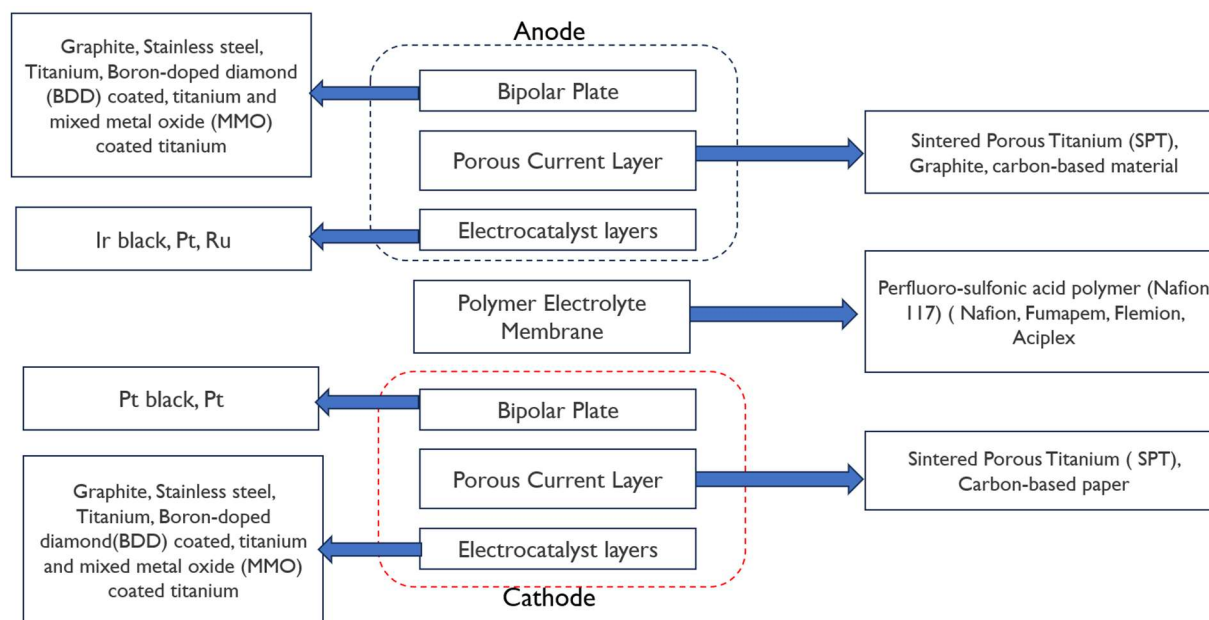


Figure 4: A diagram showing the primary components and candidate materials for the anode, cathode, and polymer electrolyte membrane of a PEM water electrolyzer[34]

2.2.2 Proton Exchange Membrane

The polymer electrolyte membrane in PEM electrolyzers not only conducts protons but also serves as the gas separator between H_2 and O_2 . Conventional PFSA membranes (NafionTM 117) remain the benchmark for proton conductivity and chemical stability, but recent hydrocarbon-based ionomers provide lower costs and higher thermal tolerance, albeit with challenges in oxidative stability and gas separation[35]. PFSA membranes have high proton conductivity (about 0.1 S/cm when fully hydrated at 80 °C) and excellent chemical stability in the harsh oxidative environment[36]. Their mechanical toughness and long history in PEM fuel cells make them a natural choice for electrolyzers as well[36]. However, PFSA membranes have notable drawbacks: cost, environmental impact, and gas permeability[36]. Nafion and similar PFSA membranes show significant hydrogen crossover, especially at higher temperatures or with thinner membrane thickness[37].

These issues have led to research into hydrocarbon-based membranes. The tighter polymer morphology of hydrocarbon proton exchange membranes (such as sulfonated polyarylene ethers, polyetherketones, or

polyphenylene sulfones) in general results in a lower gas permeability than PFSA[35]. They can also be less expensive and have a lower environmental impact. They can potentially reduce hydrogen crossover while maintaining comparable proton conductivity when fully hydrated and tolerate higher operating temperatures ($>80\text{ }^{\circ}\text{C}$) without degrading[38][36][39]. Klose et al. (2020) demonstrated a PEM electrolyzer MEA with a sulfonated poly(phenylene sulfone) (sPPS) membrane that achieved 3.5 A/cm^2 at 1.8 V . Thus, more than doubling the current density of a Nafion 115 baseline MEA ($\sim 1.5\text{ A/cm}^2$ at 1.8 V) with three times lower resistance and one-third the H_2 crossover of Nafion[36]. The challenge remains ensuring long-term chemical stability. Composite membranes combine a PFSA with a porous or inert backbone to reduce swelling and crossover. Adding inorganic fillers (like silica, zirconia, or graphene oxide) to Nafion can lower gas permeability by filling voids, though sometimes at the expense of slightly reduced conductivity[15]. Reinforced membranes (e.g., expanded PTFE-reinforced Nafion) are used in some commercial electrolyzers to boost mechanical strength, permitting thinner membranes that still resist pinholes and hydrogen leaks. The ideal membrane would be thin, highly proton-conductive, gas-impermeable, durable in hot, acidic, oxygen-rich environments, and cost-effective. Advances in hydrocarbon and composite membranes are actively advancing the field toward these goals[36].

2.2.3 Electrocatalysts Design

The state-of-the-art OER catalyst in PEM systems is iridium oxide (IrO_2) (doped with ruthenium or other elements)[34]. IrO_2 offers a balance of reasonable activity and sufficient stability. Ruthenium oxide (RuO_2) actually has higher intrinsic OER activity (lower overpotential), but pure RuO_2 anodes corrode quickly in acidic OER conditions, resulting in short lifespan[40][15]. Previous studies from 1976 established activity trends for OER and HER catalysts. Miles and Thomason found that, among single metals, the OER activity (at $80\text{ }^{\circ}\text{C}$ in acid) follows the order $\text{Ir} \approx \text{Ru} > \text{Pd} > \text{Rh} > \text{Pt} > \text{Au}$ [41]. Similarly, for the HER, the order was $\text{Pd} > \text{Pt} > \text{Rh} > \text{Ir} > \dots > \text{Ni}$ (with palladium and platinum being the best pure metals for H^+ reduction)[41]. These results explain why Pt and Ir are chosen as primary electrocatalysts. Most PEM anodes commonly

use iridium in oxide form (IrO_2 or Ir black, which forms IrO_2 in situ) with loadings around 1–2 mg_Ir/cm² and ESCA of 601 $\mu\text{C}/\text{cm}^2$ [42]. Even at these loadings, iridium's scarcity remains a significant concern due to its limited supply[15]. Research efforts to reduce Ir usage include developing high-surface-area IrO_2 nanoparticles or nano-porous iridium, which have higher mass activity[43][44][45][46]. Some alternative catalysts include crystalline mixed oxides like pyrochlores (e.g., $\text{Pb}_2\text{Ir}_2\text{O}_{7-x}$), perovskites (such as SrRuO_3), metal phosphides or nitrides. However, no fully platinum-group-metal-free catalyst has yet demonstrated both high OER activity and adequate stability in the PEM electrolyzer environment[47]. Non-noble candidates (e.g., manganese or cobalt oxides) often dissolve in acidic electrolytes under OER conditions[48].

On the HER side, there is some progress with PGM-free catalysts. Molybdenum sulfides and tungsten carbide materials have demonstrated HER activity in acid, but their stability remains an issue. Since the cathode Pt loading is already low and minimally impacts cost, the focus stays on the anode. One promising approach is to use ultra-low Ir loadings by leveraging advanced supports: Carmo et al. mention that catalyst development efforts include novel support materials that enhance Ir utilization and research into catalysts like crystalline IrRuO_x or metastable phase oxides that might provide higher activity per unit of Ir[15].

2.2.4 Bipolar Plates and Flow Field Design

The bipolar plate (BPP) in a PEM electrolyzer functions as both the anode of one cell and the cathode of the next cell in a series stack (hence "bipolar"). It offers structural support, separates gases between cells, conducts electrical current, and includes flow channels to distribute water and collect gases. Bipolar plates are usually made of titanium in PEM water electrolyzers because of titanium's corrosion resistance in acidic, oxygen-rich environments[49][50].

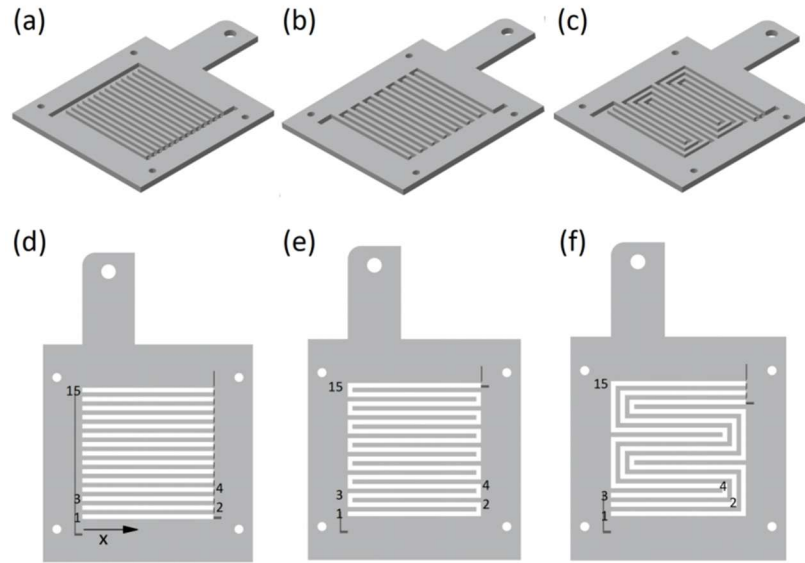


Figure 5: Illustration of common flow field plate designs used in electrolyzers: a parallel flow field (a, d), a single-serpentine flow field (b, e), and a triple-serpentine flow field (c, f)[51].

Several flow field design patterns are available: parallel channels, single-serpentine, multiple serpentine, grid/mesh patterns, and pin-hole or porous distributor plates[51]. Parallel channels offer low-pressure drop, which is advantageous for pump efficiency, but can suffer from uneven flow distribution[51]. In a single serpentine flow field, all water and gas move through one channel. This design produces significantly higher local flow velocities than a parallel flow field, which distributes flow across multiple channels. Therefore, a single-serpentine flow field has a much higher pressure drop than a parallel design[52][51][53]. Multi-serpentine designs aim to balance flow distribution and pressure. In PEM fuel cells, serpentine and interdigitated flows are common to manage liquid water removal, whereas in electrolyzers, managing oxygen gas removal from the anode is the main challenge[54].

Studies on the impact of flow field design on PEM electrolyzer performance have yielded conflicting results. Ito et al. observed better performance with a parallel flow field compared to a single-serpentine design up to 1.0 A/cm^2 , attributing this to differences in concentration overpotential, although this explanation may be less important at lower current densities[52]. Similarly, another study reported improved performance for parallel flow fields at current densities up to 3.0 A/cm^2 , while Li et al.'s research

indicated better performance for a single-serpentine configuration[55][56]. Several other designs, such as interdigitated and pin-type flow fields, are documented in the literature but are less common in practice[57][58][59]. Additive manufacturing has also been explored for complex bipolar plate geometries, including flow fields with internal cooling or innovative 3D patterns[60][61].

2.3 Techno-economic and Renewable Energy Background

While individual studies have explored PEM design options, few have systematically linked changes in material properties to techno-economic outcomes. This gap hampers efforts to determine which material investments genuinely lead to cost-effective performance improvements when scaled to commercial module sizes. Our work aims to address these gaps by incorporating a validated 0D/1D model into an LCOH optimization framework.

2.3.1 Frameworks for Technoeconomic Analysis

Several open-source frameworks have been developed for the techno-economic analysis (TEA) of hydrogen production systems, including H2A, HySupply, and the Techno-Economic Simulation Tool (TechEST)[2], [62], [63][64]. These frameworks provide valuable tools for evaluating the cost of various hydrogen pathways. However, most of these Excel-based models are fundamentally static and often lack dynamic integration between physical system modeling and process economics. They lead to oversimplified assessments that do not fully capture the temporal variability of renewable energy inputs or the operational flexibility of electrolyzer systems. Recent updates to proprietary software, such as AspenTech's V14.1, have introduced modules for detailed PEM electrolyzer design and operation, enabling more granular process simulation. Despite these advancements, affordability remains a significant barrier for users, particularly for startups and early-stage technology developers. Therefore, an open-source framework is encouraged for those who may lack the resources to invest in high-cost commercial software.

The U.S. Department of Energy's H₂A model and similar frameworks in Europe and Australia adopt a discounted cash flow approach, which defines LCOH as the ratio of the present value of all costs to the total kilograms of H₂ produced, deriving key financial metrics such as net present value (NPV) and internal rate of return (IRR) from the annualized cash flows[11], [15]. This methodology ensures that both capital and operational costs are captured in a single metric, allowing for direct comparison to market prices and policy targets.

H₂A was used in a 2014 DOE study by Colella et al. to compare PEM electrolysis at “forecourt” scale (distributed, 1,500 kg H₂/day) and “central” scale (50,000 kg/day) for current technology versus projected future improvements[65]. The study identified the high capital cost and low capacity factor of forecourt electrolysis as key cost drivers and noted that only with future cost reductions and cheaper electricity could PEM electrolysis meet the DOE target of \$2–4/kg (untaxed) hydrogen[65]. Traditional H₂A-based analyses assume a relatively steady operating profile and often base inputs on current costs or optimistic future estimates[2]. Another critique is that many TEA studies assume high capacity factors (e.g., electrolyzer running 90% of the time) to lower hydrogen costs, whereas if paired with intermittent renewables without grid backup, the capacity factor may be much lower (solar-only electrolysis might operate around 20–25% of hours)[66]. A few studies incorporate the cost of energy storage or grid connection to boost capacity factors, such as including a battery or allowing grid electricity at times to supplement renewables[67][63][68].

Another often overlooked factor is degradation and replacement. Most LCOH models typically include a stack replacement cost at a set interval(every 7 years). However, degradation is a continuous process that can also increase operating power needs over time. Few models fully incorporate performance degradation into the cost calculation[69]. It's also noted that some cost studies use historically low renewable prices and assume they can be entirely dedicated to H₂ production. While renewable Purchase Power Agreements (PPA) prices have dropped significantly (wind and solar < \$20/MWh in best cases[6], the reality of procuring large volumes of such low-cost electricity for electrolysis may involve additional grid costs or

variability. Models that assume a constant \$20/MWh power price may be oversimplified; a more realistic approach might use hourly price distributions or a mix of solar and wind profiles[70].

2.3.2 Cost Drivers for PEM hydrogen production.

Badgett et al. predict that several important factors will help to lower the cost of electrolysis-generated hydrogen. These comprise changes in the materials used and the design of the system, the scale of manufacturing activities, and the learning effect acquired from the actual implementation of more electrolysis systems[71].

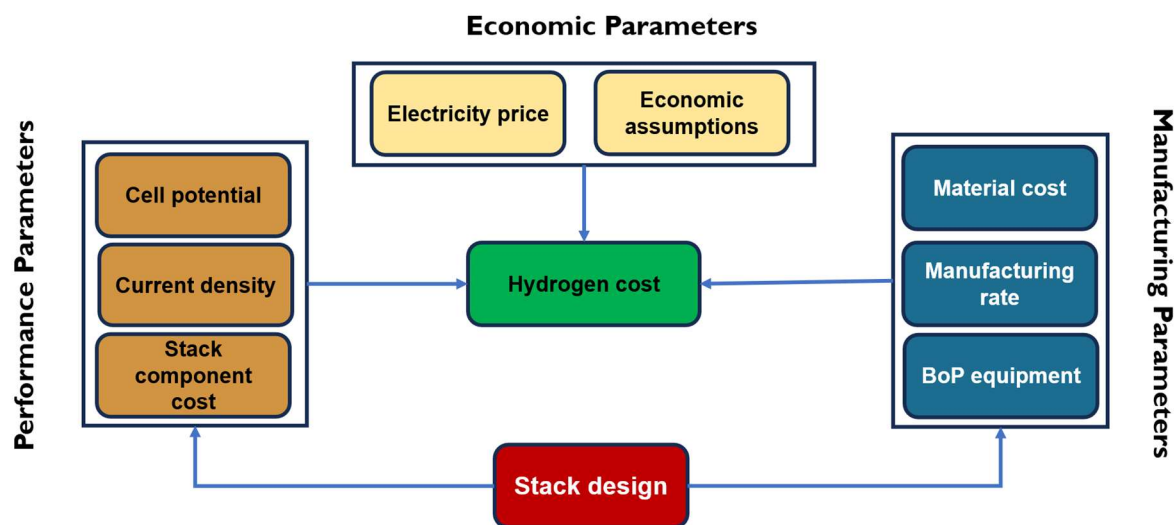


Figure 6: Cost drivers in hydrogen production: Relationship of electrolyzer materials, performance, and economic parameters

Badgett et al. predict that several important factors will help to lower the cost of electrolysis-generated hydrogen. These comprise changes in the materials used and the design of the system, the scale of manufacturing activities, and the learning effect acquired from the actual implementation of more electrolysis systems[71]. Techno-economic analyses (TEAs) as a tool, can help investigate how changing various cost factors might affect the hydrogen cost and guide research, development, and electrolysis

technology investment(Figure 6)[71]. For example, the performance, manufacture, and related costs of the electrolyzer stack directly depend on its design. These elements, therefore, affect the capital expenses of the system as well as the rate of hydrogen generation, two important determinants of the total hydrogen cost[72][73].

Contemporary studies report uninstalled stack CAPEX ranging from \$800 to \$1,500 per kilowatt (kW) of electrolyzer capacity, with installation adding another 10% to 15%[74]. BoP components such as power electronics, compressors, pumps, and water purification account for approximately 40% to 60% of total installed CAPEX[75]. Electrical energy and deionized water are often referred to as energy and non-energy feedstock, respectively. In most studies, electricity consumption (approximately 50–55 kWh per kilogram of H₂ at steady state) constitutes 60–70% of LCOH under high-utilization scenarios[76]. Other operational cost items, such as water and routine maintenance, account for a lesser share[77]. Seemingly conflicting results have been published regarding the main cost driver of PEM electrolysis. A majority of recent studies identify electricity cost as the dominant factor influencing LCOH. Since a PEM electrolyzer requires about 50–55 kWh of electricity per kilogram of hydrogen (at 68–72% HHV efficiency), even modest changes in power prices can significantly impact LCOH. James et al. (2013) demonstrated through a sensitivity analysis that a 50% increase in electricity costs could raise LCOH by more than \$2/kg[62]. In contrast, Yates et al. (2020) identified electrolyzer system size as the single most important factor affecting hydrogen cost. In their model, scaling the nominal electrolyzer power up by a factor of 10 could reduce LCOH by approximately \$0.3 per kg (all else equal)[78]. Another study by Astriani et al. concluded that LCOH is more sensitive to the electrolyzer's cost than to variations in electricity tariff[67].

Recent TEAs have evolved beyond static analyses by incorporating dynamic operations and renewable integration. Coupling PEM electrolyzers with time-varying tariffs or surplus renewable supply enables high-capacity factor operation during low-price periods, which reduces average electricity costs and LCOH by an additional 5–10%[79]. Offshore wind-direct coupling studies similarly demonstrate that bypassing

grid transmission and directly supplying electrolyzer systems can achieve hydrogen costs as low as \$2.09 per kilogram in optimal locations, compared to \$3.86 per kilogram through onshore transmission[80].

2.3.3 Renewable Energy configuration

Integrating renewable energy variability into TEA frameworks has increasingly become a focal point. A 2024 techno-economic assessment highlighted that PV-wind hybrid systems reduce LCOH to \$3.01/kg by leveraging complementary generation patterns[81]. Hybrid wind-PV scenarios achieve the lowest LCOH due to higher capacity factors and lower electricity prices compared to solar-only systems. The IEEJ study compared "surplus power" (using curtailed renewables) and "stable power" (dedicated renewable plants) configurations. While surplus power reduced electrolyzer capacity factors to 5–13%, stable power designs reached capacity factors of 50–70% by mitigating intermittency, albeit with higher upfront infrastructure costs[82]. Such results are achieved through multi-objective optimization of system design, which accounts for renewable resource variability and storage integration, highlighting the potential of hybrid renewable systems to significantly improve both utilization rates and economic performance for green hydrogen production[66].

Beyond capacity factors, geographic sensitivity analyses have shown that LCOH can vary by \$2–3/kg across different U.S. regions due to differences in renewable resource quality, electricity tariffs, and permitting costs. For instance, wind-rich regions like ERCOT (Texas) achieve LCOH as low as \$3.74/kg with tax credits, while California's higher grid prices and lower wind capacity factors result in costs exceeding \$5/kg[83]. Similarly, regions with frequent negative electricity prices (e.g., western Texas) allow for cheaper hydrogen production by leveraging curtailed renewable energy[13].

A further dimension of recent TEA research involves policy incentives and carbon pricing. The Inflation Reduction Act (IRA) of 2022 introduced production tax credits (PTC) of up to \$3/kg H₂ for electrolyzers sourcing low-carbon electricity, effectively lowering LCOH by 30–50% under favorable conditions[84].

Nevertheless, studies by Bracci (2023) caution that PTC eligibility criteria, such as hourly emissions intensity thresholds, require hourly modeling to capture compliance risk and revenue streams accurately [14], [70]. This motivates coupling TEA with time-resolved emissions data, a complexity seldom addressed in earlier static analyses.

Chapter 3: Materials and Methods

3.0 Description of Framework

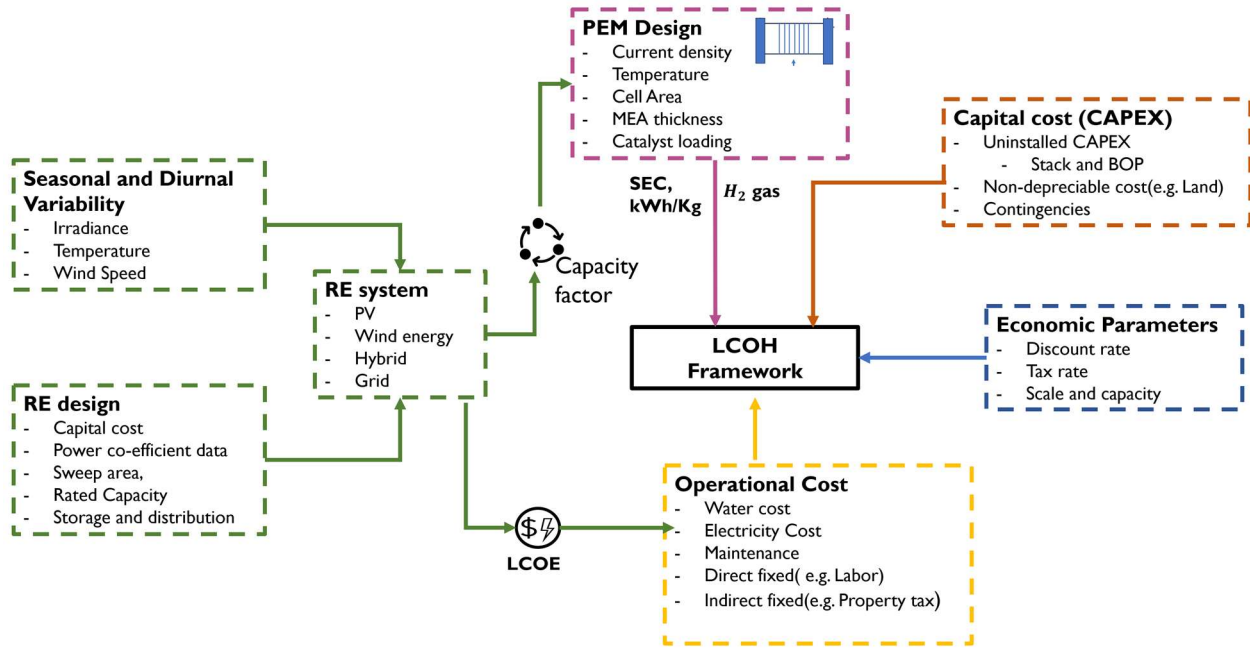


Figure 7: Description of LCOH framework for hourly assessment of green hydrogen production

To deliver a holistic techno-economic evaluation, we developed an integrated modeling framework that couples a validated physics-based PEM electrolyzer model with a system-level discounted-cash-flow (DCF) cost module. As illustrated in Figure 7, the primary dependent variables are the specific energy consumption (SEC), hydrogen output, capacity factor and LCOE. These dynamic variables are influenced by the design parameters from the PEM design module and the RE system module. Capital and operating costs through the economic parameters are annualized and discounted to present value.

The independent variables from the PEM design module, such as the MEA thickness, temperature, and current density, determine the Specific Energy required to produce a unit kilogram of product hydrogen. The sub-system is modeled as an electrochemical reaction, whereas the economic module follows the U.S.

Department of Energy's H2A v3.2018 methodology, adopting its structured input–output architecture and default financial parameters. Uninstalled stack and balance-of-plant capital costs are modified to the system size using a curve-fitting function adopted from literature[67]. It is assumed that both small, distributed units (1,500 kg/day) and large, centralized plants (50,000 kg/day) share a consistent installation cost basis[67]. We then apply installation lang factors, contingency allowances, and non-depreciable land and permitting charges exactly as defined in H2A framework.

On the operating side, the framework ingests an hourly electricity cost time-series from renewable energy (RE) configurations solar PV, wind, and hybrid PV–Wind along with grid tariffs. The seasonal and diurnal modulating factors on the irradiance, temperature and wind speed affect the capacity factor of the energy configuration. Hourly RE generation profiles, obtained from National Renewable Energy Laboratory (NREL) data, are passed through a levelized cost of electricity (LCOE) subroutine to produce weighted average power prices under seasonal and diurnal variability. These dynamic power costs, together with fixed O&M, water treatment, and periodic stack replacement charges, drive the annual cash-flow streams.

We determine the levelized cost of hydrogen (LCOH) from the DCF model. Net present value (NPV) and internal rate of return (IRR) are determined from the same cash-flow series. By linking our physics-based SEC and capacity-factor outputs to a configurable RE supply model and a DCF model, this framework allows us to explore how design choices, cell area, catalyst loading, power electronics efficiency, and energy-supply scenarios jointly influence LCOH, NPV, and IRR.

The following sections outline the design basis and assumptions used in this framework to analyze the economies of scale (Section 4.5) and renewable integration strategies (Section 5.2).

3.1 Mathematical Modelling

3.1.1 Electrolyzer Model Design

Theoretically, the minimum voltage required to initiate the reaction under ideal conditions, without any energy losses, is the reversible voltage V_{rev}

$$V_{rev} = \frac{\Delta G}{zF} = 1.23 \quad (4)$$

where z , is the number of moles of electrons transferred ($z=2$). The voltage needed to sustain the electrochemical reaction at a constant temperature where the heat produced by the reaction exactly equals the heat consumed is the thermoneutral voltage, given as:

$$V_{th} = \frac{\Delta H}{zF} = 1.48 \text{ V} \quad (5)$$

The total cell voltage needed for the electrochemical reaction is the sum of the ideal voltage and the overpotentials caused by the cell's design. Overpotentials are mainly due to the inefficiencies of electrode and electrolyte design materials[85]. The design overpotentials are classified as activation, ohmic, and concentration overpotentials.

3.1.1.1 The Open circuit (reversible voltage)

The Nernst equation relates the system's temperature and pressure to the reversible open-circuit voltage. At standard conditions (1 atm, 298 K) with liquid water as the product, $V \approx 1.229 \text{ V}$ [15].

$$V_{rev} = V_{rev}^0 + \frac{RT}{zF} \ln \left(\frac{\alpha_{H_2} \sqrt{\alpha_{O_2}}}{\alpha_{H_2O}} \right) \quad (6)$$

where V_{rev}^0 is the standard potential (≈ 1.23 V for the PEM reaction), R is the gas constant, F is Faraday's constant, and a_i as the activities of H_2 , O_2 , and H_2O . For gases, $\alpha_{gas} \approx \frac{p_{gas}}{p^0}$ (the ratio of partial pressure to standard pressure), and for liquid water, $\alpha_{H_2O} \approx 1$.

$$V_{rev} = V_{rev}^0 + \frac{RT}{zF} \ln \left(\frac{p_{H_2} \cdot \sqrt{p_{O_2}}}{\alpha_{H_2O}} \right) \quad (7)$$

The reversible voltage at STP is related as[15]:

$$V_{rev}^0 = 1.229 - 0.09 \times 10^{-3}(T - 298.0) \quad (8)$$

Theoretically, pressure has a lesser impact on the V_{rev} than temperature due to the logarithmic term. Higher hydrogen or oxygen pressure raises the open-circuit voltage, while more water inlet lowers it.

3.1.1.2 Activation Overpotentials

The Butler-Volmer equation describes the voltage drop when current flows between the two half-cells due to kinetic inefficiencies. The activation overpotential (V_{act}) results from the energy required to drive the slowest reaction step. The reaction at the anode half-cell limits the kinetics and is the main contributor to the total activation overpotential, while the Pt/C catalyst influences the kinetics at the cathode[86].

$$i = i_0 \left[\exp \left(\frac{\alpha_a z F V_{act}}{RT} \right) - \exp \left(\frac{-\alpha_c z F V_{act}}{RT} \right) \right] \quad (9)$$

α_a , α_c are anodic and cathodic charge transfer coefficients ($\alpha_a = 2.0$, $\alpha_c = 0.5$)[87][15]. The exchange current density (i_0) describes the current at the anode coming into equilibrium with the current at the cathode.

The oxygen anode, $i_{0,anode}$, is several orders of magnitude lower than $i_{0,cathode}$, making the anode activation loss dominant[88][89]. Enhancing the anode exchange current density (i_0) to accelerate the oxygen evolution reaction (OER) effectively can reduce the overpotential ($V_{act,anode}$). Exchange current density

and activation energy values for both the cathode and anode reactions adopted for this model are reported in the Appendix A. 2.

For the anode and cathode half-cells:

$$V_{act} = V_{act,a} + V_{act,c} \quad (10)$$

$$V_{act,a} = \frac{RT_a}{\alpha_a F} \sinh^{-1} \left(\frac{i}{2i_{0,a}} \right) = \frac{RT_a}{\alpha_a F} \ln \left(\frac{i}{2i_{0,a}} + \sqrt{1 + \left(\frac{i}{2i_{0,a}} \right)^2} \right) \quad (11)$$

$$V_{act,c} = \frac{RT_c}{\alpha_c F} \sinh^{-1} \left(\frac{i}{2i_{0,c}} \right) = \frac{RT_c}{\alpha_c F} \ln \left(\frac{i}{2i_{0,c}} + \sqrt{1 + \left(\frac{i}{2i_{0,c}} \right)^2} \right) \quad (12)$$

$V_{act,a}$, $V_{act,c}$, T_a , and T_c are the anode and cathode voltages, and the anode and cathode operating temperatures, respectively. The equation is further simplified to the Tafel equation in a more dominant anodic effect:

$$V_{act,anode} \approx \frac{RT}{\alpha_a F} \ln \left(\frac{i}{i_{0,an}} \right) \quad (13)$$

with $i_{0,an} = K_{i_{0,an}} \cdot \exp \left(\frac{E_{act,an}}{RT} \right)$ referenced to the pre-exponential factor ($K_{i_{0,an}}$) measured in 21600000 A/cm² and the activation energy ($E_{act,anode}$) at 76,000 J/mol[90].

3.1.1.3 Ohmic Overpotentials

Ohmic overpotential V_{ohm} is caused by resistive losses in the ionic and electronic conducting parts of the cell. Ohmic loss is modeled using Ohm's law.

$$V_{ohm} = I \cdot R_{total} = V_{ohm,a} + V_{ohm,c} + V_{ohm,m} \quad (14)$$

where I is the cell current (A) for $I = i \cdot A_{cell}$, and R_{total} is the total internal resistance (Ω) that opposes the flow of electrons. The total resistance depends on the membrane electrolyte (R_m), the porous-electrode (GDL + CL) layers (R_{elec}), the interfacial contact resistance ($R_{in,}$) and the resistance from the bipolar plates (R_{bpp}) .

$$R_{total} = R_a + R_c + R_m = (R_{bpp,a} + R_{elec,a} + R_{in,a}) + (R_{bpp,c} + R_{elec,c} + R_{in,c}) + R_m \quad (15)$$

The resistance of the membrane is:

$$R_m = \frac{t_m}{\sigma_m \cdot A_{cell}} \quad (16)$$

where t_m is membrane thickness in micrometers (μm), and σ_m is the proton conductivity of the material used, measured in Siemens per centimeter (S/cm). The membrane conductivity is modeled as a function of temperature and water content[91]. A membrane's hydration (λ) informs the ionic conductivity σ_{mem} , described by[92]

$$\sigma_{mem} = (0.0051392\lambda - 0.0005326) \cdot \exp\left(1.268\left(\frac{1}{303} - \frac{1}{T}\right)\right) \quad (17)$$

This expression is valid for $5 \leq \lambda \leq 22$ and $30^\circ C \leq T \leq 120^\circ C$. A well-hydrated membrane has high σ_{mem} (0.1 S/cm); if λ decreases (dry membrane), σ_{mem} falls, and ohmic losses increase steeply[92].

The resistivity in the electrode catalyst layer, determined by the material resistivity (ρ_{el}), is expressed as a function of electrode properties. (t_{el}) is the electrode thickness in centimeters (cm), and the catalyst layer resistance is

$$R_{elec} = \frac{t_{el}}{A_{cell}} \cdot \rho_{el} \quad (18)$$

The total voltage drop due to ohmic resistance in the cathode and anode of the electrodes is determined as

$$V_{ohm,cat} = V_{ohm,an} = \rho_{el} \cdot t_{el} \cdot i \quad (19)$$

A more detailed breakdown of the total resistivity is required to allow for modular design and for future expansion on alternative components. The distributed resistance along the flow-field length and channels is shown in Figure 8[93].

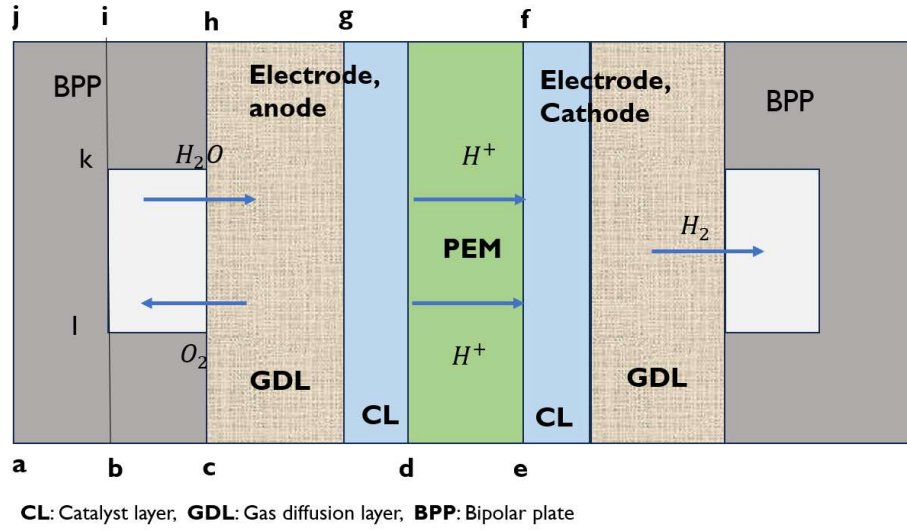


Figure 8: Cross-sectional diagram of a Proton Exchange Membrane (PEM) electrolyzer for internal resistance analysis[93]

The total plate resistance along the flow-field length L_{ab} is expressed as,

$$R_{bpp1} = \rho_p \frac{L_{ab}}{A} \quad (20)$$

$$R_{bpp2} = \rho_p \frac{L_{bc}}{0.5 L_{ik} L} \quad (21)$$

The resistance from the electrodes to the gas channel, in-plane r , and through-plane is given as[93],

$$R_{e1ec1} = \rho_e \frac{0.25 L_{kl}}{t_{el} L (1 - \epsilon)} \quad (22)$$

$$R_{elec} = \rho_e \frac{t_{el}}{0.5 L_{km} L (1 - \varepsilon)} \quad (23)$$

$$R_{elec3} = \rho_e \frac{t_{el}}{L_{kl} L (1 - \varepsilon)} \quad (24)$$

Whereas the interfacial resistance is empirically set as twice the through-plane electrode resistance, $R_{in} = 2R_{e2}$, to fit polarization data[87].

3.1.1.4 Mass Transport (Concentration) Losses

At high current densities, reactant consumption can create concentration gradients and cause depletion near the electrodes, leading to additional overpotential. When the reactant supply rate cannot meet the demand, the local partial pressure (or concentration) at the catalyst decreases, effectively lowering the cell voltage. We assume a limiting current density i_L of 6 A/cm², and the total loss can be written as[94]:

$$V_{conc} = -\frac{RT}{zF} \ln \left(1 - \frac{i}{i_L} \right) \quad (25)$$

The voltage loss increases as the current density approaches the limiting current density.

3.1.1.5 Overall Cell Voltage and Efficiencies

By combining these contributions, the instantaneous total voltage under steady-state conditions for a number of cells (N_{cell}) is:

$$V_{cell} = V_{rev} + V_{act, anode} + V_{act, cathode} + V_{ohm} + V_{conc} \quad (26)$$

$$V_{stack} = N_{cell} V_{cell} \quad (27)$$

Faradaic Efficiency

We define a Faraday efficiency, η_F , to account for current losses such as hydrogen crossover or internal shunt current. This represents the fraction of the applied current that produces the target reaction products.

$$\eta_F = \frac{\text{actual reaction current}}{\text{total current}} = 1 - \frac{i_{\text{loss}}}{i} \quad (28)$$

where i_{loss} is the parasitic current density associated with side reactions or crossover. A high-quality membrane, thicker or less permeable, and lower differential pressure enhance η_F by decreasing crossover. In practice, Faraday efficiency in modern PEM electrolyzers can surpass 98–99% at high current density but diminishes at low loads or high pressure due to increased crossover[95]. Faradaic losses appear as reduced hydrogen production (or lower fuel cell current for a given fuel feed) and are modeled here as an efficiency loss rather than a direct voltage decrease term.

3.1.1.6 The Mass and Energy Balance

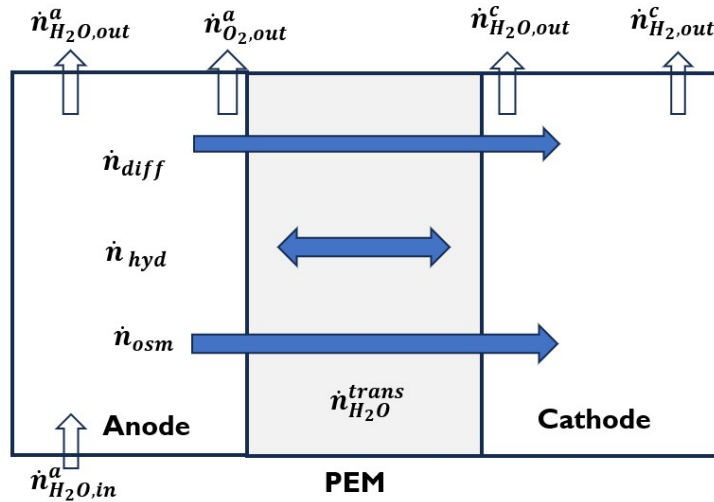


Figure 9: A diagram illustrating the primary water transport mechanisms across the membrane in a PEM water electrolyzer.

The reactant water ($\dot{n}_{H_2O, in}^a$) supplied to the anode half-cell and is consumed to produce oxygen and protons. The oxygen and water are recirculated from the anode half-cell through the gas separator.

$$\dot{n}_{O_2, out}^a = \dot{n}_{O_2, in}^a + \frac{iA_{cell}}{4F} \quad (29)$$

$$\dot{n}_{H_2O, out}^a = \dot{n}_{H_2O, in}^a - \frac{iA_{cell}}{2F} - \dot{n}_{H_2O}^{trans} \quad (30)$$

Water crosses through the membrane via multiple mechanisms: electro-osmotic drag (\dot{n}_{osm}), back-diffusion (\dot{n}_{diff}), and hydraulic permeation (\dot{n}_{hyd}), though electro-osmotic drag is the dominant mechanism.

$$\dot{n}_{H_2O}^{trans} = \dot{n}_{osm} + \dot{n}_{diff} + \dot{n}_{hyd} \quad (31)$$

$$\dot{n}_{osm} = \frac{n_d i}{F} \cdot A_{cell}, \quad (32)$$

The electroosmotic drag coefficient (n_d) quantifies the amount of water molecules transported through a membrane per proton. Water molecules are carried along with protons across the membrane from anode to cathode by electro-osmotic drag (\dot{n}_{osm} (mol/s)).

$$n_d(T) = 0.0134 T + 0.03 \quad (T \text{ in } ^\circ C) \quad (33)$$

[96] When the cathode side gets very moist with a concentration difference, water tends to diffuse across the membrane. (\dot{n}_{diff}) represents the molar flow due to the concentration gradient between the half cells.

$$\dot{n}_{diff} = -D_w \frac{dC_w}{dx} \cdot A_{cell} \quad (34)$$

where C_w is the water concentration in the membrane, often written in terms (λ) number of water molecules per sulfonic acid group[91].

$$\dot{n}_{diff} = - \frac{D_\lambda \rho_{dry}}{EW} \frac{d\lambda}{dx} \cdot A_{cell}, \quad (35)$$

ρ_{dry} represents the dry membrane density and EW , the equivalent weight (kg/mol of sulfonic acid[91].

Hydraulic crossover occurs due to the pressure difference across the membrane. This is modeled by Darcy's law for flow through a porous medium[97].

$$n_{\text{hyd}} = -\frac{K_{\text{mem}}}{\mu_w} \Delta p \cdot A_{\text{cell}} \quad (36)$$

Where K_{mem} is the effective permeability of the membrane to water, and μ_w water viscosity. Darcy-driven water flux is generally small in PEM fuel cells, but in water electrolyzers with thin membranes at high differential pressure, it can contribute to additional hydrogen crossover.

Hydrogen and oxygen leave the cathode half-cell and are further processed and recirculated in the H_2 gas separator.

$$n_{\text{H}_2, \text{out}}^c = n_{\text{H}_2, \text{in}}^c + \frac{iA_{\text{cell}}}{2F} \quad (37)$$

$$n_{\text{H}_2\text{O}, \text{out}}^c = n_{\text{H}_2\text{O}, \text{in}}^c + n_{\text{H}_2\text{O}}^{\text{trans}} \quad (38)$$

The energy balance of a PEM cell

A PEM cell generates heat from multiple sources: (i) the reaction enthalpy that is not converted to electrical work, (ii) Joule heating from ohmic losses, and (iii) any heat from mixing or phase change (e.g., water evaporation/condensation). The difference between ΔH and ΔG is released as heat even at open circuit (eqn 1-6). Additional overpotential losses further convert electrical energy into heat. Therefore, the rate of heat generation in a single cell, Q_{gen} , due to the cell operating voltage exceeding the thermoneutral voltage.

$$Q_{\text{gen}} = I \cdot (V_{\text{cell}} - V_{th}) \quad (39)$$

The total temperature of the cell is determined by an energy balance that includes heat generation, heat removal, and energy flow from the reactant and product streams. We assume the cell has a uniform temperature. For a lumped cell mass m with heat capacity C_p

$$mC_p \frac{dT}{dt} = Q_{\text{gen}} - Q_{\text{cool}} - Q_{\text{env}}, \quad (40)$$

where Q_{cool} is heat removed by a coolant and Q_{env} is losses to ambient (convection, radiation). We assume steady-state is reached when generation equals removal. The bipolar plates are used to dissipate heat and maintain a uniform temperature. Non-uniform temperature can cause dry spots or flooding in different areas, so thermal management aims to keep the cell at an optimal temperature (often $\sim 60\text{--}80\text{ }^\circ\text{C}$)[98].

3.1.1.6 Electrolyzer Model Validation and Sensitivity

We compared the model's predictions against experimental polarization curves from Debe et al. (2024) of a Nafion 117 membrane (178 μm thick) at ambient pressure and temperatures of 23 K (50 $^\circ\text{C}$) and 353 K (80 $^\circ\text{C}$), over current densities up to 2 A/cm²[99]. Other secondary sources of experimental data were considered[79], [100], [101]. The validation focused on reproducing polarization curves (cell voltage vs. current density) and Faradaic efficiency across a range of temperatures, pressures, and catalyst loadings. A local sensitivity analysis examined the influence of uncertainties in exchange current density, membrane thickness, and temperature on cell voltage.

3.1.2 Energy System Design

The following subsections hold the design model for the photovoltaic power system and the wind turbine design model, as well as the interoperability with grid connection.

3.1.2.1 Photovoltaic (PV) Power Model

The goal of modeling the photovoltaic (PV) system is to accurately estimate electricity generation from solar energy to incorporate into the hydrogen analyses. The output power of the PV depends on the solar irradiance incident on the PV array and the module's temperature. The hourly and yearly PV power output can be represented as[102]

$$P_{PV,hY} = P_{STC,rated} \cdot f_{derPV,y} \frac{GTI_h}{G_{STC}} \left(1 + \alpha_p (T_{PV,cell}^h - T_{STC}) \right) p_{losses} \quad (43)$$

$P_{STC,rated}$ indicates the rated peak capacity of the PV system under standard test conditions (STC) at 1 MW.

To account for the reduction in module efficiency over time, we assume an annual derating factor $f_{derPV,y} \approx 0.90$. The global tilted irradiance (GTI_h), measured in kW/m², describes the solar radiation incident on the tilted photovoltaic module surfaces during hour h . Solar irradiance data, which is often available online, is usually given as global horizontal irradiance (GHI). Therefore, to obtain the global tilted irradiance (GTI), this data is adjusted based on the tilt and orientation of the solar panels. This conversion involves correcting for the module's tilt angle and solar geometry, using the following equation[103]:

$$GTI = GHI \frac{\sin(\sigma + \theta_{PV})}{\sin \sigma} \quad (41)$$

Here, θ_{PV} is the angle at which the photovoltaic panels are tilted relative to the horizontal. σ represents the angle of solar elevation, defined as[104]:

$$\sigma = 90 - \phi + \delta \quad (42)$$

ϕ indicates the latitude of the installation site, while δ represents the solar declination angle, which varies throughout the year and is defined as[104]

$$\delta = 23.4 \cos \left(\frac{360}{365} (d + 284) \right) \quad (43)}$$

corresponding to the day number of the year from 1 through 365.

The cell temperature ($T_{PV,cell}^h$) influences efficiency and energy output, adjusted against the standard temperature conditions ($T_{STC} = 25^\circ\text{C}$) through the temperature coefficient $\alpha_p \approx -0.0035/^\circ\text{C}$ [105][106].

$$T_{PV,cell}^h = T_{amb}^h + \frac{\text{NOCT} - 20}{800} G[h] \quad (44)$$

with T_{amb}^h modeled as a seasonal sine wave to reflect seasonal variations and Nominal Operating Cell Temperature (NOCT) in Celsius. $G[h]$ represents the global tilted irradiance GTI_h from Equation (44), measured in W/m^2 . Systematic losses such as inverter efficiency, cable losses, and thermal effects are included as p_{losses} . Incorporating these losses improves the accuracy and usability of the PV model, ensuring comprehensive evaluation and reliable results when used in broader energy system simulations and analyses. All assumptions are provided in Appendix A. 5

3.1.2.2 Wind Power Model

The surrogate modeling of wind energy generation involves calculating the wind turbine's power output as a function of wind speed, considering several performance-related factors. The relationship used to determine the wind turbine power output (P_{WT}) at any given moment is governed by the Betz-Lanchester equation as[107]:

$$P_{WT} = 0.5\eta_{WT} \cdot \rho A C_p(\omega, \beta) v^3 \quad (45)$$

The mechanical efficiency (η_{WT}) accounts for energy losses in critical mechanical components like gearboxes and drivetrains, directly affecting the effective power available from wind energy conversion. The air density (ρ) is approximated at $1.225 \text{ kg}/\text{m}^3$, is crucial since denser air carries more kinetic energy, significantly impacting power output[108]. The swept area (A) of 3000 m^2 is assumed as the circular area created by the rotating turbine blades and determines how much wind is intercepted[109]. The power coefficient ($C_p(\omega, \beta)$) captures the aerodynamic efficiency of the turbine and varies based on the tip speed

ratio (ω) and blade pitch angle (β). (ω) is the ratio of the blade tip speed to the wind speed, while (β) adjusts the blades' orientation relative to the wind flow to optimize efficiency. The polynomial power coefficient curves adopted from literature are summarized in Appendix A. 7[110]

$$C_p(\omega, \beta) = k_0 \left(\frac{k_1}{\omega_i} - k_2\beta - k_3\beta\omega_i - k_4\omega_i^{c_5} - k_6 \right) e^{-\frac{k_7}{\omega_i}} + k_8\omega \quad (46)$$

where:

$$\frac{1}{\omega_i} = \frac{1}{\omega + k_9\beta + k_{10}} - \frac{k_{11}}{1 + \beta^3} \quad (47)$$

Lastly, wind speed (v), (m/s) critically influences power output, as the cubic term shows that even small changes in wind speed can greatly affect the available power. The distribution of wind speeds v is well-modeled by a Weibull probability density[111].

$$f(v) = \frac{k}{\lambda} \left(\frac{v}{\lambda} \right)^{k-1} \exp[-(v/\lambda)^k], \quad v \geq 0, \quad (48)$$

where λ is the scale parameter (the average wind speed), and k is the shape parameter[111]. Seasonal and diurnal modulating factors are applied to the local wind velocity[112]. The wind velocity is further adjusted based on the height of the turbine above ground level[113]. We limited the design to the cut-in/cut-out constraints for a 1 MW turbine to protect it from structural stress such that.

$$P_{WT} = \begin{cases} 0, & v < v_{in}, v > v_{out} \\ P_{WT(v)}, & v_{in} \leq v \leq v_r \\ P_{WT, rated}, & v_r \leq v \leq v_{out} \end{cases} \quad (49)$$

No output is generated when wind speeds are below the cut-in speed (v_{in}) or above the cut-out speed (v_{out}). Between the rated speed (v_r) and the cut-out speed (v_{out}), the turbine operates at its constant rated power ($P_{WT, rated}$). For wind speeds between cut-in (v_{in}) and rated speed (v_r), the output power follows the curve $P_{WT}(v)$, assuming that A , ρ , and C_p remain effectively constant. $P_{WT}(v)$ refers to the power from by the

Betz-Lanchester equation. This helps with forecasting and facilitates the effective integration of wind power within the broader energy system analysis.

3.1.2.3 Integration of Renewable Energy Plant Outputs

The total power output of the renewable energy (RE) plant, comprising both photovoltaic and wind energy systems, must be measured to evaluate the overall energy balance at each hour (h) of the year (y). The total RE power output ($P_{RE,h,y}$) is thus calculated as:[67]

$$P_{RE,h,y} = P_{PV,h,y} + P_{WT,h,y} \quad (50)$$

To maintain continuous operation of the electrolyzer, which requires stable power input within the operational constraints of 5% to 100% of its rated capacity ($P_{PEMsys,rated}$), supplementary power from the upstream electrical grid may be necessary[67]. Therefore, the imported power ($P_{import,h,y}$) from the grid is calculated based on the electrolyzer's minimum operational limit as follows:

$$P_{import,h,y} = \begin{cases} (0.05 \cdot P_{PEMsys,rated}) - P_{RE,h,y}, & \text{if } P_{RE,h,y} < (0.05 \cdot P_{PEMsys,rated}) \\ 0, & \text{otherwise} \end{cases} \quad (51)$$

When the renewable energy production falls below the electrolyzer's minimum operational threshold, the deficit is compensated by importing power from the grid. Conversely, when renewable energy production surpasses the electrolyzer's maximum operational capacity (rated power $P_{PEMsys,rated}$) the excess electricity is directed back to the electrical grid. The exported power ($P_{export,h,y}$) in such scenarios is calculated by:

$$P_{export,h,y} = \begin{cases} P_{RE,h,y} - P_{PEMsys,rated}, & \text{if } P_{RE,h,y} > P_{PEMsys,rated} \\ 0, & \text{otherwise} \end{cases} \quad (52)$$

This comprehensive methodology allows for detailed assessments of system performance, stability, and economic viability across different operational conditions and renewable energy availability.

3.2 Technoeconomic Analysis and Framework

3.2.1 Design Basis

A plant capable of producing 10,000 kg H₂/day, is chosen as the pre-optimal midpoint between small-scale (1,500 kg/day) and large-scale (50,000 kg/day) facilities to balance economies of scale against[74]. The boundary mirrors DOE H2A PEM case studies for distributed and central hydrogen production systems. The baseline capacity reflects the inflection point at which diminishing returns begin to outweigh cost savings from further scaling. The basis allows co-location with wind or solar farms or to be embedded at industrial sites.

Table 1: Parameters for distributed, baseline and centralized hydrogen production systems

Parameters	Distributed	Baseline	Centralized
Production capacity, kg/day	1,500	10,000	50,000
Start-up Year	2024	2024	2024
Total Uninstalled Capital (\$/kW)	2000	\$995	708
Total Electrical Usage (kWh/kg)	54.3	54.3[% LHV](61%) (% HHV) (72.6%)	54.3
Stack Electrical Usage (kWh/kg)	49	49[% LHV](68%) (% HHV) (80%)	49

3.2.1.1 Process design basis

The electrolyzer stack is operated at 333 K with an anode pressure of 1 bar and a cathode (product) pressure of 30 bar, delivering high-purity hydrogen suitable for downstream applications without additional compression at the plant fence. The validated physics model predicts a specific energy consumption (SEC) of 49 kWh/kg at stack level and 54.3 kWh/kg system-wide once balance-of-plant (BoP) loads are included. Purity exceeds 99.97 % on a dry basis, and Faradaic losses from gas crossover remain below 1 % under these conditions, as corroborated by the Scheepers et al. data set used for model calibration. A nominal capacity factor of 90 % is assumed after the commissioning year, during which production ramps linearly from 50 % of nameplate to full output; BoP and O&M expenditures are scaled accordingly. Water consumption is fixed stoichiometrically at 9 kg H₂O per kilogram of hydrogen plus a 5 % purge allowance for quality control, and oxygen is vented without credit in the baseline scenario.

Table 2: Process design basis for economic analysis

Parameter	Value
Plant Capacity (kg/day)	10 000
The cell operating temperature, T (K)	333.15
The cell operating pressure, P (bar)	1 (anode), 30 (cathode)
The maximum current density (A/cm ²)	2
Exchange current density (A/cm ²)	2.618 x 10 ⁻⁶ (anode), 1.0e-1 (cathode)
Limiting current density (A/cm ²)	6
The electrode thickness (microns)	200
The electrode porosity	0.3
The membrane thickness (microns)	114
Active area (cm ²)	877

Parameter	Value
Cell voltage, V	1.79
Voltage efficiency, V	0.69
Cell Power rating, kW/cell	3.14
Total power rating, kW	19,034
Specific Energy consumption, kWh/kg	49
Membrane type	PFSA, Nafion 117
Hydrogen purity	≥99.999 vol %, ISO 14687-2 Fuel-Cell Grade
Capacity factor	95 % (8322 h/yr)

3.2.1.4 Economic basis

Financial parameters include a weighted average cost of capital (WACC) of 10 %, consistent with comparable industrial projects. We define the minimum acceptable discount-cash-flow rate of return (DCFROR) at 10 % for profitability calculations. Utility costs incorporate electricity (\$0.07/kWh), water treatment, routine maintenance, and membrane/catalyst replacements. Plant profitability is assessed via LCOH, net present value (NPV), and internal rate of return (IRR), with LCOH computed as the ratio of the present value of total lifecycle costs to cumulative hydrogen production over 20 years. Other financial parameters: Stack replacement is scheduled every ten years at 15 % of the initial installed CAPEX to capture membrane and catalyst end-of-life refurbishments.

Table 3: Economic parameters and basis for discounted-cash-flow analysis

Economic variable	Value/assumption
Plant operating life, years	20
Weighted-average cost of capital (WACC)	10 %
Corporate income-tax rate	27 %
Depreciation method	20-year Modified Accelerated Cost Recovery System (MACRS).
Construction period	3 years
Electricity price (grid PPA) , \$/ kWh	0.07
DI-water cost, \$/kg	0.002
Annual O&M (excluding electricity)	2 % of installed capital
Salvage value	0 % of EPC cost (conservative)
Uninstalled capital cost, \$995/kW	995

3.2.2 Process Description

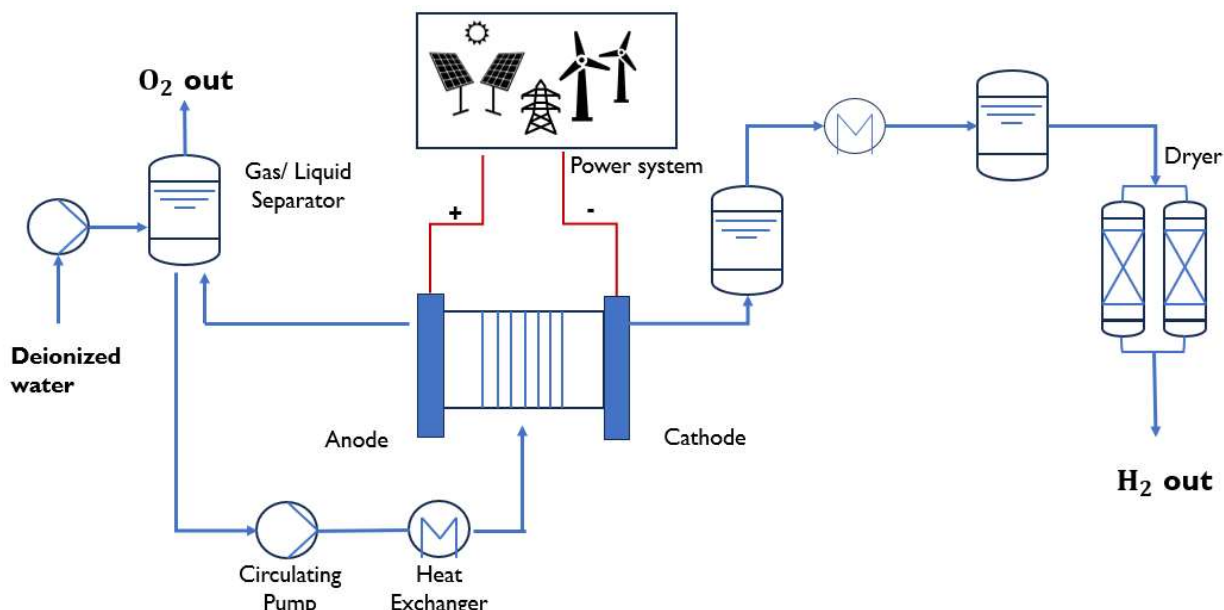


Figure 10: Block flow diagram for PEM electrolysis hydrogen production

Our base-case PEM electrolyzer plant, rated at 10,000 kg H₂/day, follows the flow scheme depicted in Figure 10. Deionized water first enters an ion-exchange pretreatment loop and is pressurized by a high-performance feed pump. It is then preheated through a shell-and-tube heat exchanger to the stack operating temperature of 333 K before distribution to the anode half-cell of the membrane-electrode assembly (MEA). Within the stack, water molecules dissociate under a cell voltage that our validated electrochemical model predicts to be within ± 28 mV of experimental Nafion 117 polarization curves at current densities between 0.5 and 2.0 A/cm²; Faradaic efficiency remains above 99 % and gas crossover stays below 1 %.

On the anode side, evolved oxygen and residual liquid collect in a gas–liquid separator; oxygen is vented through a control valve, while condensate returns to the water loop. At the cathode, hydrogen and entrained moisture pass first through a demister and condensate trap before entering a dual-tower desiccant dryer. The drying stage delivers hydrogen at 30 bar and > 99.97 % purity, ready for distribution without further compression. A continuous bleed equivalent to 5 % of the inlet water flow prevents salt buildup and ensures membrane longevity.

The core electrochemical unit comprises 6186 identical cells connected in series, each featuring a 877 cm² active area. The MEA employs a Nafion 117 membrane with 178 micron thickness, sandwiched between platinum-catalyzed cathodes (0.4 mg/cm²) and iridium-oxide anodes (1.54 mg/cm²). Bipolar plates of titanium with gold-plated flow fields ensure low electrical resistance and corrosion resistance under acidic conditions. Flow-field channels are designed in an interdigitated pattern to optimize water distribution and gas removal, minimizing local flooding and Ohmic losses. Shunt currents are mitigated through insulated manifold designs, preserving cell-to-cell voltage uniformity.

Balance-of-plant components including recirculation pumps, power electronics, separators, and thermal management controls contribute an additional 5.3 kWh/kg to the system-wide specific energy consumption (SEC) of 54.3 kWh/kg. The stack alone consumes 49 kWh/kg for hydrogen generation, corresponding to a 68 % lower heating value (LHV) efficiency at 90 % capacity factor. Startup sequencing ramps production from 50 % to full capacity over the first year, during which O&M costs are scaled to 75 % of steady-state fixed charges and 50 % of variable charges to reflect commissioning activities.

3.3 Scope and Indicators

3.3.1 System Boundary

To ensure clarity and reproducibility, the scope of our analysis is explicitly delimited by a well-defined system boundary that encompasses water treatment, electrolyzer operation, and gas-handling up to the point of dry, high-purity hydrogen at the plant fence. As illustrated in Figure 11, our boundary includes the renewable-or grid-supplied power management system, the PEM stack assembly, the associated water pretreatment train, and the hydrogen and oxygen gas management modules; it excludes downstream compression, transportation, and end-use facilities. By holding the scope fixed, we can transparently compare the techno-economic performance of “green” hydrogen against benchmark cases. (blue hydrogen

produced via steam-methane reforming with carbon capture, and gray hydrogen without capture) on a common basis.

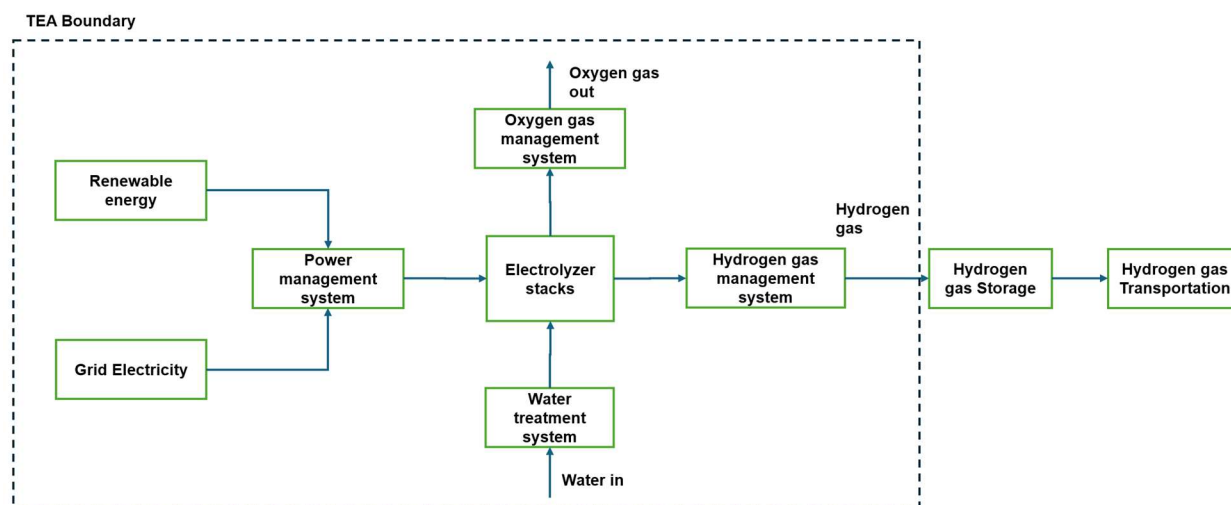


Figure 11: Scope and boundary for TEA of PEM hydrogen production

The time horizon for all cash-flow and environmental indicators spans the 20-year design life of the plant, consistent with IRS MACRS depreciation schedules and H2A Lite conventions. Our analysis is tailored to project developers, policymakers, and industrial offtakers evaluating on-site or near-site hydrogen production options, and thus it focuses on capital and operating parameters most relevant to early-stage deployments. We acknowledge that excluding compression and transportation may understate total system costs for remote or bulk distribution scenarios; this limitation is addressed in our discussion of future work.

The functional unit for comparison is one kilogram of hydrogen delivered at 30 bar and > 99.97 % purity. All mass and energy flows, including feedstock water, electrical input, and by-product oxygen, are normalized to this unit to facilitate benchmarking across scales and technologies. Production capacities of 1,500 kg/day (distributed), 10,000 kg/day (mid-scale), and 50,000 kg/day (central) define three case studies used in our scenario analysis, which probes the impact of economies of scale and renewable-energy penetration on key metrics.

Geographically, we assume a temperate U.S. inland site(the Great Plains archetype) with access to medium-voltage grid infrastructure and typical solar irradiance and wind-speed profiles. Feedstock electricity is modeled under three configurations: grid only, solar-PV only, and a 50:50 PV–wind hybrid, using hourly resource data to capture seasonal and diurnal variability. Water is assumed to meet ultrapure standards after on-site treatment of municipal supply, and purge streams are neutralized within the plant. Waste streams (oxygen vent gas and spent ion-exchange regenerant) are managed per local environmental regulations but are not credited economically.

3.3.2 Metrics

3.3.2.1 Design and System Efficiency

To characterize how effectively the PEM electrolyzer converts input electrical power into chemical energy stored in hydrogen, we define the system efficiency bases on the Lower Heating Value (LHV) and Higher Heating Value (HHV) basis as[68]

$$\eta_{LHV} = \frac{m_{H_2} \cdot LHV_{H_2}}{E_{PEM_{el}} + E_{BoP}} \quad (53)$$

$$\eta_{HHV} = \frac{m_{H_2} \cdot HHV_{H_2}}{E_{PEM_{el}} + E_{BoP}} \quad (54)$$

where $E_{el,h,y}$ is the net electrical input supplied to the stack $E_{PEM_{el}}$ and BoP units E_{BoP} . LHV_{H_2} is the lower heating value of hydrogen, which excludes the latent heat of vaporization of product water, while HHV_{H_2} includes the total energy released during combustion[68]. LHV_{H_2} and HHV_{H_2} are 33.32 kWh/kg 39.44 kWh/kg respectively[94]. These represent the net usable energy at the application.

At standard operation (60–80 °C, ambient pressure), commercial PEM electrolyzers achieve an efficiency of 65–70% HHV, with state-of-the-art systems nearing 80% when integrating waste heat recovery[15].

Generally, LHV-based efficiency is more suitable for fuel cell applications (net power use), while HHV-based efficiency is applied in electrolyzer evaluations, particularly under policy or grid-integration scenarios where the energy source includes renewable generation with seasonal storage requirements. HHV is more appropriate in applications that require the condensation of water vapor, such as in boiler systems[114].

An inverse metric of energy efficiency, Specific Energy Consumption (SEC_{H_2}) is defined as the amount of electrical energy required to produce one kilogram of hydrogen. The total Specific Energy Consumption, $SEC_{H_2 Total}$ Includes the work done by the PEM electrolyzer E_{PEM} and the work done by the BoP E_{BoP} [68]

$$SEC_{H_2 Total} = \frac{E_{PEM} + E_{BoP}}{m_{H_2}} \quad (55)$$

Throughout this study, we report system-wide SEC, including balance-of-plant loads, to facilitate comparisons across scales and energy-supply scenarios.

3.3.2.2 System-level Economic Metrics

To evaluate the financial viability of PEM electrolysis under different energy supply scenarios, we calculate four key economic indicators: levelized cost of hydrogen (LCOH), net present value (NPV), internal rate of return (IRR), and levelized cost of electricity (LCOE). Each of these indicators highlights a unique aspect of project performance over the plant's 20-year lifespan.

Levelized Cost of Hydrogen (LCOH)

The LCOH represents the average cost per kilogram of hydrogen produced, taking into account capital recovery, operation and maintenance, and energy expenses, all discounted to present value. Formally[68]

$$\text{LCOH} = \frac{\sum_{t=0}^N \frac{C_{\text{cap},t} + C_{\text{om},t}}{(1+r)^t}}{\sum_{t=0}^N \frac{M_{\text{H}_2,t}}{(1+r)^t}} \quad (56)$$

where $C_{\text{cap},t}$, and $C_{\text{om},t}$, are the capital-related, O&M, and electricity costs incurred in year t , respectively. $M_{\text{H}_2,t}$ is the mass of hydrogen produced in year t , r is the weighted average cost of capital, and N is the plant life (20 years).

Net Present Value (NPV)

The NPV measures the present-value surplus (or deficit) of cash flows over the project's lifetime. It provides a direct indication of the cumulative value creation by considering the time value of money.

$$\text{NPV} = \sum_{t=0}^n \frac{R_t - C_t}{(1+r)^t} \quad (57)$$

where R_t and C_t are revenues and costs at year, t and is the project lifetime.

The Internal Rate of Return (IRR)

The IRR is defined as the discount rate r that brings the NPV to zero. A higher IRR indicates greater project profitability and risk relative to the WACC benchmark. The lower the IRR the riskier the project, considering the potential annual growth rate.

$$0 = \sum_{t=0}^n \frac{R_t - C_t}{(1 + \text{IRR})^t} \quad (58)$$

Levelized Cost of Electricity (LCOE)

For the renewable energy supply configuration (solar, wind, or hybrid), the LCOE is calculated to evaluate the cost per unit of electricity generated for the PEM electrolyzer system as

$$\text{LCOE} = \frac{\text{CRF} \cdot C_{RE} + O_{RE}}{E_{\text{annual}}} \quad (59)$$

where C_{RE} is the capital cost of the renewable energy plant, O_{RE} is the annual operating cost, and E_{annual} is the annual electricity production. LCOE values are benchmarked against grid electricity tariffs or PPA prices to determine economic competitiveness. The Capital Recovery Factor (CRF) is given as

$$\text{CRF} = \frac{r(1+r)^n}{(1+r)^n - 1} \quad (60)$$

at a discount rate (r) of 0.12, system lifetime (n) of 25 years.

3.4 Cost Modeling

This section will detail the model for operational and capital costs under the economic sub-model.

3.4.1 PEM Capital Cost Sub-model

3.4.1.1 PEM Uninstalled cost

The total uninstalled capital cost of the PEM hydrogen production system consists of the electrolyzer stack and the balance-of-plant (BoP). Following Astriani et al.'s parametric fitting of global cost data, the uninstalled stack cost is expressed as an exponential-linear function of the rated electrical capacity of the electrolyzer (in kW)[67]:

$$\text{Cost}_{EL} = k_1 + k_2 P_{EL,\text{rated}} + k_3 e^{k_4 P_{EL,\text{rated}}} \quad (61)$$

The constants k_1 , k_2 , k_3 , and k_4 are given as 1046.93, -3.48, 2061.57, and -0.26. The fitted constants represent baseline costs, linear scaling factors, and exponential scaling effects. The cost of the PEM electrolyzer system scales rapidly and diminishes with economies of scale for large capacities. The total uninstalled cost includes the balance-of-plant (BoP) components such as gas-liquid separators, compressors, pumps, thermal management systems, and water purification units. The power management system (PMS) constitutes another significant capital investment, involving equipment such as rectifiers and transformers. These components are essential for converting grid-supplied or renewable alternating current (AC) into the direct current (DC) required by the PEM electrolyzer stack. Given the dynamic operating conditions associated with renewable energy integration, PMS configurations must be robust and capable of handling substantial fluctuations in voltage and current, thereby ensuring continuous and reliable electrolyzer operation. The uninstalled cost is then multiplied by a set of "Hand factors" or derived multipliers that convert equipment costs into installed costs. These multipliers account for auxiliary materials, assembly, project engineering, civil work, overheads, supervision, freight, and contingencies.

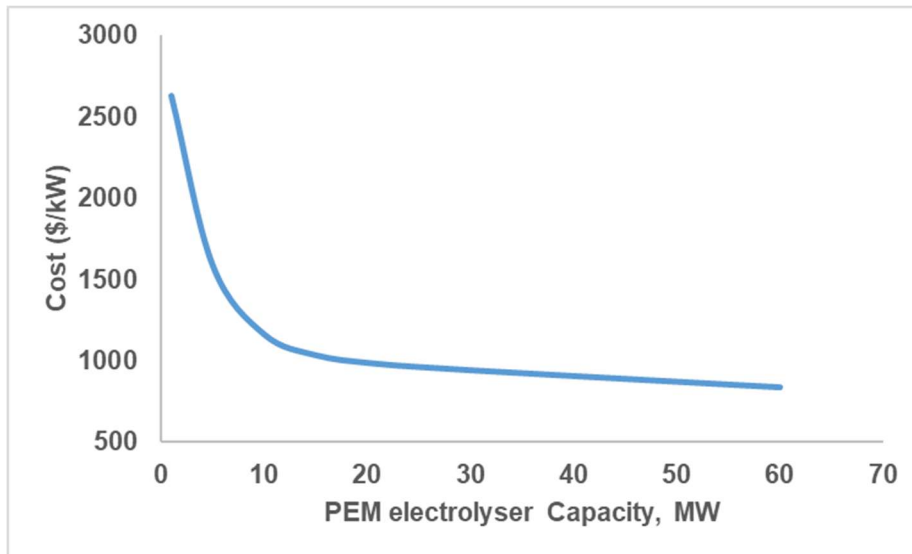


Figure 12: Uninstalled capital cost curve for PEM electrolyzer[67].

3.4.1.2 Renewable Energy System Cost

To account for variable energy supply scenarios, a separate modeling layer is introduced for renewable electricity provision. The RE system includes solar photovoltaic (PV) and onshore wind power as independent and hybrid supply configurations. For each renewable source, the capital cost (C_{RE}) and operating cost O_{RE} are modeled as functions of installed capacity P and scale index s for price corrections, adopting the 6/10 rule:

$$C_{RE} = C_{ref} \cdot \left(\frac{P}{P_{ref}} \right)^{-s} ; \quad O_{RE} = O_{ref} \cdot P \quad (62)$$

The cost of solar PV and wind systems is based on a 1 MW reference scaled to a 20 MW project scale and includes an 8% land procurement cost.[63]. We assume the purchase cost includes the cost of installation. Hybrid power systems that combine solar and wind in a 1:1 capacity ratio were modeled with proportional capital cost contributions and aggregate operational costs. These values serve as input parameters for alternative electrolyzer configurations that rely on an off-grid renewable supply.

All RE investment costs are consolidated into the Levelized Cost of Energy (LCOE) for the hydrogen production system. LCOE for solar, wind, or hybrid configuration is computed to assess the cost per unit of electricity generated

3.4.2 Operational Expenditure

The total OPEX is categorized into fixed and variable components, each representing distinct drivers of annual expenditures. Appendix B. 3 offers a concise summary of the assumptions used to estimate these costs. The fixed costs comprise direct fixed labor and indirect fixed overheads. For labor, we assume a wage rate of \$31.29 per person-hour and staff the plant to ensure that total maintenance labor averages 1,500 man-hours per year. Maintenance is distributed across routine inspections and corrective repairs. Indirect fixed costs include an annual budget of \$50,000 for licensing and permitting, property taxes, and insurance

assessed at 1.5% of total installed CAPEX (approximately \$1.7 million per year), along with facility rent of \$75,000 per year. Together, these direct and indirect fixed charges account for nearly 4% of installed capital each year, providing a stable base load of overhead against which variable costs are measured. These assumptions are all consistent with NREL's 2019 H2A and H2AFAST tools for distributed systems[115].

Variable OPEX is driven by feedstocks, utilities, and consumables that scale directly with hydrogen production. Electricity represents the single largest line item; for grid-connected cases, it is simply the product of SEC and the contracted price. For off-grid cases, we substitute the time-series LCOE developed from the RE sub-model. Water costs encompass three distinct streams: demineralized process water at \$0.002 per liter, cooling-loop water at \$0.0005 per liter, and a small purge stream treated and discharged at \$0.10 per kilogram of spent regenerant. Oxygen vented to the atmosphere carries no economic credit in our baseline but incurs compression power in the event of on-site utilization, which we capture as a variable BoP load. Finally, periodic stack replacements are scheduled every ten years at 15% of the initial CAPEX, entered into the cash-flow model as a lump-sum variable cost in years ten and twenty.

3.5 Parametric Sensitivity and Uncertainty Analysis

Building on the detailed techno-economic framework, we subject key model inputs to both deterministic and probabilistic analysis to ascertain which parameters most strongly influence project economics and to quantify the inherent uncertainty in our LCOH, NPV, and IRR estimates. The basis and ranges for the sensitivity analysis are given in Appendix C. 1

3.5.1 Univariate Sensitivity on key Input Parameters

In the univariate sensitivity analysis, each input parameter is varied independently between low and high bounds while all other assumptions remain fixed at the base value. Each bound represents a scenario reflecting plausible near-term or DOE's technical target under the Hydrogen Earthshot values at their base

case[11]. Figure 17 and Figure 18 present tornado diagrams based on parameter variation and their effect on LCOH and NPV. The plot illustrates Total Energy Feedstock Cost (\$/kWh), Uninstalled Capital Cost (\$/kW), Specific Energy Efficiency (kWh/kg H₂), Tax Rate (%), Total Fixed Operating Costs (\$/yr), Total Utility Costs (\$/year), Total Non-Energy Feedstock (\$/year), and Co-Product O₂ Selling Price (\$/kg O₂). (Appendix C. 1) A scenario comparison between a centralized and a distributed system is compared to the baseline on NPV and IRR.

3.5.2 Multivariate and Montecarlo Simulations

We complemented the univariate study with multivariate and Monte Carlo simulations to capture parameter interactions and probabilistic risk. In a two-dimensional contour analysis, we jointly vary electricity costs and capital expenditures across their respective ranges to generate LCOH contour plots. The contour plot demonstrates the trends and the dominating parameters related to the metrics being assessed (Figure 19, Figure 20)

Chapter 4:

Results and Discussion

4.1 PEM Design Validation and Parameter Sensitivity

A preliminary validation of the electrochemical model is essential before integrating it into the proposed framework. The effect of the design parameter choices is seen in the effect on the study of the polarization curve and the breakdown of the overpotentials that need to be minimized.

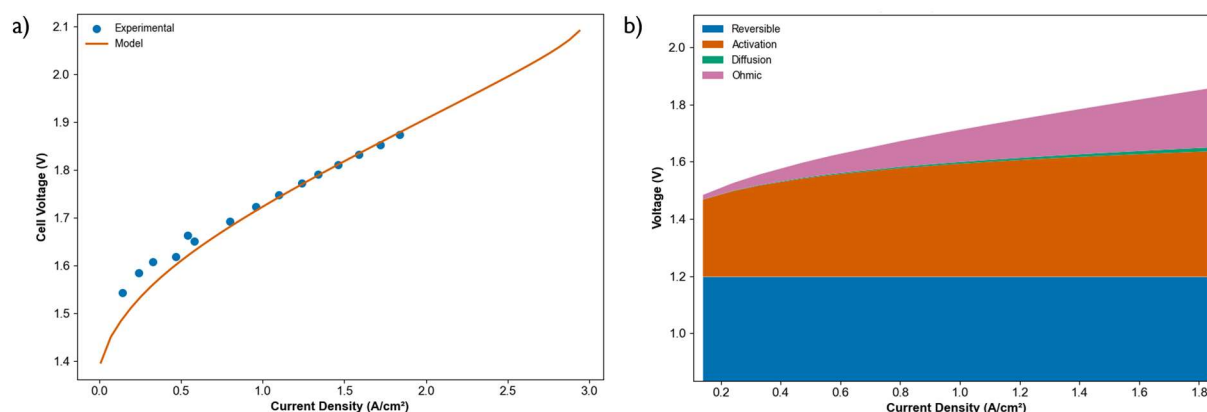


Figure 13: Model validation and voltage loss analysis for a PEM electrolyzer. (a) The polarization curve generated by an electrochemical model (solid line) is compared with experimental data points. (b) A breakdown of the total cell voltage predicted by the model

As shown in Figure 13, the model (solid orange line) tracks the experimental data (blue markers) with high fidelity across the full current-density range. Quantitatively, we achieved an RMSE of 32 mV, an MAE of 28 mV, and an R^2 of 0.897 versus the Debe et al. curves well within the typical experimental variability of commercial PEM stacks[99]. These statistics confirm that our electrochemical model reproduces both the shape and absolute voltage levels of a Nafion 117 membrane operating under realistic conditions.

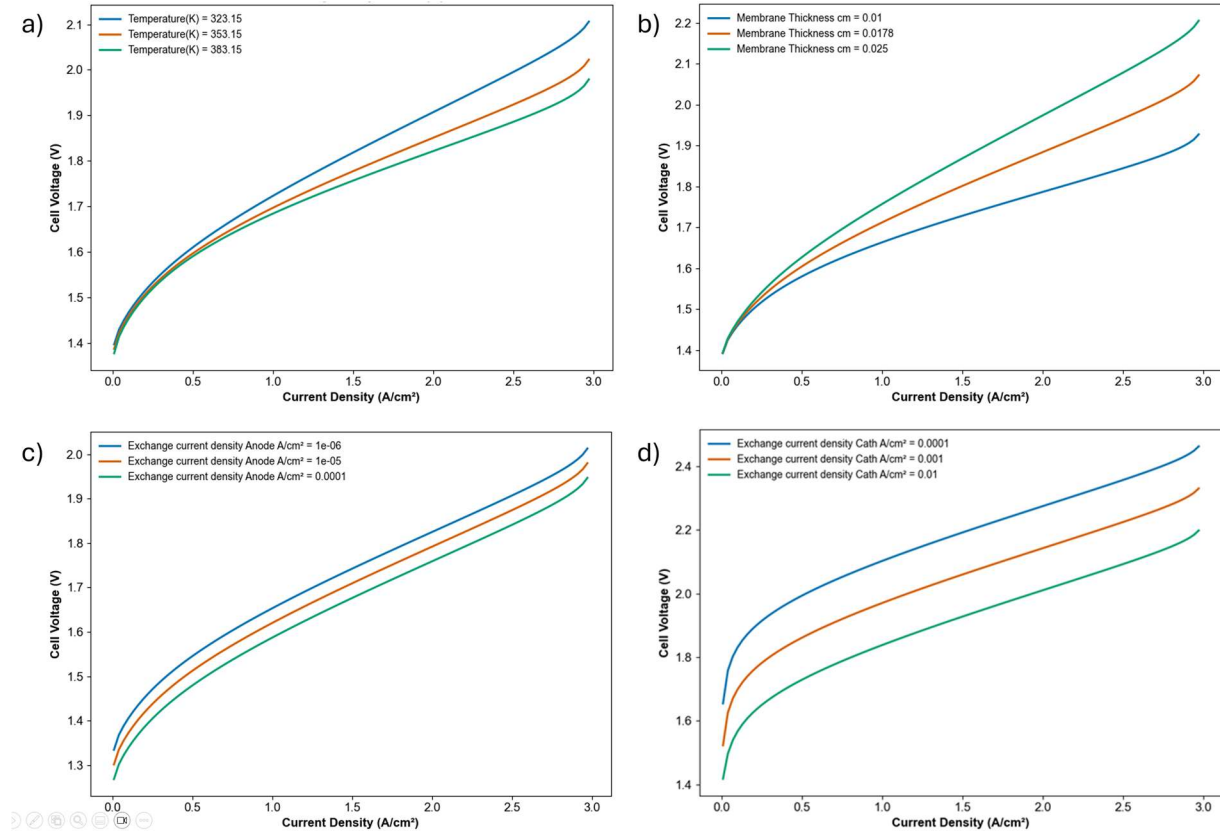


Figure 14: Parametric study of a PEM electrolyzer on cell performance. (a) Temperature Sensitivity, (b) Membrane Thickness Sensitivity, (c) Anode Exchange current density Sensitivity, (d) Cathode Exchange current density Sensitivity

Having validated the core model, we conducted a localized sensitivity analysis to investigate how uncertainties in key parameters affect cell voltage. Figure 14a illustrates the impact of stack temperature: increasing T from 323 K to 383 K reduces cell voltage by up to 70 mV at 2 A/cm², driven by decreased activation overpotential and enhanced conductivity. Figure 14b shows that increasing membrane thickness from 100 to 250 μm adds roughly 120 mV of ohmic loss at high current densities, emphasizing the trade-off between mechanical durability and energy efficiency. Furthermore, Figure 14c demonstrates that reducing the exchange-current density i_0 from 1×10^{-4} to 1×10^{-6} A/cm² increases the low-current-density voltage by nearly 200 mV, underscoring the critical role of catalyst kinetics in minimizing activation losses.

The exchange current density i_0 , which scales with catalyst loading and intrinsic activity, exerts a pronounced effect at low current densities. Reduction in i_0 increases the activation overpotential by roughly 200 mV at 0.2 A/cm² (Figure 14d). This behavior follows directly from the Butler–Volmer relation: lower i_0 slows the electrode reaction kinetics, requiring larger driving voltages to sustain the same current. Optimizing the catalyst layer by increasing active-site density or improving ionomer distribution, therefore raises i_0 and compresses the low-current voltage penalty[86], [100].

The temperature and pressure both influence the thermodynamic and transport terms. Increasing the stack temperature from 323 K to 383 K lowers the activation barrier and enhances membrane conductivity, decreasing cell voltage by up to 70 mV at 2 A/cm² (Figure 14a). Conversely, raising the cathode pressure directly boosts the Nernst open-circuit voltage, as determined by the gas-partial-pressure term. However, higher species pressures can also impede water transport into the electrode pores, worsening diffusion losses, which in turn modestly increase concentration overpotentials at high current densities[87]. High-pressure PEM electrolyzers are beneficial to avoid the high cost of compression prior to storage, transportation, or application[87].

The thickness of the electrode and membrane affects both ohmic and mass-transport resistances. Figure 14 illustrates that increasing the membrane thickness from 100 to 250 μm results in approximately 120 mV of ohmic drop at 2 A/cm², consistent with the expected linear relationship between ionic path length and resistance. Additionally, thicker catalyst layers extend the diffusion pathways for water and produced gases, raising concentration overpotentials and flattening the high-current plateau of the polarization curve[93].

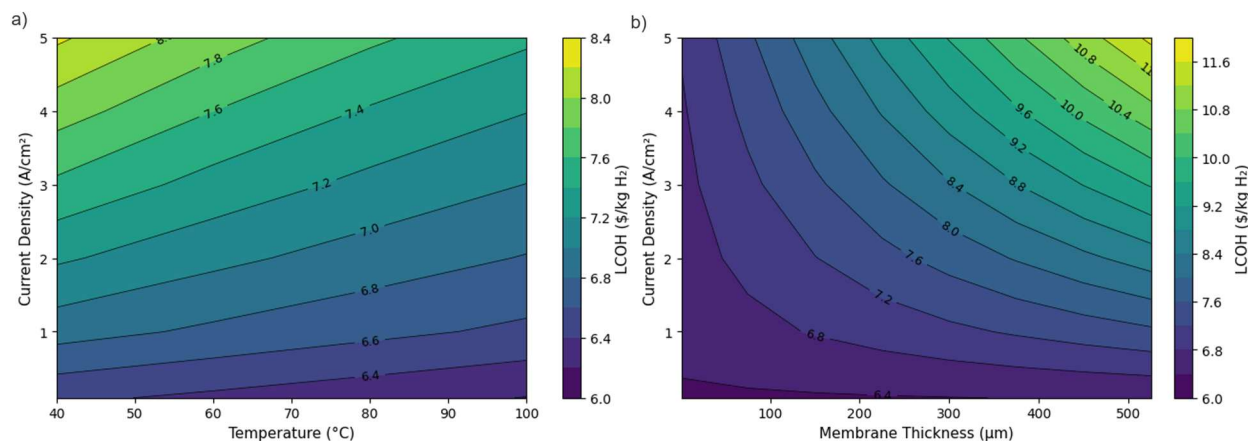


Figure 15: a) Contour of LCOH to Temperature and current density, b) Contour of LCOH to Membrane thickness and current density.

Figure 15a presents the levelized cost of hydrogen (LCOH) as a function of two key PEM electrolyzer operating parameters: cell temperature (40–100 °C) and current density (0.5–5 A/m²). The contour lines span an LCOH range of roughly \$6.0–\$8.4 per kg H₂, illustrating how thermal management and electrochemical design together shape hydrogen economics.

Across the design space (current density from 0.1 to 5 A/cm², temperature from 40 °C to 100 °C), LCOH ranges from approximately \$6.0/kg (low density & high temperature) to \$8.4/kg (high density & low temperature). Higher temperatures reduce both activation overpotentials and membrane resistance, decreasing the specific energy consumption (SEC) by several kWh/kg. At a fixed temperature (e.g., 60 °C), increasing current density from 1 A/cm² to 3 A/cm² raises LCOH by about \$0.8/kg. Higher current densities cause larger kinetic and Ohmic overpotentials, increasing SEC even as the necessary cell-stack area (and thus capital expenditure) decreases. The optimal region is around 1.5–2.5 A/cm² at 60–80 °C, where LCOH is minimized (approximately \$6.5–\$7.0/kg) without significantly increasing either CAPEX through oversized stacks or OPEX through high overpotentials.

Figure 15b shows how membrane thickness (50–550 µm) and operating current density (0.5–5 A/cm²) affect the levelized cost of hydrogen (LCOH) for a proton-exchange-membrane (PEM) electrolyzer. The lowest cost range (\$6.0–\$7.0/kg) occurs with thin membranes (≤ 100 µm) combined with moderate current

density (1–2 A/cm²). For a 100 μ m membrane, increasing from 0.5 to 5 A/cm² raises LCOH from \$6.4 to \$8.8/kg. This increase results from higher kinetic, ohmic, and mass-transport overpotentials, which outweigh the CAPEX benefit of reducing stack area. The lowest LCOH range (\$6.2–6.8/kg) occurs at membrane thicknesses of 125 μ m or less and current densities of 1–2 A/cm². In this zone, ohmic losses stay modest, while capital dilution remains tolerable. Using membranes thinner than 75 μ m offers less than \$0.2/kg in savings but introduces risks related to durability and gas crossover. Commercially available composite PFSA or PFSA-PFPE membranes in the 50–100 μ m range minimize ohmic voltage drops while maintaining mechanical integrity, enabling LCOH reductions of up to \$3/kg compared to stacks over 200 μ m.

4.2. Univariate Sensitivity and Scenario analysis

4.2.1 Centralized , Baseline, and Distributed Scenario Analysis

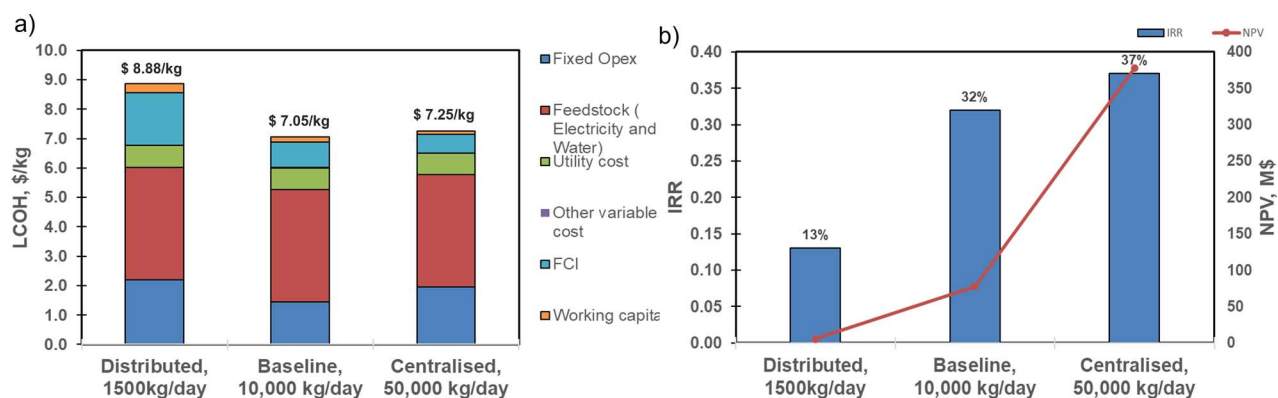


Figure 16: a) LCOH at different plant capacities of 1500kg/day(distributed), 10,000kg/day and 50,000kg/day(centralized). B) The IRR and NPV for distributed and centralized systems

Figure 16a compares the levelized cost of hydrogen (LCOH) and its breakdown across three plant capacities: a small-scale “distributed” unit (1,500 kg/day), our mid-scale “baseline” reference (10,000 kg/day), and a large “centralized” plant (50,000 kg/day). It breaks down each LCOH into its main cost

categories: fixed operating expenditure, electricity feedstock, utilities, other variable costs, fixed-capital investment (FCI) recovery, and working capital.

Moving from the distributed to the mid-scale plant, we observe a significant decline in levelized cost, from approximately \$8.88/kg to \$7.05/kg. Two cost drivers account for most of this 21% reduction. First, economies of scale considerably reduce the cost per kilogram contribution of fixed OPEX and FCI: the larger plant spreads labor, administration, and capital recovery over a production volume nearly seven times greater, compressing those bars in the stacked profile. Second, balance-of-plant components such as the power-conditioning and water-treatment components show sub-linear cost scaling (Section 3.4.1), further lowering capital recovery per unit of hydrogen.

When capacity is expanded an additional five-fold to 50,000 kg/day (centralized system), the LCOH increases only slightly, reaching a minimum of \$7.05–7.25/kg in our model. While fixed costs continue to decrease on a per-kilogram basis, the feedstock electricity bar, already the largest contributor, increases in absolute height due to total power demand rising linearly with output. At the assumed tariff of \$0.07/kWh, electricity accounts for about 53% of the centralized LCOH, consuming most of the savings achieved elsewhere. Thus, the slight increase between the baseline and centralized configurations (\$7.0 → \$7.25/kg) indicates a tipping point at which diminished scale advantages in CAPEX and labor are offset by electrical energy consumption.

Several insights for project developers can be drawn from this scenario analysis. First, right-sizing a plant for a specific offtake avoids both the high unit costs of undersized assets and the electricity-driven economics of mega-scale installations operating at today's power prices. Second, feedstock electricity price volatility becomes more significant than any other single parameter once capacities exceed approximately 10,000 kg/day; subsequent tornado-diagram results (Section 4.2.2) will confirm this dominance quantitatively. Finally, the modest cost penalty of the distributed case highlights its potential niche wherever transport, compression or permitting considerations take precedence over cost minimization.

Distributed systems deliver positive returns but generate limited value, making them suitable for niche applications where co-location or resilience are essential. Mid-scale plants find an optimal balance between high IRR and strong NPV, maximizing both capital efficiency and overall project value under current cost and tariff conditions. Mega-scale installations further increase NPV but offer only marginal IRR improvements, suggesting that developers should carefully consider the additional complexities of permitting, supply-chain logistics, and market offtake before pursuing the largest setups. We acknowledge that larger capacity projects might secure better power purchase agreements, which could change the analysis dynamics. Nonetheless, these results offer a clear decision framework for green-hydrogen investors.

4.2.2 Multi-Scenario Analysis and Sensitivity to LCOH

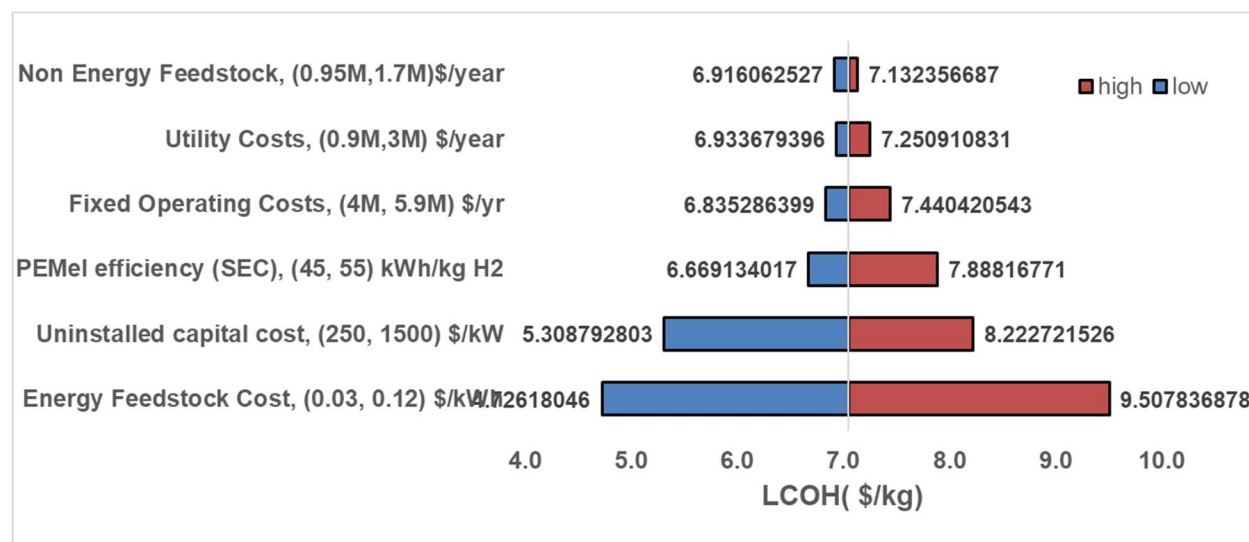


Figure 17: Tornado chart showing a univariate sensitivity of LCOH to key parameters

The span of each bar in Figure 17 can be interpreted as a thought experiment: what would the levelized cost of hydrogen be if a single parameter reflected a plausible “optimistic” future and a conservative “present-day” or “legacy” value, while everything else remained unchanged? Figure 17 shows the predicted changes in hydrogen costs plotted on the x-axis versus various single input factors arrayed along the y-axis. It

specifically shows the sensitivity of Hydrogen production costs to changes in: Total non-energy feedstock, Total utility cost, SEC, Total Fixed Operating cost, Uninstalled capital cost and Total Energy Feedstock cost. Taken together, these outline a band of economic possibilities anchored at our 10,000 kg/day baseline and widening to \$4.7–9.5/kg across the envelope of scenarios. The blue color band indicates optimistic scenarios, whereas the orange color band shows high-end scenarios.

The tornado analysis shows that our cost estimates for hydrogen heavily rely on current market conditions and future technical objectives. In high-end scenarios, where electricity could be priced at \$0.15/kWh in certain states, or installed CAPEX at \$1,500/kW, SEC at 55 kWh/kg, and O&M around 8% of CAPEX, the LCOH might reach \$9.5/kg. Here, the risk for green hydrogen is significant, and special financing or contracts may be needed to achieve acceptable returns. Conversely, in the “low-cost” scenarios, where power can be obtained at \$0.03/kWh during renewable surpluses or if DOE targets for PEM are met (CAPEX \approx \$250/kW and SEC at 45 kWh/kg), or if O&M is optimized to 5% of CAPEX, LCOH could fall below \$5/kg.

Low-power-price scenario (\$0.03/kWh) reflects curtailed-renewable or “overbuild-and-spill” regimes now emerging in regions with high solar penetration (e.g., California’s midday surplus) or in markets where electrolyzers are co-located behind the meter with dedicated PV and wind[116]. In such settings, the plant can procure electricity below the long-run marginal cost of the grid, reducing LCOH to approximately \$4.7/kg. This lower bound is within reach of blue hydrogen under mid-range carbon-capture costs; therefore, projects pursuing a pure-renewables arbitrage strategy can be competitive today without further technological breakthroughs[117]. Conversely, a merchant-grid electrolyzer in a peaking-price region, relying on 24/7 renewable energy certificates, could face tariffs at or above \$0.12/kWh, which could drive the LCOH to nearly \$9.50/kg. This price is significantly higher than that of gray hydrogen produced from SMR, indicating that electricity cost volatility poses the primary threat to project economics whenever low-cost PPAs or behind-the-meter designs are not available. Even small reductions in the average electricity tariff by a point or two of levelized cost of electricity (LCOE) translate almost one-for-one into savings in

hydrogen costs. This will validate business models that emphasize ultra-low-cost, high-capacity-factor power procurement over marginal efficiency gains.

Capital-cost trajectory (\$250/kW) scenarios approximate an optimistic 2030 DOE target that assumes serial production of large-format stacks, thin-film catalyst deposition, and integrated MEA[11]. Achieving this goal could lower LCOH by ~\$1.8/kg relative to today's small-lot quotes of \$1,500/kW, about the same magnitude as a 15% swing in electricity cost. Therefore, manufacturing scale-up offers the second most influential lever after affordable power[118]. While capital cost has a lesser effect than electricity cost, it is greater than any other operational cost. Future breakthroughs in cost optimization for stack manufacturing will more decisively reduce hydrogen prices than incremental gains in water, labor, or utility efficiency. Conversely, if capital falls to DOE's \$250/kW target while mid-continent electricity stabilizes near \$0.05/kWh, LCOH would converge near \$5.3/kg, below the \$5.5–6/kg range, which could be the parity threshold with blue hydrogen under a moderate carbon price.

The fixed operation costs include production expenses that are independent of the amount of hydrogen produced, such as insurance, property taxes, and maintenance contracts. Implementing predictive maintenance, good service contracts, and strategic plant placement could potentially reduce fixed O&M annual expenses by nearly \$2 million for a 20-MW plant. The LCOH benefit (\pm \$0.2/kg) is modest compared to electricity costs or CAPEX but remains strategically important because these savings accumulate and grow each year. The lower end of fixed O&M costs could result in an LCOH of \$6.84/kg. Increasing maintenance and operational costs up to 8% of CAPEX can also raise costs to \$7.44/kg. While these factors are important for project competitiveness, especially for projects using similar power sources, yet they remain secondary compared to the electricity tariff or plant CAPEX.

The benefit of stack efficiency optimization scales with the proportion of electricity costs. The 45 kWh/kg stack efficiency target simulates advanced membrane-electrode assemblies with sub-500 mV cell voltages and improved ohmic conductance. Achieving this performance saves roughly \$0.40/kg off LCOH. Thus, it captures half the gain from meeting DOE's CAPEX target for PEM electrolyzers while simultaneously

reducing cooling load and balance-of-plant (BoP) sizing. Since efficiency gains reduce both variable electricity costs and some capital line items, they remain a worthwhile R&D focus even in low-power-price regions.

In the scenario for utility and non-energy feedstocks, a threefold increase in water and ancillary utility costs affects the LCOH by less than $\pm \$0.15$ per kilogram. This confirms the traditional view that deionized water consumption is economically insignificant (about 2% of total variable cost). However, in arid regions or microgrid deployments where water must be trucked in, these costs could rise and require site-specific analysis. Oxygen as a co-product is excluded from this analysis because it is not directly related to the cost of hydrogen.

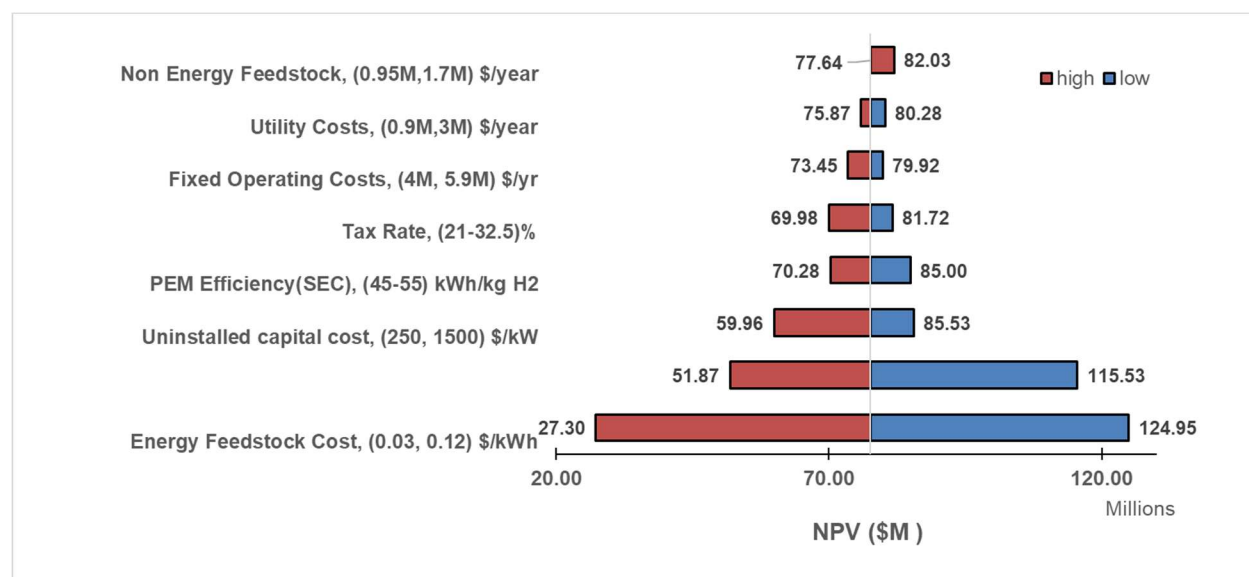


Figure 18: Tornado chart showing a univariate sensitivity of NPV to key parameters

While the previous analysis focuses on how individual parameters affect the levelized cost of hydrogen, project developers and investors ultimately prioritize value creation measured by NPV. Therefore, Figure 18 groups the similar levers based on their impact on the baseline net present value of \$77.6 million. Once again, electricity price stands out as the most critical factor: at a tariff of \$0.03/kWh, the project's cumulative discounted cash surplus rises to \$125 million. Conversely, a steep power cost of \$0.12/kWh nearly erases

profitability, reducing NPV to \$27 million. In other words, a one-cent increase per kilowatt-hour corresponds to roughly \$12 million in project value over twenty years.

Efficiency gains are very important because they can lower electricity consumption and enhance the project's profitability. Improving specific energy consumption from 55 to 45 kWh/kg increases NPV by roughly eight million dollars. However, it's important to note that this is still half the impact of electricity cost. Fixed O&M, utility water, and non-energy consumables alter NPV by no more than \pm \$ 7 million across the realistic bounds we examined, confirming their secondary status in project economics.

We studied how tax policies affect green hydrogen projects under different tax rates. The high-end scenario for taxes and government policies reflects a combined federal and state corporate tax rate for states like California (28.4%), New Jersey (28.0%), and Minnesota (28.5%)[119]. The low-end scenario includes regions with low or no corporate income tax. The tax burden cuts the Net Present Value (NPV) of a green hydrogen project by about \$7-8 million, assuming all other factors stay the same. The tax penalty is similar in effect to small improvements in stack efficiency. In other words, a favorable tax break can offset the costs of running a slightly less efficient electrolyzer, and vice versa. Additionally, this indicates that policy instruments like investment tax credits or accelerated depreciation improve project economics but cannot compensate for unfavorable electricity tariffs.

We also analyzed the valorization of oxygen as a coproduct. Revenue from the sales of oxygen as a coproduct at the rate of \$0.028/kg O₂ gives an additional five million dollars of value. Only at very large scales, where oxygen volumes rival those of a dedicated air-separation unit, would by-product valorization materially shift the investment case. This finding cautions against over-reliance on oxygen credits in proforma statements unless a firm offtake agreement is in place.

Collectively, the LCOH and NPV tornado analyses reveal a consistent hierarchy of sensitivities: electricity cost ranks first, followed by capital cost, while efficiency, O&M, taxation, and ancillary streams lag significantly behind. From an informed perspective, the results indicate that early-stage project screening

should prioritize long-term power price commitments and reliable CAPEX estimates; only when those anchors are favorable do incremental gains in efficiency or fiscal optimization meaningfully enhance financial sustainability.

4.3 Multivariate sensitivity analysis

Figure 19 illustrates the sensitivity of the levelized cost of hydrogen (LCOH) to two key techno-economic drivers: the cost of electrical energy and the design capacity of the electrolyzer. Across the examined parameter space, with design capacities ranging from 2,000 to 15,000 kg H₂/day and electricity prices between \$0.01 and \$0.21 per kWh, the contour lines reveal two fundamental insights. First, the cost of electrical energy proves to be the most influential factor in reducing LCOH. Keeping capacity constant at 10,000 kg/day (the baseline), a decrease in electricity price from \$0.12 to \$0.02 per kWh lowers LCOH from about \$10/kg to below \$4/kg. In contrast, increasing capacity from 5,000 to 15,000 kg/day at a fixed electricity price of \$0.07 per kWh only decreases LCOH by roughly \$1.5/kg. This asymmetric sensitivity highlights that, for green hydrogen systems, obtaining low-cost power through power purchase agreements, grid-side renewables, or behind-the-meter generation is a more effective approach than endless plant upscaling.

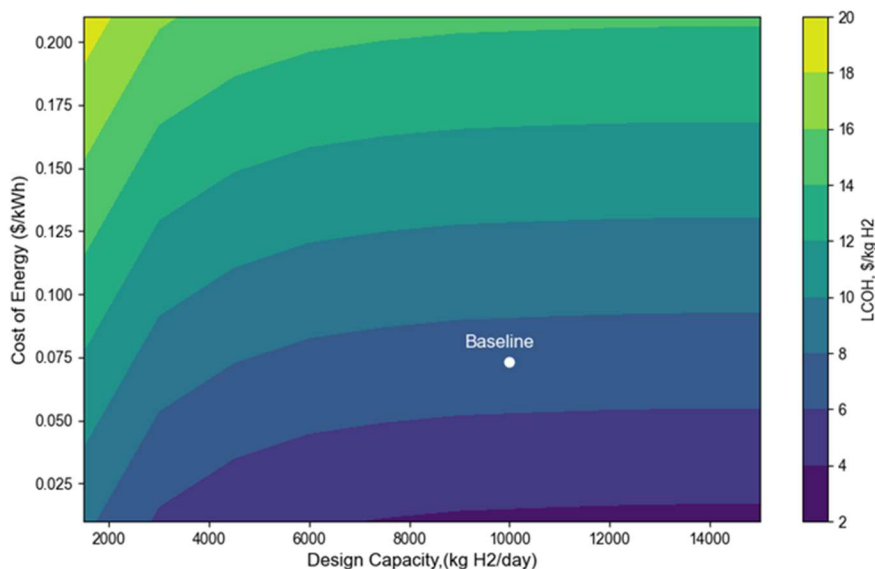


Figure 19: Contour of LCOH (\$/kg H₂) versus design capacity (kg H₂/day) and electricity cost (\$/kWh). The white marker denotes the 10,000 kg/day baseline case at \$0.07 kWh

Second, while economies of scale do reduce unit costs, they show significant diminishing returns beyond approximately 10,000 kg/day. In the lower-left quadrant of Figure 19, small-scale units ($\leq 4,000$ kg/day) see steep LCOH declines of \$2–3/kg for each additional 2,000 kg/day of capacity. However, after 10,000 kg/day, the contours flatten, indicating that an extra 2,000 kg/day expansion results in only marginal ($< \$0.2/\text{kg}$) cost savings. This plateau effect occurs because fixed capital expenditures, while spread over greater throughput, become a progressively smaller portion of total cost as operational expenditures (primarily driven by electricity) dominate.

These results have clear implications for project developers and policymakers. Achieving LCOH targets in the \$4–6/kg range requires either electricity costs below \$0.05/kWh, capacity factors exceeding 90% on firm power, or a combination of moderate scale (8,000–12,000 kg/day) with sub-\$0.06/kWh energy. Trying to reduce LCOH solely by increasing plant size would require impractically large electrolyzer installations both technically and financially without also having access to low-cost, low-carbon power. In contrast, integrating cost-effective renewable electricity options (e.g., utility-scale wind, solar plus storage) or securing long-term low-price PPAs will lead to much greater reductions in hydrogen unit cost.

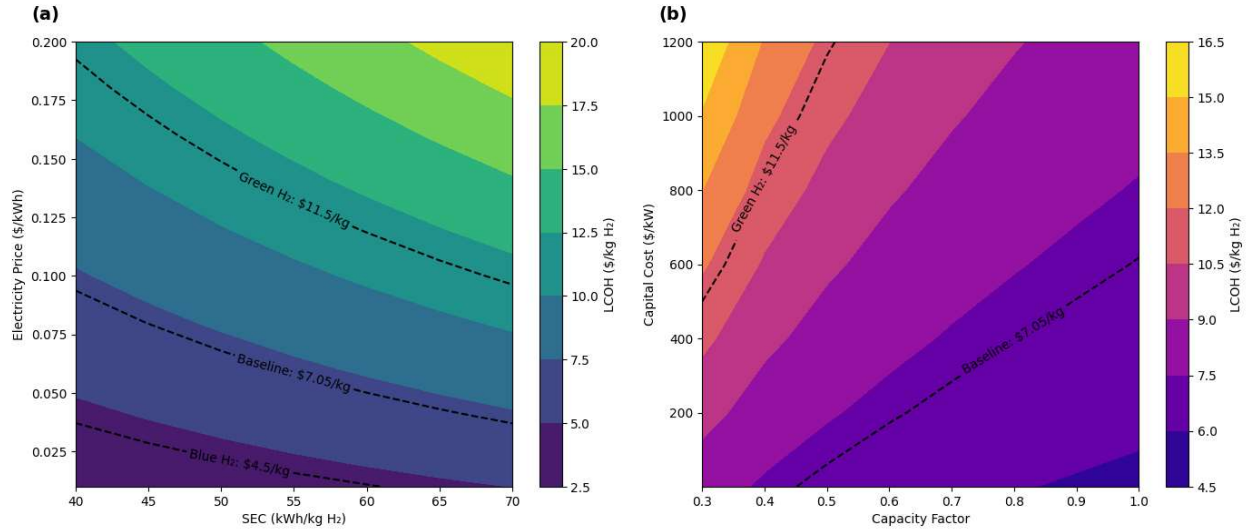


Figure 20: (a) Contour of LCOH (\$/kg H₂), Specific Energy Consumption (kWh/kg H₂) and electricity cost (\$/kWh), (b) Contour of LCOH(\$/kg H₂), Capital Cost (\$/kW) and Plant Capacity Factor

We further extended this analysis to examine the relationship between electrolyzer efficiency, expressed as specific energy consumption (SEC, kWh/kg H₂), and electricity cost (Figure 20a). At very low electricity prices ($< \$0.02/\text{kWh}$), the sensitivity of LCOH to SEC diminishes, reflecting the dominance. Conversely, when power prices exceed $\$0.15/\text{kWh}$, the LCOH contours steepen dramatically, which underscores the critical importance of both high-efficiency stack design and access to low-cost renewables in marginal markets. Although efficiency gains never plateau mathematically, there is a practical limitation (40-50 kWh/kg), while power contracts can sometimes change in larger increments.

At high electricity prices ($\geq \$0.12/\text{kWh}$), a 5 kWh/kg efficiency gain delivers \$1–\$1.5/kg LCOH savings making stack efficiency improvement through R&D more valuable. Whereas at low electricity prices ($\leq \$0.05/\text{kWh}$), that same efficiency gain only saves $\leq \$0.3/\text{kg}$. Our baseline sits below the green-hydrogen threshold. This indicates that even current electrolyzer efficiencies (50 kWh/kg) can produce cost-competitive hydrogen if power can be sourced at $0.075/\text{kWh}$. Further improvements in SEC will deepen that cost advantage. Approaching the blue hydrogen price point will require the SEC to be less than 45 kWh/kg and power $< \$0.03/\text{kWh}$, thus demanding both catalytic breakthroughs and a cheaper electricity source.

The \$11.5/kg “green-hydrogen” threshold (dashed line) shows that at CapEx levels (\$800–\$1 000/kW), the plant must run at a Capacity Factor (CF) greater than 0.7 to be with the baseline price(Figure 20b). Plant downtime can be improved through predictive maintenance for fault detection and reliable RE system configuration. The efficiency of the PEM Electrolyzer is a function of the availability and ratio of energy supplied to the rated power of the electrolyzer system.

4.4 Impact of Renewable Energy configuration on LCOH

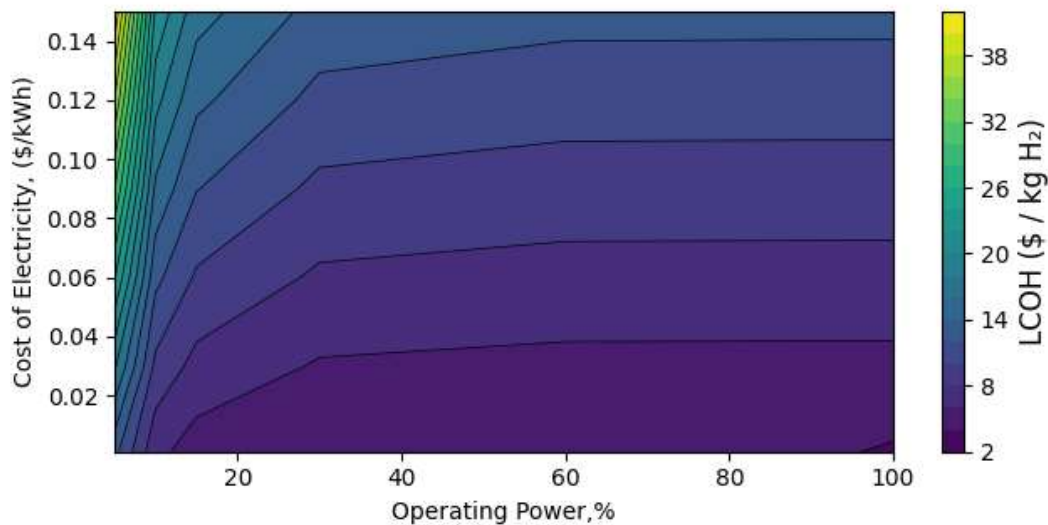


Figure 21: A contour of the LCOH of hydrogen at different operating power and cost of electricity

Figure 21 presents the levelized cost of hydrogen (LCOH) as a function of two operational parameters: the electricity price (from \$0.01 to \$0.15 per kWh) and the electrolyzer operating power expressed as a percentage of its rated power (5 %–100 %). Here, “operating power” is defined as the ratio of actual electrical input to the electrolyzer versus its nameplate power rating. Thus, a proxy for utilization or capacity factor under dynamic dispatch.

At very low operating power ($\leq 10\%$), LCOH rises precipitously, exceeding \$40/kg even at the lowest electricity prices. This behavior reflects the dominance of capital-recovery costs when the same electrolyzer stack is scarcely utilized: with only 876–1,752 hours of full-power equivalent operation per year. Between 20 % and 50 % operating power, LCOH falls sharply as utilization improves from roughly \$18/kg to \$8/kg ($\Delta \$10/\text{kg}$). However, above $\approx 50\%$ load, the contour lines flatten: pushing from 50 % to 100 % only yields another \$3–4/kg reduction. This inflection marks the point where further increases in utilization deliver progressively smaller amortization benefits, and where operating-cost (electricity) begins to dominate.

The results imply that Intermittent renewables alone operating power $\lesssim 30\%$ will risk hydrogen costs $> \$12/\text{kg}$ unless subsidized or unless coupled with storage or demand-management to boost effective load. A Hybrid power integration that ensures $\geq 50\%$ operating power is essential to bring LCOH into the competitive \$6–8/kg band, especially when paired with electricity prices below \$0.08/kWh. Therefore, priority should be given to securing cost-effective, high-availability power through PPAs, co-located renewables with storage, or grid-firm contracts

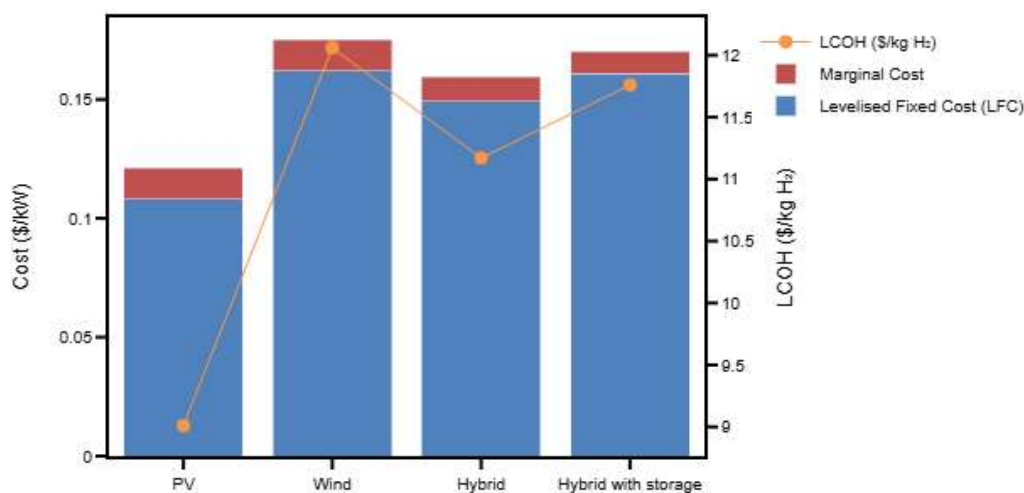


Figure 22: LCOE and the corresponding LCOH impact for hydrogen production for different energy configurations

To conclude our scenario analysis, we examined four different electricity supply options: PV-only, wind-only, a PV–wind hybrid, and a hybrid combined with battery storage. For PEM hydrogen production, the

selection of renewable feedstock is often framed around capacity factor and marginal electricity cost. The basis assumes a uniform 20 MW installed capacity for PV and wind systems (10 + 10 MW for the hybrid), with capacity factors of 25 % (PV), 34 % (wind), and a hybrid setup with storage cycles at one 20 MWh discharge per day.

The PV-only scenario has the lowest energy production cost per kWh (\$0.11/kWh) in fixed charges with negligible marginal costs, resulting in an LCOE of (\$0.12/kWh) and an LCOH of (\$9/kg). Its modest 25% utilization is more than offset by the lower per-kW price of solar panels and minimal balance of plant (BoP) complexity. Wind-only provides more consistent output ($CF \approx 34\%$) but incurs higher levelized fixed charges (\$0.16/kWh) and a larger marginal cost (\$0.03/kWh) due to turbine operations and maintenance (O&M). The turbine capital expenditure (CAPEX) surpasses its better capacity factor, leading to the highest LCOH at \$12.2/kg.

These collectively demonstrate that equipment costs are the main drivers of LCOE in all off-grid scenarios. Greater RE availability does not automatically lead to cheaper hydrogen. Increases in capacity factor from hybridization can offset some of the premium associated with renewable systems, but cannot fully replace access to a low-cost grid or a good PPA tariff. A standalone PV system provides the lowest entry barrier, while hybrid configurations balance moderate cost increases with better reliability. Adding storage further safeguards hydrogen production from renewable intermittency but comes with a capital premium that must be justified by downstream value, such as time-sensitive refueling or grid services revenue. Ultimately, the choice of energy configuration should align with local resource profiles, off-taker needs, and financing constraints. RE system cost savings will translate to lower LCOH if they enable a high utilization rate of the electrolyzer.

Chapter 5: Conclusion

5.1 Summary of Key Findings

This study delivers a definitive framework for forecasting the true cost and value of grid-connected and renewable-driven PEM hydrogen production. We designed and achieved an RMSE of 32 mV against experimental polarization curves. The activation overpotential dominates total voltage loss, suggesting improvement in catalyst layer design. By embedding our validated physics-based electrolyzer model within an economic discounted-cash-flow methodology, we establish benchmarks: a 10,000 kg/day plant at 333 K and 30 bar, fueled at \$0.07/kWh, produces hydrogen at \$7/kg with a 32 % IRR and an \$77 M NPV.

Through systematic scenario-based sensitivity analysis, we showed that the cost of electricity is the dominant lever, capable of affecting LCOH by up to \$2/kg for every \$0.04/kWh change in the tariff. Uninstalled capital cost is the next key driver: achieving DoE's target of \$250/kW stack and BoP can lower hydrogen cost by more than \$1.50/kg. Efficiency improvements (45–55 kWh/kg SEC) and optimized O&M strategies provide incremental gains, under \$0.50/kg in savings, while water and oxygen streams have little economic impact under current market conditions.

Multivariate sensitivity analysis across plant scale and power price shows a clear "sweet spot" for sub-\$5/kg hydrogen: midsize plants (> 8,000 kg/day) paired with electricity tariffs \leq \$0.05/kWh. Financially, plants in this area achieve IRRs above 35% and NPVs in the low hundreds of millions, while smaller or more expensive setups struggle to meet financing requirements. Mid-scale onsite generation (10,000 kg/day) stands out as the most balanced approach: large enough to benefit from scale economies yet sufficiently agile to avoid the market-sizing risks of mega-scale projects.

Among off-grid options, PV-only systems have the lowest capital expenditure (CAPEX) but a moderate levelized cost of hydrogen (LCOH) because of the low capacity factor; wind offers a higher capacity factor

but results in more expensive electricity; PV-wind hybrids provide a compromise. Adding battery storage improves dispatchability but raises LCOH unless electricity-market revenues offset the storage costs. An optimal capacity factor of 40-50 % for renewable energy supply offers a balance of intermittency with plant utilization.

5.2 Intellectual Merit

This study advances the techno-economic analysis of green hydrogen production by introducing a multi-scale modeling framework that integrates detailed electrochemical physics, system-level cost assessment, and dynamic renewable energy integration. Unlike prior work that treats PEM electrolyzer design and energy supply in isolation, our approach unifies these domains through three novel contributions:

1. **Physics-Driven Optimization:** We develop a first-principles, 0D/1D PEM electrolyzer model, parametrized for activation, ohmic and concentration overpotentials, membrane hydration, and gas crossover.
2. **Dynamic, Location-Specific Energy Coupling:** We incorporate hourly-resolved PV, wind, and hybrid generation profiles, sourced from high-resolution irradiance and wind reanalysis data, directly into the electrolyzer simulation.

5.3 Broader Impact

The outcomes of this integrated analysis extend well beyond academic insight. It offers tangible benefits for energy policy, industry strategy, and societal decarbonization goals. First, by providing site-specific LCOH and NPV maps that account for regional renewable resources, this work equips policymakers and planners with the quantitative evidence needed to tailor incentives, such as production tax credits,

renewable energy mandates, or locational subsidies, to locations where green hydrogen can be produced most cost-effectively.

We have demonstrated that distributed, smaller-scale electrolyzers can achieve competitive LCOH in grid-constrained or remote regions, underscores a pathway for industrial decarbonization in hard-to-reach communities and emerging markets. Localized hydrogen production reduces dependence on long-distance gas pipelines, enhances energy resilience, and creates new green job opportunities in manufacturing, operations, and maintenance.

Moreover, the framework's dynamic modeling of intermittency informs grid operators and utilities about the value of flexible loads and hydrogen storage in balancing high penetrations of variable renewable energy sources. By demonstrating how electrolyzers can provide demand response and ancillary services, our work aligns with broader efforts to modernize electric grids, reduce curtailment of solar and wind output, and integrate large-scale clean energy systems.

5.4 Limitations of the Study

Our framework offers a comprehensive technoeconomic perspective of PEM hydrogen; nevertheless, we acknowledge several limitations that may exist. First, we focused only on production, excluding downstream costs like compression, storage, and transportation. In scenarios where hydrogen needs to be transported long distances or stored at high pressures, total supply-chain costs can increase significantly, which could reduce the attractive LCOH and financial returns reported here.

Second, our renewable-integration scenarios employ a simplified dispatch logic that allocates power instantaneously to the electrolyzer and, where applicable, to battery storage. We assumed perfect foresight of hourly resource availability, whereas actual operation will face forecasting errors that lead to suboptimal utilization and slight efficiency penalties.

Third, our financial model uses fixed WACC, tax rate, and offtake price assumptions over the 20-year horizon. Market conditions, policy incentives, and capital market risk premiums may change, resulting in tail risks or upside opportunities that are not captured in the static DCF. Renewable hydrogen models depend on multi-year power purchase agreements, and the termination or renegotiation of these agreements can significantly affect project economics.

Fourth, technical inputs such as stack lifetime, and replacement schedules are informed by current literature and vendor data. However, they may not fully account for emerging degradation modes when managing variable renewable resource operations. We also abstract away detailed water-chemistry dynamics and membrane-electrode-assembly fouling, aspects that can influence maintenance cycles and unplanned downtime.

Finally, our site-specific renewable resource profiles are based on a representative U.S. inland location and may not apply to coastal, arid, or high-latitude regions without recalibration. We maintain consistent policies, tax rates, depreciation schedules, and incentives. However, project sites often encounter changing regulations that significantly impact economics.

5.5 Future Research Directions

Based on the insights from our techno-economic and sensitivity analysis, we've identified several areas for future research.

5.5.1 Multi-Objective Optimization of PEM Electrolyzer Design

An ongoing task is the formulation and solution of a multi-objective optimization problem that seeks to minimize the PEMel design cost (CapEx) and specific energy consumption simultaneously while maximizing cell efficiency under realistic operating constraints. Decision variables would include

membrane thickness, catalyst loading, ionomer content, and operating temperature/current setpoints. The thickness of the MEA influences compactness, heat transfer, mechanical design, and materials usage. The model will provide opportunities to explore trade-offs that are inherently coupled in the design space of the PEM electrolyzer.

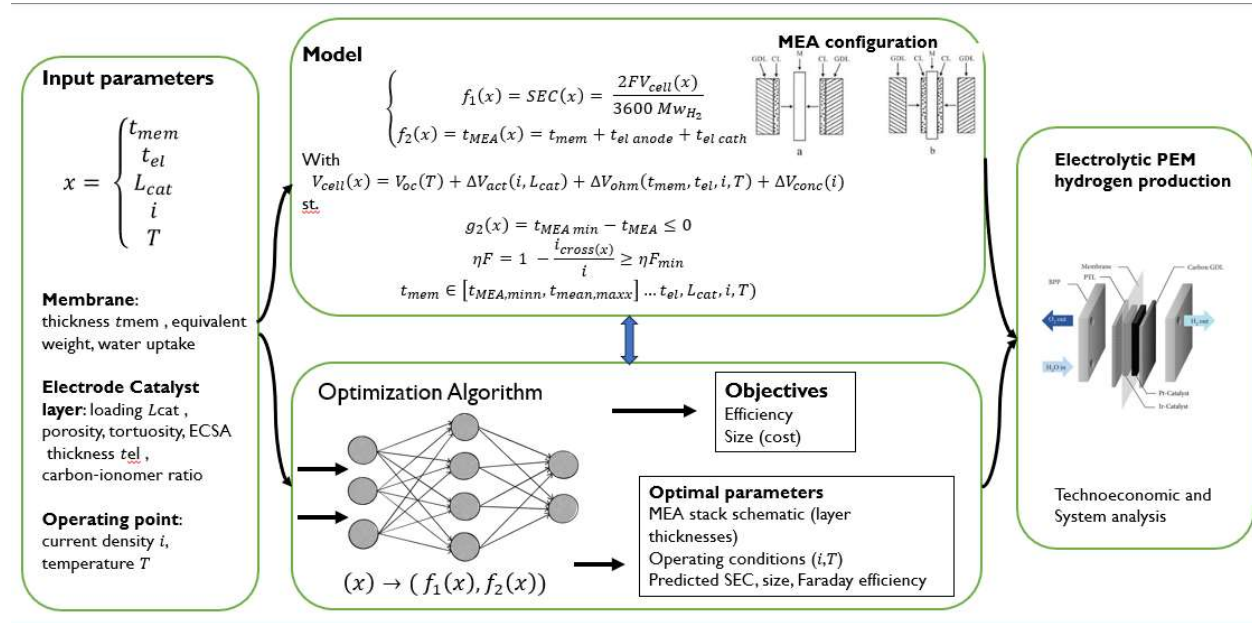


Figure 23 Schematic of the multi-objective optimization workflow, highlighting decision variables, constraints

The proposed optimization workflow (Figure 23) begins by sampling candidate MEA designs, each defined by the decision vector space. For every candidate \mathbf{x} , our coupled model computes the SEC and stack voltage, predicts Faradaic efficiency, and calculates the implied cost factor based on material thicknesses. Through iterative non-dominated sorting and genetic operators, NSGA-II could reveal the envelope of trade-off designs ranging from ultra-thin, high-efficiency stacks with elevated crossover risk to thicker, more robust configurations with slightly higher energy demands[120].

5.5.2 Evaluation of Cost-Reduction Levers

Building on our completed sensitivity analyses (Aim 2), the next phase is to develop the framework to assess the impact of alternative materials and manufacturing pathways that can reduce both the capital and operating costs of PEM electrolyzers. We will focus on three critical components: the membrane, the anode catalyst layer, and the cathode catalyst layer. The proposed workflow will begin with a comprehensive literature survey of advanced membrane chemistries (hydrocarbon-based polymers, reinforced PFSA composites) and low-loading or non-precious-metal catalysts (Ni–Fe, transition-metal carbides) reported in peer-reviewed journals[121], [122]. A catalog of alternative PEM electrolyzer materials and their key parameters and cost parameters will be generated.

A global sensitivity and uncertainty analysis will be conducted using BioSTEAM's built-in Monte Carlo and Sobol sampling routines[123]. By encoding each material option as a discrete "module" within BioSTEAM, we can simulate the full process-level impacts and hundreds of thousands of design variants with different material properties and cost-learning parameters. Parallel Aspen Plus case studies will be developed for cross-validation. Comparisons between our streamlined Python outputs and BioSTEAM's rigorous unit-operation simulations will help to calibrate model fidelity.

5.5.3 Dynamic Optimization of Renewable-Electrolyzer Configurations

The RE potential varies across geographical regions for different energy systems[124]. The next task under ‘Aim 3’ will be to integrate a dynamic, multi-objective optimization layer that selects optimal renewable energy mixes, electrolyzer sizing, and storage capacities to minimize the levelized cost of hydrogen (LCOH) under real-world intermittency. To efficiently explore this high-dimensional design space, we propose using particle swarm optimization (PSO)[125]. PSO particles will represent plausible configurations and pairings whose hourly dispatch is simulated by our renewable and electrolyzer time-series models. At each iteration, we will compute LCOH, capacity factor, and storage utilization metrics for

hundreds of scenarios, then update particle velocities and positions based on local and global optima. The Gaussian process model will accelerate convergence by approximating LCOH responses in unexplored regions, allowing the optimizer to focus on the most promising design clusters. Geospatial variability of renewable resources will be addressed by embedding region-specific weather, tariff, and land-use data into the optimization.

5.5.4 Geospatial, Hourly-Resolved LCOH Mapping with Policy and Emissions Layers

The final element of our dynamic system-analysis(Aim 3) framework will be a comprehensive geospatial assessment that calculates location-specific LCOH by coupling hourly dispatch simulations with regional environmental and financial parameters. This task entails two key components: spatial data integration and incentive modeling.

i. Spatial Data Integration:

We will assemble high-resolution geospatial layers for five archetypal U.S. regions: the Texas Gulf Coast, California Central Valley, Great Plains, New York offshore, and the Phoenix–Casa Grande corridor in Arizona. We will draw on NREL's NSRDB for solar irradiance, the WIND Toolkit for wind speeds, and publicly available elevation, land-use, and grid interconnection maps. Each site will be characterized by its hourly renewable generation potential, prevailing wholesale and time-of-use electricity tariffs, and transmission constraints, ensuring that our dispatch model reflects both physical resource endowment and market exposure.

ii. Policy and Incentive Modeling:

To capture the impact of federal and state incentives on hydrogen economics, we will layer in tax credit eligibility. The Investment Tax Credit (ITC) for renewables and the Production Tax Credit (PTC) for clean hydrogen under the Inflation Reduction Act[3]. We will calculate after-incentive LCOH and NPV for each

location by linking hourly hydrogen production outputs to annualized ITC and PTC cash flows. Additional regional incentives, such as state renewable portfolio standard multipliers or land-use permitting costs, will be included.

Together, these analyses will equip policymakers, developers, and investors with a detailed, site-tailored understanding of green hydrogen viability. It will aid in identifying regions with optimal resource, regulatory, and economic conditions and quantifying how policy levers shift the competitive landscape. This geospatial LCOH atlas will serve as a decision-support tool to accelerate the deployment of cost-effective, clean hydrogen infrastructure at scale.

Appendix A.

PEM Electrolyzer and Energy Design Parameters

This appendix details the parameters, constants, and key assumptions used in the mathematical models for the PEM electrolyzer and the renewable energy systems. Values are drawn from established literature to ensure the model's validity and relevance.

A.1 PEM Electrolyzer Cell Design Parameters and Assumptions

Appendix A. 1 PEM Electrolyzer Cell Design Parameters and Assumptions

Parameter	Value	Reference and basis
Faraday constant, F (C /mol)	96 485	Standard value
Gas constant, R (J/ mol K)	8.314	Standard value
Number of Electrons Transferred (z)	2	Stoichiometry of the water splitting reaction
Cell temperature, T (K)	333.15	Assumption based on the range of practicable temperatures
Cell pressure, P_a/P_c (bar)	1 (anode) / 30 (cathode)	Assumptions for a high-pressure hydrogen onsite generation
Maximum current density, i_{\max} (A /cm ²)	2.0	Assumption based on high-performance MEAs[100]
Limiting current density, i_{\lim} (A /cm ²)	6.0	[94]
Anodic Charge Transfer Coeff. (α_a)	2.0	Typical value for PEM electrolysis OER kinetics[87]

Parameter	Value	Reference and basis
Cathodic Charge Transfer Coeff. (α_c)	0.5	Typical value for PEM electrolysis HER kinetics[15]
Anode Exchange Current Density ($i_{0,a}$, A/cm ²)	2.618×10^{-6}	[87], [126], [127]
Cathode Exchange Current Density ($i_{0,c}$, A/cm ²)	1.0×10^{-1}	[87], [126], [127][79]
Electrode thickness, t_{el} (μm)	200	[128]
Electrode porosity, ε	0.30	[15], [93]
Membrane thickness, t_m (μm)	178	127 - 178 Representative of standard Nafion TM membranes (e.g., N115, N117)
Membrane Conductivity (σ_m)	Empirical function of T and λ	Based on the widely used model for Nafion TM [92]
Electro-osmotic Drag Coeff. (n_d)	Empirical function of T	[96]
Titanium resistivity, ρ_{ti} (Ω cm)	5.0×10^{-3}	[129]
Carbon-paper resistivity, ρ_{CP} (Ω cm)	8.0×10^{-2}	[31]
Water viscosity, (at 60°C) $\mu\text{H}_2\text{O}$ Pa·s	4.67×10^{-4}	Standard value
Water density, $\rho_{\text{H}_2\text{O}}$ kg/m ³	983.2	Standard value
Anode catalyst loading, mg/cm ²	1.54	[31]
Cathode catalyst loading, mg /cm ²	0.40	[31]
Active area, A (cm ²)	877	Assumptions with design range
Cell voltage, V	1.79	Model output

Parameter	Value	Reference and basis
Voltage efficiency	0.69	Model output
Power per cell, kW	3.14	Model output
Total stack power, kW	19 034	Model output
Specific energy consumption of PEM, kWh/kg H ₂	49	Model output

A.1.2 Electrochemical Kinetic Parameters

Appendix A. 2: Reference exchange currents and activation energies for OER and HER[79]

Variable	Value	Reference(s)
$i_{0,cathode}^{ref}$, A/cm ²	0.75×10^{-3} , 1.0×10^{-3} , 9.0×10^{-2} , 1.0×10^{-3}	Pt cathode,[15], [87], [89], [126], [127], [130]
$E_{act,cath}$, J/mol	30,000	[131]
$i_{0,anode}^{ref}$, A/cm ²	1.0×10^{-7} , 1.0×10^{-12} , 1.65×10^{-8} , 1.0×10^{-7}	Pt-Ir anode,[15], [87], [89], [100], [126], [127], [130]
$E_{act,an}$, J/mol	90,000	[40][89]

Appendix A. 3: Polarization Curve Validation data from Debe et al. 2012[99]

Current density, i (A/cm ²)	Cell voltage, V
0.14	1.543
0.24	1.584
0.33	1.607
0.47	1.619

Current density, i (A/cm ²)	Cell voltage, V
0.54	1.663
0.58	1.650
0.80	1.692
0.96	1.723
1.10	1.748
1.24	1.773
1.34	1.791
1.46	1.811
1.59	1.832
1.72	1.853
1.84	1.874

Appendix A. 4: System Energy Balance Parameters based on H2A Case study

	On-site	Centra	Basis and Assumptions
H ₂ Outlet Pressure, bar	30	30	
Cell voltage, volts/cell	1.79	1.79	Based on the electrochemical design output:
Total Stack Energy Usage per mass net H ₂ , kWh _{elec} /kg Net H ₂	49.23	49.23	Based on the electrochemical design output:
BOP Loads			

	On-site	Centra	Basis and Assumptions
Power Inverter Efficiency, %	94%	95%	Based on industry input and H2A parameter. (possible improvement to 97% for advanced systems).
Inverter Electrical Load, kWh _{elec} /kg Net H ₂	2.95	2.59	
Dryer Thermal Load, kWh _{therm} /kg Net H ₂	0.34	0.34	H2A data.[62]
Dryer Efficiency, kWh _{elec} /kWh _{therm}	3.67	3.67	According to industry input from the H2A case study on the ratio of net electrical energy. Forecourt/distributed efficiency will increase by 5%, and Future Central's efficiency will increase by 10%
Dryer Electrical Load, kWh _{elec} /kg Net H ₂	1.25	1.25	[62]
Misc Electrical Load, kWh _{elec} /kg Net H ₂	1.2	1.2	Based on industry input for present state of the art.
Total BOP Electrical Load , kWh _{elec} /kg Net H ₂	5.40	5.04	[62]
Total System Electrical Usage per mass net, H ₂ , kWh _{elec} /kg Net H ₂	54.6	54.3	[62]

A.2 Renewable Energy Design Parameters

This section details the parameters for the renewable energy system components and the overall plant performance specifications.

Appendix A. 5: Photovoltaic (PV) System Model Parameters

Parameter	Value	Basis & Reference
PV rated power, P_{rated} , MW	1.0	Design Basis
Clear-sky STC GHI Irradiance (G_{HI} , G_{STC} , W/m ²)	1 000	Industry standard definition (IEC 61215)[106]
STC Cell Temperature (T_{STC} , °C)	25	Industry standard definition (IEC 61215)[106]
Derating factor, $f_{\text{derPV},y}$	0.90	Accounts for soiling, wiring, inverter losses, etc.,[132]
Annual Degradation Rate, (f_{derate} p_{loss})	0.5% per year	Median degradation rate observed in long-term studies[67], [105]
Cell Power Temperature Coefficient (α_p , %/°C)	0.0035	-0.3% to -0.45% Typical range for monocrystalline silicon panels,[106]
Nominal Operating Cell Temp. (NOCT, °C)	45	Standard parameter for real-world performance estimation,[106]
Ambient temperature (annual mean /amp.), $T_{\text{mean}}/T_{\text{amp}}$, °C	15/10	
Declination, elevation, ° δ/σ	21.75/71.75	
Site Latitude, ϕ ,/° φ °	40	Assumption, 40°N of the equator around Great Plain archetype passes through Kansas, Nebraska, Oklahoma etc.
Panel Tilt Angle, θ_{PV} , °	25	Assumption, a typical solar projectile angle

Appendix A. 6: Wind Turbine Parameters

Parameter	Value	Reference / Justification
Rated power (P_{rated} , MW)	1	Referenced design basis
Air density (ρ , kg/m ³)	1.225	Standard sea-level air density (ISO 2533)
Swept Area per MW, (A , m ² /MW)	3 000	Within the range of practical sizing[109]
Drivetrain & Generator Efficiency (η_{WT})	0.90	Typical efficiency for modern gear-driven turbines 0.90 - 0.95[133]
C_p (power coefficient) C_p	0.40	Values taken from models of specific turbines, e.g., the NREL 5-MW reference turbine or as cited in your text[110]
Weibull scale (λ)(m/s)	8	[111]
Weibull shape (k)	2	[111]
Cut-in Wind Speed (v_{cin} , m/s)	3	Typical operational limit for utility-scale turbines [134] To prevent turbine blades from spinning at low wind speed (curtailment) and to reduce bat fatalities
Rated Wind Speed (v_r , m/s)	13	Speed at which the turbine reaches its nameplate power[133]
Cut-out Wind Speed (v_{cout} , m/s)	25	Safety limit to prevent structural damage at high winds[133]
Tip-speed ratio, ω	10	
Pitch angle β °	2	
Polynomial coefficients c_0 – c_{11}	See Table below	Turbine-specific empirical fit as in Castillo et al. (2023) [110]

Appendix A. 7: Polynomial Power coefficient (cp) curves in wind turbines[110]

Constants	Kotti et al [135]	Khajuria et al [136]	Ovando et al [137]	Llano et al	Shi et al [138]	Bustos et al [139]	Ahmed et al [140]
k_0	5.0×10^{-1}	5.0×10^{-1}	5.2×10^{-1}	5.0×10^{-1}	7.3×10^{-1}	4.4×10^{-1}	1
k_1	1.16×10^2	1.16×10^2	1.16×10^2	7.25×10	1.51×10^2	1.25×10^2	1.10×10^2
k_2	0	4.0×10^{-1}	4.0×10^{-1}	4.0×10^{-1}	5.8×10^{-1}	4.0×10^{-1}	4.0×10^{-1}
k_3	4.0×10^{-1}	0	0	0	0	0	0
k_4	0	0	0	0	2.0×10^{-3}	0	2.0×10^{-3}
k_5	0	0	0	0	2.14	0	2.2
k_6	5	5	5	5	1.32×10	6.94	9.6
k_7	2.1×10	2.1×10	2.1×10	1.3125×10	1.84×10	1.71×10	1.84×10
k_8	0	0	6.8×10^{-3}	0	0	0	0
k_9	8.0×10^{-3}	0	8.0×10^{-2}	8.0×10^{-2}	2.0×10^{-2}	8.0×10^{-2}	2.0×10^{-2}
k_{10}	0	8.8×10^{-2}	0	0	0	0	0
k_{11}	3.5×10^{-2}	3.5×10^{-2}	3.5×10^{-2}	3.5×10^{-2}	3.0×10^{-3}	1.0×10^{-3}	3.0×10^{-2}

Appendix A. 8: Overall Plant Operating and Design Assumptions

Parameter	Value	Basis & Reference
Hydrogen Production Capacity, kg/day	10,000	Design Target
Electrolyzer System Capacity Factor	90%	Based on the H2A model, high availability is assumed
Total System Energy Consumption, kWh/kg H ₂	54.3	Design basis from H2A Centralized PEM model

Parameter	Value	Basis & Reference
Stack-only Energy Consumption, kWh/kg H ₂	49.0	PEM model output
Balance of Plant (BOP) Consumption, kWh/kg H ₂	5.3	Calculated differences include drying, cooling, etc.
Renewable Energy (Wind) Capacity, MW	20	System design assumption
Wind Capacity Factor	34%	Site-specific assumption
PV Only Capacity, MW	20	Scenario assumption (wind-only)
Wind Capacity Factor	25%	Design output
Discount rate, r	0.12	
Lifetime, n, yr	25	
CRF	0.2914	Capital recovery factor

Appendix B:

Economic and System Parameters

Appendix B. 1: Baseline Design Parameters: Technical Operating Parameters and Specifications, and Financial Input Values

Parameters	Input
Production capacity, kg/day	10,000
Start-up Year	2024
Total Uninstalled Capital (\$/kW)	\$995
Total Electrical Usage (kWh/kg)	54.3[% LHV] (61%) (% HHV) (72.6%)
Stack Electrical Usage (kWh/kg)	49[% LHV] (68%) (% HHV) (80%)
BoP Electrical Usage (kWh/kg)	5.04
Stack Current Density (A/cm ²)	2
Cell Voltage (V)	1.8
Specific Electrolyzer Power Consumption at Peak Production (kWh/kg H ₂)	49
Outlet Pressure from Electrolyzer (bar)	30
Installation Cost (% of uninstalled capital cost)	12%
Stack Replacement Interval (years)	10
Stack Replacement Cost Percentage (% of installed capital cost)	15%
Plant Life (years)	20
Stack Degradation Rate (mV/khrs)	1.5
Cell Active Area (cm ²)	877

Parameters	Input
Capacity Factor (%)	90%
Tax rate	27%
Plant Life (years)	20
Depreciation Type	MACRS
Depreciation Schedule Length (years)	3
% of Capital Spent in 1 st , 2 nd , 3 rd year of construction	10%, 60%, 30%
% of Fixed and Variable Operating Cost During Start-up	75%, 50%

*Modified Accelerated Cost Recovery System (MACRS).

Capital Costs and Assumptions

Appendix B. 2: Capital Costs and Assumptions

Item	Value	Basis & Reference
Direct Capital Cost		
Uninstalled Electrolyzer System	\$995/kW	Based on the uninstall cost curve function,[18]
Installation Factor	12% of the uninstalled cost	H2A model default
Indirect Capital Costs		
Site Preparation & Construction	Variable	H2A defaults based on AACE standards
Engineering & Design	Variable	H2A defaults
Project Contingency	15%	H2A model default

Item	Value	Basis & Reference
Total Fixed Capital Investment (FCI)	\$27,455,339	Sum of direct and indirect costs
Working Capital	15% of FCI	H2A model default

AACE International stands for the Association for the Advancement of Cost Engineering

Appendix B. 3: Operating Costs and Assumptions

Item	Value	Basis & Reference
Fixed OPEX		
Maintenance & Repairs	5% of direct capital/year	H2A model default
Labor, G&A, Taxes, Insurance	Variable	Calculated based on H2A defaults for labor rates and tax law
Total Fixed OPEX	\$4,771,667/year	Sum of fixed cost items
Variable OPEX		
Electricity Price (Grid)	\$0.07/kWh	U.S. industrial average (EIA, 2024)
Deionized Water Cost	\$0.007/gallon	H2A model default
Oxygen Byproduct Credit	\$0.03/kg	Assumed credit for sold oxygen
Total Variable OPEX (at 90% CF)	\$18,575,000/year	Sum of variable costs, dominated by electricity

Appendix C:

Sensitivity Analysis Parameters

Appendix C. 1: Uncertainty and Sensitivity Parameters

Parameter	Low	Base	High	Basis / Reference(s)
Installed capital cost, \$/kW	\$800/kW (future DOE target)	\$2,000/kW (current average)	\$3,500/kW (today's high end)	DOE target and cost-reduction projections,
Uninstalled capital cost, \$/kW	\$250/kW by 2026 \$150/kW ultimate (2031)	\$995/kW \$975— \$1,200/kW (for production rates from ~10 MW/yr up to >100 MW/yr)	\$1500/kW	DOE target and cost-reduction projections,[141]
Fixed O&M cost, %	15 % (best-in-class estimates)	17 % (H2A default)	22% (older systems)	H2A assumptions, % of cap. cost/yr
Electricity feedstock cost, \$/kWh	\$0.03/kWh (low-cost renewables)	\$0.07/kWh (U.S. industrial avg.)	\$0.15/kWh (high-retail)	Renewable PPA & EIA data, Hydrogen Program,
Deionized water cost, \$/gal	\$0.002/gal	\$0.005/gal (H2A default)	\$0.010/gal	H2A demineralized-water input,H2A data,
O ₂ by-product credit price, \$/kg	\$0/kg (no sale) base	\$0.09/kg (N. America avg.)	\$0.17/kg (EU spot)	Industrial-gas pricing, H2A database
Corporate tax rate (combined), %	21 % (federal only)	25 % (avg. U.S. combined)	33% (high-state)	Federal & state rates, Tax Foundation
Electrolyzer energy efficiency, kWh/kg H ₂	45 kWh/kg (future target)	55 kWh/kg (current state-of-the-art)	65 kWh/kg (lower-grade)	H2A system performance

References

- [1] S. McQueen *et al.*, “Department of Energy Hydrogen Program Plan,” US Department of Energy (USDOE), Washington, DC (United States), DOE/EE-2128, Nov. 2020. doi: 10.2172/1721803.
- [2] O. Marzouk, “Levelized cost of green hydrogen (LCOH) in the Sultanate of Oman using H₂A-Lite with polymer electrolyte membrane (PEM) electrolyzers powered by solar photovoltaic (PV) electricity,” Dec. 20, 2023, *Rochester, NY*: 4670768. Accessed: Feb. 19, 2024. [Online]. Available: <https://papers.ssrn.com/abstract=4670768>
- [3] L. R. Gomez, E. A. Beagle, M. Lewis, and M. E. Webber, “Determining Life Cycle Emissions of Hydrogen Production Using the 45VH₂-GREET Model for the 45V Hydrogen Production Tax Credit”.
- [4] “45V Hydrogen Tax Credit in the Inflation Reduction Act: Comparing Hourly and Annual Matching,” Resources for the Future. Accessed: Jun. 25, 2024. [Online]. Available: <https://www.rff.org/publications/issue-briefs/45v-hydrogen-tax-credit-in-the-inflation-reduction-act-comparing-hourly-and-annual-matching/>
- [5] J. Nyangon and A. Darekar, “Advancements in hydrogen energy systems: A review of levelized costs, financial incentives and technological innovations,” *Innovation and Green Development*, vol. 3, no. 3, p. 100149, Sep. 2024, doi: 10.1016/j.igd.2024.100149.
- [6] “Green hydrogen cost reduction.” Accessed: Feb. 29, 2024. [Online]. Available: <https://www.irena.org/publications/2020/Dec/Green-hydrogen-cost-reduction>
- [7] S. Oberthür and K. Kulovesi, “Accelerating the EU’s climate transformation: The European Green Deal’s Fit for 55 Package unpacked,” *Review of European, Comparative & International Environmental Law*, vol. 34, no. 1, pp. 7–22, 2025, doi: 10.1111/reel.12596.
- [8] R. Hinrichs-Rahlwes, “Renewable Energy for Climate Protection and Energy Security: Lessons Learned from the European Green Deal and REPowerEU,” 2024. doi: 10.1007/978-3-031-61660-0_17.
- [9] M. de los A. D. Moreno, “Chapter 6: Green hydrogen mitigates the EU’s energy dependence and leads to climate neutrality in 2050,” 2023. Accessed: Jul. 13, 2025. [Online]. Available: <https://www.elgaronline.com/edcollchap/book/9781035317844/book-part-9781035317844-17.xml>
- [10] B. S. Pivovar, M. F. Ruth, D. J. Myers, and H. N. Dinh, “Hydrogen: Targeting \$1/kg in 1 Decade,” *Electrochem. Soc. Interface*, vol. 30, no. 4, p. 61, Dec. 2021, doi: 10.1149/2.F15214IF.
- [11] DoE, “Hydrogen Shot,” Energy.gov. Accessed: Jul. 13, 2024. [Online]. Available: <https://www.energy.gov/eere/fuelcells/hydrogen-shot>
- [12] “Guidelines to Determine Well-to-Gate Greenhouse Gas (GHG) Emissions of Hydrogen Production Pathways using 45VH₂-GREET Rev. August 2024,” 2024.
- [13] “Section 45V Clean Hydrogen Production Tax Credits”.
- [14] “45V Hydrogen Tax Credit in the Inflation Reduction Act: Evaluating Emissions and Costs,” Resources for the Future. Accessed: Jun. 25, 2024. [Online]. Available: <https://www.resources.org/common-resources/45v-hydrogen-tax-credit-in-the-inflation-reduction-act-evaluating-emissions-and-costs/>
- [15] M. Carmo, D. L. Fritz, J. Mergel, and D. Stolten, “A comprehensive review on PEM water electrolysis,” *International Journal of Hydrogen Energy*, vol. 38, no. 12, pp. 4901–4934, Apr. 2013, doi: 10.1016/j.ijhydene.2013.01.151.
- [16] S. D. Prasetyo, Y. Trisnoaji, Z. Arifin, and A. A. Mahadi, “Harnessing unconventional resources for large-scale green hydrogen production: An economic and technological analysis in Indonesia,” *Unconventional Resources*, vol. 6, p. 100174, Apr. 2025, doi: 10.1016/j.uncres.2025.100174.
- [17] J. M. M. Arcos and D. M. F. Santos, “The Hydrogen Color Spectrum: Techno-Economic Analysis of the Available Technologies for Hydrogen Production,” *Gases*, vol. 3, no. 1, Art. no. 1, Feb. 2023, doi: 10.3390/gases3010002.

- [18] E. Curcio, “Techno-economic analysis of hydrogen production: Costs, policies, and scalability in the transition to net-zero,” *International Journal of Hydrogen Energy*, vol. 128, pp. 473–487, May 2025, doi: 10.1016/j.ijhydene.2025.04.013.
- [19] J. Huang, P. Balcombe, and Z. Feng, “Technical and economic analysis of different colours of producing hydrogen in China,” *Fuel*, vol. 337, p. 127227, Apr. 2023, doi: 10.1016/j.fuel.2022.127227.
- [20] F. Pruvost, S. Cloete, C. Arnaiz del Pozo, and A. Zaabout, “Blue, green, and turquoise pathways for minimizing hydrogen production costs from steam methane reforming with CO₂ capture,” *Energy Conversion and Management*, vol. 274, p. 116458, Dec. 2022, doi: 10.1016/j.enconman.2022.116458.
- [21] J. Incer-Valverde, A. Korayem, G. Tsatsaronis, and T. Morosuk, “‘Colors’ of hydrogen: Definitions and carbon intensity,” *Energy Conversion and Management*, vol. 291, p. 117294, Sep. 2023, doi: 10.1016/j.enconman.2023.117294.
- [22] V. Venizelou and A. Poullikkas, “Comprehensive Overview of Recent Research and Industrial Advancements in Nuclear Hydrogen Production,” *Energies*, vol. 17, no. 12, Art. no. 12, Jun. 2024, doi: 10.3390/en17122836.
- [23] A. Swartbooi, K. K. Kapanji-Kakoma, and N. M. Musyoka, “From Biogas to Hydrogen: A Techno-Economic Study on the Production of Turquoise Hydrogen and Solid Carbons,” *Sustainability*, vol. 14, no. 17, Art. no. 17, Sep. 2022, doi: 10.3390/su141711050.
- [24] V. J. Aimikhe and O. E. Eyankware, “Recent Advances in White Hydrogen Exploration and Production: A Mini Review,” *JENRR*, vol. 13, no. 4, pp. 64–79, Apr. 2023, doi: 10.9734/jenrr/2023/v13i4272.
- [25] C. Beurey *et al.*, “Review and Survey of Methods for Analysis of Impurities in Hydrogen for Fuel Cell Vehicles According to ISO 14687:2019,” *Front. Energy Res.*, vol. 8, Feb. 2021, doi: 10.3389/fenrg.2020.615149.
- [26] M. Post, W. Buttner, D. Pearman, K. Hartmann, and I. Palin, “Hydrogen Contaminant Detector”.
- [27] M. J. F. Hookham *et al.*, “Impact of Hydrogen Liquefaction on Hydrogen Fuel Quality for Transport Applications (ISO-14687:2019),” *Processes*, vol. 10, no. 9, Art. no. 9, Sep. 2022, doi: 10.3390/pr10091697.
- [28] N. Sezer, S. Bayhan, U. Fesli, and A. Sanfilippo, “A comprehensive review of the state-of-the-art of proton exchange membrane water electrolysis,” *Materials Science for Energy Technologies*, vol. 8, pp. 44–65, Jan. 2025, doi: 10.1016/j.mset.2024.07.006.
- [29] M. F. Ahmad Kamaroddin *et al.*, “Membrane-Based Electrolysis for Hydrogen Production: A Review,” *Membranes*, vol. 11, no. 11, Art. no. 11, Nov. 2021, doi: 10.3390/membranes11110810.
- [30] J. Zhao, H. Liu, and X. Li, “Structure, Property, and Performance of Catalyst Layers in Proton Exchange Membrane Fuel Cells,” *Electrochem. Energy Rev.*, vol. 6, no. 1, p. 13, Mar. 2023, doi: 10.1007/s41918-022-00175-1.
- [31] K. Zhang *et al.*, “Status and perspectives of key materials for PEM electrolyzer,” *Nano Research Energy*, vol. 1, p. e9120032, Dec. 2022, doi: 10.26599/NRE.2022.9120032.
- [32] P. Millet, N. Mbemba, S. A. Grigoriev, V. N. Fateev, A. Aukauloo, and C. Etiévant, “Electrochemical performances of PEM water electrolysis cells and perspectives,” *International Journal of Hydrogen Energy*, vol. 36, no. 6, pp. 4134–4142, Mar. 2011, doi: 10.1016/j.ijhydene.2010.06.105.
- [33] R. Vinodh, T. Palanivel, S. Sharanappa Kalanur, and B. G. Pollet, “Recent advancements in catalyst coated membranes for water electrolysis: a critical review,” *Energy Advances*, vol. 3, no. 6, pp. 1144–1166, 2024, doi: 10.1039/D4YA00143E.
- [34] A. H. Abdol Rahim, A. S. Tijani, S. K. Kamarudin, and S. Hanapi, “An overview of polymer electrolyte membrane electrolyzer for hydrogen production: Modeling and mass transport,” *Journal of Power Sources*, vol. 309, pp. 56–65, Mar. 2016, doi: 10.1016/j.jpowsour.2016.01.012.
- [35] H. Nguyen, C. Klose, L. Metzler, S. Vierrath, and M. Breitwieser, “Fully Hydrocarbon Membrane Electrode Assemblies for Proton Exchange Membrane Fuel Cells and Electrolyzers: An Engineering Perspective,” *Advanced Energy Materials*, vol. 12, no. 12, p. 2103559, 2022, doi: 10.1002/aenm.202103559.

- [36] C. Klose *et al.*, “All-Hydrocarbon MEA for PEM Water Electrolysis Combining Low Hydrogen Crossover and High Efficiency,” *Advanced Energy Materials*, vol. 10, no. 14, p. 1903995, 2020, doi: 10.1002/aenm.201903995.
- [37] W. W. Ng, H. S. Thiam, Y. L. Pang, K. C. Chong, and S. O. Lai, “A State-of-Art on the Development of Nafion-Based Membrane for Performance Improvement in Direct Methanol Fuel Cells,” *Membranes*, vol. 12, no. 5, Art. no. 5, May 2022, doi: 10.3390/membranes12050506.
- [38] D. V. Bhalani and B. Lim, “Hydrogen Separation Membranes: A Material Perspective,” *Molecules*, vol. 29, no. 19, Art. no. 19, Jan. 2024, doi: 10.3390/molecules29194676.
- [39] D. W. Shin, M. D. Guiver, and Y. M. Lee, “Hydrocarbon-Based Polymer Electrolyte Membranes: Importance of Morphology on Ion Transport and Membrane Stability,” *Chem. Rev.*, vol. 117, no. 6, pp. 4759–4805, Mar. 2017, doi: 10.1021/acs.chemrev.6b00586.
- [40] M. Suermann, T. J. Schmidt, and F. N. Büchi, “Comparing the kinetic activation energy of the oxygen evolution and reduction reactions,” *Electrochimica Acta*, vol. 281, pp. 466–471, Aug. 2018, doi: 10.1016/j.electacta.2018.05.150.
- [41] M. H. Miles and M. A. Thomason, “Periodic Variations of Overvoltages for Water Electrolysis in Acid Solutions from Cyclic Voltammetric Studies,” *J. Electrochem. Soc.*, vol. 123, no. 10, p. 1459, Oct. 1976, doi: 10.1149/1.2132619.
- [42] S. Zhao *et al.*, “Determining the Electrochemically Active Area of IrO_x Powder Catalysts in an Operating Proton Exchange Membrane Electrolyzer,” *ECS Trans.*, vol. 69, no. 17, p. 877, Sep. 2015, doi: 10.1149/06917.0877ecst.
- [43] M. E. Kreider *et al.*, “Understanding the Effects of Anode Catalyst Conductivity and Loading on Catalyst Layer Utilization and Performance for Anion Exchange Membrane Water Electrolysis,” *ACS Catal.*, vol. 14, no. 14, pp. 10806–10819, Jul. 2024, doi: 10.1021/acscatal.4c02932.
- [44] D. P. K. Mohanta, M. S. Ripa, F. Regnet, and D. L. Jörisen, “Impact of Membrane Types and Catalyst Layers Composition on Performance of Polymer Electrolyte Membrane Fuel Cells,” *ChemistryOpen*, vol. 9, no. 5, p. 607, May 2020, doi: 10.1002/open.202000089.
- [45] M. Darab, A. O. Barnett, G. Lindbergh, M. S. Thomassen, and S. Sunde, “The Influence of Catalyst Layer Thickness on the Performance and Degradation of PEM Fuel Cell Cathodes with Constant Catalyst Loading,” *Electrochimica Acta*, vol. 232, pp. 505–516, Apr. 2017, doi: 10.1016/j.electacta.2017.02.101.
- [46] J. Lee, C. Seol, J. Kim, S. Jang, and S. M. Kim, “Optimizing Catalyst Loading Ratio between the Anode and Cathode for Ultralow Catalyst Usage in Polymer Electrolyte Membrane Fuel Cell,” *Energy Technology*, vol. 9, no. 7, p. 2100113, 2021, doi: 10.1002/ente.202100113.
- [47] K. Ayers, “High efficiency PEM water electrolysis: enabled by advanced catalysts, membranes, and processes,” *Current Opinion in Chemical Engineering*, vol. 33, p. 100719, Sep. 2021, doi: 10.1016/j.coche.2021.100719.
- [48] R. Sharma, M. A. Karlsen, P. Morgen, J. Chamier, D. B. Ravnsbæk, and S. M. Andersen, “Crystalline Disorder, Surface Chemistry, and Their Effects on the Oxygen Evolution Reaction (OER) Activity of Mass-Produced Nanostructured Iridium Oxides,” *ACS Appl. Energy Mater.*, vol. 4, no. 3, pp. 2552–2562, Mar. 2021, doi: 10.1021/acsaem.0c03127.
- [49] P. Lettenmeier *et al.*, “Low-Cost and Durable Bipolar Plates for Proton Exchange Membrane Electrolyzers,” *Sci Rep*, vol. 7, no. 1, p. 44035, Mar. 2017, doi: 10.1038/srep44035.
- [50] A. S. Gago *et al.*, “Protective coatings on stainless steel bipolar plates for proton exchange membrane (PEM) electrolyzers,” *Journal of Power Sources*, vol. 307, pp. 815–825, Mar. 2016, doi: 10.1016/j.jpowsour.2015.12.071.
- [51] M. Maier, K. Smith, J. Dodwell, G. Hinds, P. R. Shearing, and D. J. L. Brett, “Mass transport in PEM water electrolyzers: A review,” *International Journal of Hydrogen Energy*, vol. 47, no. 1, pp. 30–56, Jan. 2022, doi: 10.1016/j.ijhydene.2021.10.013.
- [52] H. Ito *et al.*, “Effect of flow regime of circulating water on a proton exchange membrane electrolyzer,” *International Journal of Hydrogen Energy*, vol. 35, no. 18, pp. 9550–9560, Sep. 2010, doi: 10.1016/j.ijhydene.2010.06.103.

- [53] Y. Wang, Y. Pang, H. Xu, A. Martinez, and K. S. Chen, "PEM Fuel cell and electrolysis cell technologies and hydrogen infrastructure development – a review," *Energy Environ. Sci.*, vol. 15, no. 6, pp. 2288–2328, Jun. 2022, doi: 10.1039/D2EE00790H.
- [54] T. Taner, S. a. H. Naqvi, and M. Ozkaymak, "Techno-economic Analysis of a More Efficient Hydrogen Generation System Prototype: A Case Study of PEM Electrolyzer with Cr-C Coated SS304 Bipolar Plates," *Fuel Cells*, vol. 19, no. 1, pp. 19–26, 2019, doi: 10.1002/fuce.201700225.
- [55] J. O. Majasan, J. I. S. Cho, I. Dedigama, D. Tsaoulidis, P. Shearing, and D. J. L. Brett, "Two-phase flow behaviour and performance of polymer electrolyte membrane electrolyzers: Electrochemical and optical characterisation," *International Journal of Hydrogen Energy*, vol. 43, no. 33, pp. 15659–15672, Aug. 2018, doi: 10.1016/j.ijhydene.2018.07.003.
- [56] H. Li, H. Nakajima, A. Inada, and K. Ito, "Effect of flow-field pattern and flow configuration on the performance of a polymer-electrolyte-membrane water electrolyzer at high temperature," *International Journal of Hydrogen Energy*, vol. 43, no. 18, pp. 8600–8610, May 2018, doi: 10.1016/j.ijhydene.2018.02.171.
- [57] C. Minnaar, F. De Beer, and D. Bessarabov, "Current Density Distribution of Electrolyzer Flow Fields: In Situ Current Mapping and Neutron Radiography," *Energy Fuels*, vol. 34, no. 1, pp. 1014–1023, Jan. 2020, doi: 10.1021/acs.energyfuels.9b03814.
- [58] A. C. Olesen, S. H. Frensch, and S. K. Kær, "Towards uniformly distributed heat, mass and charge: A flow field design study for high pressure and high current density operation of PEM electrolysis cells," *Electrochimica Acta*, vol. 293, pp. 476–495, Jan. 2019, doi: 10.1016/j.electacta.2018.10.008.
- [59] S. S. Lafmejani, A. C. Olesen, and S. K. Kær, "VOF modelling of gas–liquid flow in PEM water electrolysis cell micro-channels," *International Journal of Hydrogen Energy*, vol. 42, no. 26, pp. 16333–16344, Jun. 2017, doi: 10.1016/j.ijhydene.2017.05.079.
- [60] G. Yang *et al.*, "Fully printed and integrated electrolyzer cells with additive manufacturing for high-efficiency water splitting," *Applied Energy*, vol. 215, pp. 202–210, Apr. 2018, doi: 10.1016/j.apenergy.2018.02.001.
- [61] G. Chisholm, P. J. Kitson, N. D. Kirkaldy, L. G. Bloor, and L. Cronin, "3D printed flow plates for the electrolysis of water: an economic and adaptable approach to device manufacture," *Energy & Environmental Science*, vol. 7, no. 9, pp. 3026–3032, 2014, doi: 10.1039/C4EE01426J.
- [62] B. James, W. Colella, J. Moton, G. Saur, and T. Ramsden, "PEM Electrolysis H2A Production Case Study Documentation," NREL/TP--5400-61387, 1214980, Dec. 2013. doi: 10.2172/1214980.
- [63] M. H. A. Khan, "Designing optimal integrated electricity supply configurations for renewable hydrogen generation in Australia," *OPEN ACCESS*.
- [64] M. S. Humbert, G. A. Brooks, A. R. Duffy, C. Hargrave, and M. A. Rhamdhani, "Economics of Electrowinning Iron from Ore for Green Steel Production," *J. Sustain. Metall.*, vol. 10, no. 3, pp. 1679–1701, Sep. 2024, doi: 10.1007/s40831-024-00878-3.
- [65] W. G. Colella, B. D. James, J. M. Moton, G. Saur, and T. Ramsden, "Techno-economic analysis of PEM electrolysis for hydrogen production," presented at the Electrolytic Hydrogen Production Workshop, NREL Golden, CO, 2014.
- [66] W. Su, W. Zheng, Q. Li, Z. Yu, Y. Han, and Z. Bai, "Capacity configuration optimization for green hydrogen generation driven by solar-wind hybrid power based on comprehensive performance criteria," *Front. Energy Res.*, vol. 11, Aug. 2023, doi: 10.3389/fenrg.2023.1256463.
- [67] Y. Astriani, W. Tushar, and M. Nadarajah, "Optimal planning of renewable energy park for green hydrogen production using detailed cost and efficiency curves of PEM electrolyzer," *International Journal of Hydrogen Energy*, vol. 79, pp. 1331–1346, Aug. 2024, doi: 10.1016/j.ijhydene.2024.07.107.
- [68] M. Kim, D. Lee, M. Qi, and J. Kim, "Techno-economic analysis of anion exchange membrane electrolysis process for green hydrogen production under uncertainty," *Energy Conversion and Management*, vol. 302, p. 118134, Feb. 2024, doi: 10.1016/j.enconman.2024.118134.

- [69] F. N. Khatib *et al.*, “Material degradation of components in polymer electrolyte membrane (PEM) electrolytic cell and mitigation mechanisms: A review,” *Renewable and Sustainable Energy Reviews*, vol. 111, pp. 1–14, Sep. 2019, doi: 10.1016/j.rser.2019.05.007.
- [70] J. M. Bracci, E. D. Sherwin, N. L. Boness, and A. R. Brandt, “A cost comparison of various hourly-reliable and net-zero hydrogen production pathways in the United States,” *Nat Commun*, vol. 14, no. 1, p. 7391, Nov. 2023, doi: 10.1038/s41467-023-43137-x.
- [71] A. Badgett, M. Ruth, B. James, and B. Pivovar, “Methods identifying cost reduction potential for water electrolysis systems,” *Current Opinion in Chemical Engineering*, vol. 33, p. 100714, Sep. 2021, doi: 10.1016/j.coche.2021.100714.
- [72] A. Badgett, S. Teplin, and B. Gilman, “Key Performance Indicators (KPIs) and Technoeconomic Analysis (TEA) of a Novel Polymer Electrolyzer Using Seawater Feedstock (Final Report),” National Renewable Energy Laboratory (NREL), Golden, CO (United States); Evolve Hydrogen, Inc., Stony Brook, NY (United States), NREL/TP-6A20-87737; CRD-22-23259, Oct. 2023. doi: 10.2172/2202790.
- [73] A. Badgett *et al.*, “An economic analysis of the role of materials, system engineering, and performance in electrochemical carbon dioxide conversion to formate,” *Journal of Cleaner Production*, vol. 351, p. 131564, Jun. 2022, doi: 10.1016/j.jclepro.2022.131564.
- [74] B. D. James, D. A. DeSantis, and G. Saur, “Final Report: Hydrogen Production Pathways Cost Analysis (2013 – 2016),” Strategic Analysis Inc., Arlington, VA (United States), DOE-StrategicAnalysis-6231-1, Sep. 2016. doi: 10.2172/1346418.
- [75] J. J. Caparrós Mancera, F. Segura Manzano, J. M. Andújar, F. J. Vivas, and A. J. Calderón, “An Optimized Balance of Plant for a Medium-Size PEM Electrolyzer: Design, Control and Physical Implementation,” *Electronics*, vol. 9, no. 5, Art. no. 5, May 2020, doi: 10.3390/electronics9050871.
- [76] S. Satyapal, “U.S. DOE Hydrogen Program Annual Merit Review (AMR) Plenary Remarks,” *RENEWABLE ENERGY*, 2023, [Online]. Available: <https://www.energy.gov/eere/fuelcells/hydrogen-shot>
- [77] J. Hemauer, S. Rehfeldt, H. Klein, and A. Peschel, “Performance and cost modelling taking into account the uncertainties and sensitivities of current and next-generation PEM water electrolysis technology,” *International Journal of Hydrogen Energy*, vol. 48, no. 66, pp. 25619–25634, Aug. 2023, doi: 10.1016/j.ijhydene.2023.03.050.
- [78] J. Yates *et al.*, “Techno-economic Analysis of Hydrogen Electrolysis from Off-Grid Stand-Alone Photovoltaics Incorporating Uncertainty Analysis,” *CR-PHYS-SC*, vol. 1, no. 10, Oct. 2020, doi: 10.1016/j.xcrp.2020.100209.
- [79] D. H. Chung, E. J. Graham, B. A. Paren, L. Schofield, Y. Shao-Horn, and D. S. Mallapragada, “Design Space for PEM Electrolysis for Cost-Effective H₂ Production Using Grid Electricity,” *Ind. Eng. Chem. Res.*, vol. 63, no. 16, pp. 7258–7270, Apr. 2024, doi: 10.1021/acs.iecr.4c00123.
- [80] H. Groenemans, G. Saur, C. Mittelsteadt, J. Lattimer, and H. Xu, “Techno-economic analysis of offshore wind PEM water electrolysis for H₂ production,” *Current Opinion in Chemical Engineering*, vol. 37, p. 100828, Sep. 2022, doi: 10.1016/j.coche.2022.100828.
- [81] S. Baral and J. Šebo, “Techno-economic assessment of green hydrogen production integrated with hybrid and organic Rankine cycle (ORC) systems,” *Heliyon*, vol. 10, no. 4, p. e25742, Feb. 2024, doi: 10.1016/j.heliyon.2024.e25742.
- [82] Y. Shibata, “Economic Analysis of Hydrogen Production from Variable Renewables,” 2015.
- [83] G. Saur and C. Ainscough, “U.S. Geographic Analysis of the Cost of Hydrogen from Electrolysis,” NREL/TP-5600-52640, 1033439, Dec. 2011. doi: 10.2172/1033439.
- [84] J. E. T. Bistline *et al.*, “Power sector impacts of the Inflation Reduction Act of 2022,” *Environ. Res. Lett.*, vol. 19, no. 1, p. 014013, Nov. 2023, doi: 10.1088/1748-9326/ad0d3b.
- [85] D. Bessarabov, H. Wang, H. Li, and N. Zhao, *PEM Electrolysis for Hydrogen Production: Principles and Applications*. CRC Press, 2016.

- [86] A. Awasthi, K. Scott, and S. Basu, "Dynamic modeling and simulation of a proton exchange membrane electrolyzer for hydrogen production," *International Journal of Hydrogen Energy*, vol. 36, no. 22, pp. 14779–14786, Nov. 2011, doi: 10.1016/j.ijhydene.2011.03.045.
- [87] F. Marangio, M. Santarelli, M. Pagani, and M. C. Quaglia, "Direct High Pressure Hydrogen Production: a Laboratory Scale PEM Electrolyser Prototype," *ECS Trans.*, vol. 17, no. 1, p. 555, May 2009, doi: 10.1149/1.3142786.
- [88] M. Espinosa-López *et al.*, "Modelling and experimental validation of a 46 kW PEM high pressure water electrolyzer," *Renewable Energy*, vol. 119, pp. 160–173, Apr. 2018, doi: 10.1016/j.renene.2017.11.081.
- [89] R. García-Valverde, N. Espinosa, and A. Urbina, "Simple PEM water electrolyser model and experimental validation," *International Journal of Hydrogen Energy*, vol. 37, no. 2, pp. 1927–1938, Jan. 2012, doi: 10.1016/j.ijhydene.2011.09.027.
- [90] E. Crespi, G. Guandalini, L. Mastropasqua, S. Campanari, and J. Brouwer, "Experimental and theoretical evaluation of a 60 kW PEM electrolysis system for flexible dynamic operation," *Energy Conversion and Management*, vol. 277, p. 116622, Feb. 2023, doi: 10.1016/j.enconman.2022.116622.
- [91] P. H. Lee, S. S. Han, and S. S. Hwang, "Three-Dimensional Transport Modeling for Proton Exchange Membrane(PEM) Fuel Cell with Micro Parallel Flow Field," *Sensors*, vol. 8, no. 3, Art. no. 3, Mar. 2008, doi: 10.3390/s8031475.
- [92] T. E. Springer, T. A. Zawodzinski, and S. Gottesfeld, "Polymer Electrolyte Fuel Cell Model," *J. Electrochem. Soc.*, vol. 138, no. 8, p. 2334, Aug. 1991, doi: 10.1149/1.2085971.
- [93] B. Han, S. M. Steen, J. Mo, and F.-Y. Zhang, "Electrochemical performance modeling of a proton exchange membrane electrolyzer cell for hydrogen energy," *International Journal of Hydrogen Energy*, vol. 40, no. 22, pp. 7006–7016, Jun. 2015, doi: 10.1016/j.ijhydene.2015.03.164.
- [94] D. Bessarabov and P. Millet, *PEM Water Electrolysis*. Academic Press, 2018.
- [95] Z. Kang, M. Pak, and G. Bender, "Introducing a novel technique for measuring hydrogen crossover in membrane-based electrochemical cells," *International Journal of Hydrogen Energy*, vol. 46, no. 29, pp. 15161–15167, Apr. 2021, doi: 10.1016/j.ijhydene.2021.02.054.
- [96] K. Onda, T. Murakami, T. Hikosaka, M. Kobayashi, R. Notu, and K. Ito, "Performance Analysis of Polymer-Electrolyte Water Electrolysis Cell at a Small-Unit Test Cell and Performance Prediction of Large Stacked Cell," *J. Electrochem. Soc.*, vol. 149, no. 8, p. A1069, Jun. 2002, doi: 10.1149/1.1492287.
- [97] H. Ito, T. Maeda, A. Nakano, and H. Takenaka, "Properties of Nafion membranes under PEM water electrolysis conditions," *International Journal of Hydrogen Energy*, vol. 36, no. 17, pp. 10527–10540, Aug. 2011, doi: 10.1016/j.ijhydene.2011.05.127.
- [98] P. Molina, C. Rios, C. Martinez de Leon, and J. J. Brey, "Heat management system design and implementation in a PEM water electrolyser," *International Journal of Hydrogen Energy*, Apr. 2024, doi: 10.1016/j.ijhydene.2024.04.089.
- [99] M. K. Debe *et al.*, "Initial Performance and Durability of Ultra-Low Loaded NSTF Electrodes for PEM Electrolyzers," *J. Electrochem. Soc.*, vol. 159, no. 6, pp. K165–K176, 2012, doi: 10.1149/2.065206jes.
- [100] F. Scheepers *et al.*, "Improving the Efficiency of PEM Electrolyzers through Membrane-Specific Pressure Optimization," *Energies*, vol. 13, no. 3, Art. no. 3, Jan. 2020, doi: 10.3390/en13030612.
- [101] D. Jang, J. Kim, D. Kim, W.-B. Han, and S. Kang, "Techno-economic analysis and Monte Carlo simulation of green hydrogen production technology through various water electrolysis technologies," *Energy Conversion and Management*, vol. 258, p. 115499, Apr. 2022, doi: 10.1016/j.enconman.2022.115499.
- [102] S. Khattak, M. Yousif, S. U. Hassan, M. Hassan, and T. A. H. Alghamdi, "Techno-economic and environmental analysis of renewable energy integration in irrigation systems: A comparative study of standalone and grid-connected PV/diesel generator systems in Khyber Pakhtunkhwa," *Heliyon*, vol. 10, no. 10, May 2024, doi: 10.1016/j.heliyon.2024.e31025.

- [103] U. C. Uchenna, "Wind-solar hybrid power system for rural applications in the south eastern states of Nigeria," *J. Electrical Systems*, vol. 8, no. 3, pp. 304–316, 2012.
- [104] Y. El Mghouchi, A. El Bouardi, Z. Choulli, and T. Ajzoul, "Models for obtaining the daily direct, diffuse and global solar radiations," *Renewable and Sustainable Energy Reviews*, vol. 56, pp. 87–99, Apr. 2016, doi: 10.1016/j.rser.2015.11.044.
- [105] A. M. Dubois *et al.*, "Step-by-step evaluation of photovoltaic module performance related to outdoor parameters: evaluation of the uncertainty," in *2017 IEEE 44th Photovoltaic Specialist Conference (PVSC)*, Jun. 2017, pp. 626–631. doi: 10.1109/PVSC.2017.8366615.
- [106] K. Paghasian and G. Tamizhmani, "Photovoltaic module power rating per IEC 61853–1: A study under natural sunlight," in *2011 37th IEEE Photovoltaic Specialists Conference*, Jun. 2011, pp. 002322–002327. doi: 10.1109/PVSC.2011.6186418.
- [107] J. A. Duffie, W. A. Beckman, and N. Blair, *Solar Engineering of Thermal Processes, Photovoltaics and Wind*. John Wiley & Sons, 2020.
- [108] U. B. Gunturu and C. A. Schlosser, "Characterization of wind power resource in the United States," *Atmos. Chem. Phys.*, vol. 12, no. 20, pp. 9687–9702, Oct. 2012, doi: 10.5194/acp-12-9687-2012.
- [109] R. Bhattacharyya and S. K.C., "Assessment of a Wind Energy Conversion System for Sustainable Hydrogen Production by Alkaline Water Electrolysis in India: Effect of Geographical Location and Wind Turbine Type," 2017. [Online]. Available: <https://api.semanticscholar.org/CorpusID:197578291>
- [110] O. C. Castillo, V. R. Andrade, J. J. R. Rivas, and R. O. González, "Comparison of Power Coefficients in Wind Turbines Considering the Tip Speed Ratio and Blade Pitch Angle," *Energies*, vol. 16, no. 6, Art. no. 6, Jan. 2023, doi: 10.3390/en16062774.
- [111] J. Zhang, B.-M. Hodge, and A. Florita, "Joint Probability Distribution and Correlation Analysis of Wind and Solar Power Forecast Errors in the Western Interconnection," *J. Energy Eng.*, vol. 141, no. 1, p. B4014008, Mar. 2015, doi: 10.1061/(ASCE)EY.1943-7897.0000189.
- [112] M. Jafarian, A. Soroudi, and M. Ehsan, "The effects of environmental parameters on wind turbine power PDF curve," in *2008 Canadian Conference on Electrical and Computer Engineering*, May 2008, pp. 001193–001198. doi: 10.1109/CCECE.2008.4564727.
- [113] A. Delgado, C. Gertig, E. Blesa, A. Loza, C. Hidalgo, and R. Ron, "Evaluation of the variability of wind speed at different heights and its impact on the receiver efficiency of central receiver systems," *AIP Conference Proceedings*, vol. 1734, no. 1, p. 030011, May 2016, doi: 10.1063/1.4949063.
- [114] I. Staffell *et al.*, "The role of hydrogen and fuel cells in the global energy system," *Energy Environ. Sci.*, vol. 12, no. 2, pp. 463–491, Feb. 2019, doi: 10.1039/C8EE01157E.
- [115] M. Penev, "Techno-Economic Modelling with H2A and H2FAST".
- [116] M. Perez, R. Perez, K. R. Rábago, and M. Putnam, "Overbuilding & curtailment: The cost-effective enablers of firm PV generation," *Solar Energy*, vol. 180, pp. 412–422, Mar. 2019, doi: 10.1016/j.solener.2018.12.074.
- [117] F. Ueckerdt *et al.*, "On the cost competitiveness of blue and green hydrogen," *Joule*, vol. 8, no. 1, pp. 104–128, Jan. 2024, doi: 10.1016/j.joule.2023.12.004.
- [118] A. T. Mayyas, M. F. Ruth, B. S. Pivovar, G. Bender, and K. B. Wipke, "Manufacturing Cost Analysis for Proton Exchange Membrane Water Electrolyzers," NREL/TP-6A20-72740, 1557965, Aug. 2019. doi: 10.2172/1557965.
- [119] E. Ohn, "The Effect of Corporate Taxation on Investment and Financial Policy: Evidence from the DPAD," *American Economic Journal: Economic Policy*, vol. 10, no. 2, pp. 272–301, May 2018, doi: 10.1257/pol.20150378.
- [120] A. Nowé, "Genetic Algorithms," in *Encyclopedia of Astrobiology*, M. Gargaud, R. Amils, J. C. Quintanilla, H. J. (Jim) Cleaves, W. M. Irvine, D. L. Pinti, and M. Viso, Eds., Berlin, Heidelberg: Springer, 2011, pp. 635–639. doi: 10.1007/978-3-642-11274-4_629.
- [121] "Critical and strategic raw materials for electrolyzers, fuel cells, metal hydrides and hydrogen separation technologies," *International Journal of Hydrogen Energy*, vol. 71, pp. 433–464, Jun. 2024, doi: 10.1016/j.ijhydene.2024.05.096.

- [122] S. Massari and M. Ruberti, "Rare earth elements as critical raw materials: Focus on international markets and future strategies," *Resources Policy*, vol. 38, no. 1, pp. 36–43, Mar. 2013, doi: 10.1016/j.resourpol.2012.07.001.
- [123] Y. Cortes-Peña, D. Kumar, V. Singh, and J. S. Guest, "BioSTEAM: A Fast and Flexible Platform for the Design, Simulation, and Techno-Economic Analysis of Biorefineries under Uncertainty," *ACS Sustainable Chem. Eng.*, vol. 8, no. 8, pp. 3302–3310, Mar. 2020, doi: 10.1021/acssuschemeng.9b07040.
- [124] G. Maclaurin *et al.*, "The Renewable Energy Potential (reV) Model: A Geospatial Platform for Technical Potential and Supply Curve Modeling," NREL/TP--6A20-73067, 1563140, MainId:13369, Jun. 2021. doi: 10.2172/1563140.
- [125] S. Mohammadi, V.-H. Bui, W. Su, and B. Wang, "Surrogate Modeling for Solving OPF: A Review," *Sustainability*, vol. 16, no. 22, Art. no. 22, Jan. 2024, doi: 10.3390/su16229851.
- [126] P. Choi, D. G. Bessarabov, and R. Datta, "A simple model for solid polymer electrolyte (SPE) water electrolysis," *Solid State Ionics*, vol. 175, no. 1, pp. 535–539, Nov. 2004, doi: 10.1016/j.ssi.2004.01.076.
- [127] K. W. Harrison, E. Hernández-Pacheco, M. Mann, and H. Salehfar, "Semiempirical Model for Determining PEM Electrolyzer Stack Characteristics," *Journal of Fuel Cell Science and Technology*, vol. 3, no. 2, pp. 220–223, Nov. 2005, doi: 10.1115/1.2174072.
- [128] N. Baumann, C. Cremers, K. Pinkwart, and J. Tübke, "Membrane Electrode Assemblies for Water Electrolysis using WO₃-Supported IrxRu_{1-x}O₂ Catalysts," *Energy Technology*, vol. 4, no. 1, pp. 212–220, 2016, doi: 10.1002/ente.201500258.
- [129] J. Mo, S. M. Steen, S. Retterer, D. A. Cullen, A. Terekhov, and F.-Y. Zhang, "Mask-Patterned Wet Etching of Thin Titanium Liquid/Gas Diffusion Layers for a PEMEC," *ECS Trans.*, vol. 66, no. 24, p. 3, Aug. 2015, doi: 10.1149/06624.0003ecst.
- [130] C. Coutanceau, S. Baranton, and T. Audichon, "Chapter 3 - Hydrogen Production From Water Electrolysis," in *Hydrogen Electrochemical Production*, C. Coutanceau, S. Baranton, and T. Audichon, Eds., in *Hydrogen Energy and Fuel Cells Primers.*, Academic Press, 2018, pp. 17–62. doi: 10.1016/B978-0-12-811250-2.00003-0.
- [131] Z.-D. He, J. Wei, Y.-X. Chen, E. Santos, and W. Schmickler, "Hydrogen evolution at Pt(111) – activation energy, frequency factor and hydrogen repulsion," *Electrochimica Acta*, vol. 255, pp. 391–395, Nov. 2017, doi: 10.1016/j.electacta.2017.09.127.
- [132] E. Amores, J. Rodríguez, J. Oviedo, and A. Lucas-Consuegra, "Development of an operation strategy for hydrogen production using solar PV energy based on fluid dynamic aspects," *Open Engineering*, vol. 7, Jun. 2017, doi: 10.1515/eng-2017-0020.
- [133] M. Zweiffel *et al.*, "Influence of drivetrain efficiency determination on the torque control of wind turbines," *Forsch Ingenieurwes*, vol. 87, no. 1, pp. 129–138, Mar. 2023, doi: 10.1007/s10010-023-00630-5.
- [134] M. D. Whitby, M. T. O'Mara, C. D. Hein, M. Huso, and W. F. Frick, "A decade of curtailment studies demonstrates a consistent and effective strategy to reduce bat fatalities at wind turbines in North America," *Ecological Solutions and Evidence*, vol. 5, no. 3, p. e12371, Jul. 2024, doi: 10.1002/2688-8319.12371.
- [135] R. Kotti, S. Janakiraman, and W. Shireen, "Adaptive sensorless Maximum Power Point Tracking control for PMSG Wind Energy Conversion Systems," in *2014 IEEE 15th Workshop on Control and Modeling for Power Electronics (COMPEL)*, Jun. 2014, pp. 1–8. doi: 10.1109/COMPEL.2014.6877181.
- [136] S. Khajuria and J. Kaur, "Implementation of pitch control of wind turbine using Simulink (Matlab)," *International Journal of Advanced Research in Computer Engineering & Technology*, vol. 1, no. 4, pp. 196–200, 2012.
- [137] R. II. Ovando, J. Aguayo, and M. Cotorogea, "Emulation of a Low Power Wind Turbine with a DC motor in Matlab/Simulink," in *2007 IEEE Power Electronics Specialists Conference*, Jun. 2007, pp. 859–864. doi: 10.1109/PESC.2007.4342101.

- [138] Q. Shi, G. Wang, L. Fu, L. Yuan, and H. Huang, "State-space averaging model of wind turbine with PMSG and its virtual inertia control," in *IECON 2013 - 39th Annual Conference of the IEEE Industrial Electronics Society*, Nov. 2013, pp. 1880–1886. doi: 10.1109/IECON.2013.6699418.
- [139] G. Bustos, L. S. Vargas, F. Milla, D. Sáez, H. Zareipour, and A. Nuñez, "Comparison of fixed speed wind turbines models: A case study," in *IECON 2012 - 38th Annual Conference on IEEE Industrial Electronics Society*, Oct. 2012, pp. 961–966. doi: 10.1109/IECON.2012.6388937.
- [140] D. Ahmed, F. Karim, and A. Ahmad, "Design and modeling of low-speed axial flux permanent magnet generator for wind based micro-generation systems," in *2014 International Conference on Robotics and Emerging Allied Technologies in Engineering (iCREATE)*, Apr. 2014, pp. 51–57. doi: 10.1109/iCREATE.2014.6828338.
- [141] A. Badgett *et al.*, "Updated Manufactured Cost Analysis for Proton Exchange Membrane Water Electrolyzers," NREL/TP--6A20-87625, 2311140, MainId:88400, Feb. 2024. doi: 10.2172/2311140.